Low Dimensional Perovskite Light Emitting Diodes based on Self-assembled Monolayer

Delft University of Technology

Master Thesis

MS53035

Student

Ziyue Lin - 5915740

Supervisors

Dr. A. J. Böttger (MSE)

Dr. L. Mazzarella (PVMD)

Dr. M. Rana (PVMD)

Phd student Haoxu Wang (PVMD)

Abstract

Perovskite Light-Emitting Diodes (PeLEDs) represent a highly promising LED technology due to their exceptional color purity, tunable emission color, and low manufacturing cost. However, the current record external quantum efficiency (EQE) for PeLEDs is limited to 32%, still below the 40% achieved by organic LEDs (OLEDs). This limitation primarily stems from defects within the perovskite layer and at interfaces between different layers in the device. Effective passivation of these defects is essential for further advancing PeLED efficiency.

In this thesis, we established the first operational PeLEDs within the PVMD group, leveraging its perovskite solar cell production line. We developed the fabrication process from the ground up and characterized the resulting device performance.

The first part of this thesis addresses the stability of perovskite layers during optical testing in ambient air. We observed that carrier lifetime measurements depend heavily on the perovskite's exposure time to air and the presence of protective overlayers, rather than solely on its inherent optoelectronic properties. This instability arises from rapid perovskite degradation in air. To mitigate this, we employed spin coating to deposit a protective PMMA layer over the perovskite and optimized this coating process. Characterization confirmed that PMMA significantly slows degradation. Additionally, we identified and corrected alignment issues in the photoluminescence quantum yield (PLQY) measurement setup, which had introduced substantial uncertainty. We refined the PLQY testing procedure to enhance result reliability.

The second part focuses on developing a quasi-2D perovskite emissive layer (EML) with low bulk defect and superior optical properties. Based on quasi-2D perovskites ($PEA_2(FAPbBr_3)_{n1}PbBr_4$) typically exhibit better emission characteristics than bulk counterpart ($FAPbBr_3$) We first confirmed the phase composition of our synthesized perovskite, verifying the formation of quasi-2D perovskite with the targeted phase distribution (n = 3). We then introduced two additives: [2-(9H-Carbazol-9-yl)ethyl]phosphonic Acid (2PACz) and KBr to enhance the optoelectronic property of EML. Photoluminescence (PL) testing revealed that 2PACz significantly enhances PL intensity, while KBr showed no such effect. Subsequently, we applied different antisolvents to improve perovskite film morphology. Results demonstrated that ethyl acetate yielded the highest PLQY. Our champion quasi-2D perovskite sample achieved a PLQY of up to 49%.

The third part details the development and characterization of carrier transport layers for PeLEDs. For the electron transport layer (ETL), we employed 1,3,5-Tris(1-phenyl-1H-benzimidazol-2-yl)benzene (TPBi) and used simulations to study how its thickness affects optical performance. Simulations indicated negligible performance variation for TPBi thicknesses between 40 nm and 80 nm. For the hole transport layer (HTL), we fabricated a self-assembled monolayer (SAM) HTL using [2-(3,6-Dimethoxy-9H-carbazol-9-yl)ethyl]phosphonic Acid (MeO-2PACz) and [4-(3,6-Dimethoxy-9H-carbazol-9-yl)butyl]phosphonic Acid (MeO-4PACz), which could reduce interfacial defect at HTL/ETL interface. However, devices with this SAM-HTL structure didn't emit light during voltage sweeps and exhibiting low turn-on voltages in J-V characteristic. We attribute this to electrical breakdown caused by electron tunneling through the extremely thin (1-2 nm) SAM layer. To suppress tunneling, we introduced an underlying NiO_x layer. This modified structure demonstrated to be successfully prevented tunneling and enabled functional PeLEDs. To further optimize hole transport while minimizing thickness, we modeled the relationship between HTL thickness and electron tunneling probability. Calculations revealed that increasing the HTL thickness by approximately 3 nm effectively shields against tunneling. This optimized, ultra-thin HTL design paves the way for PeLEDs operating at low voltages with state-of-the-art optical performance.

Keywords: perovskite light emitting diodes/PeLEDs; low dimensional perovskite; spin coating; thermal evaporation deposition; A-site doping; hole transport layer; self-assembled monolayer; quantum tunneling; ambient stability

Contents

1 Introduction

The human race has always known that fire and heated objects emit light that can be used for lighting purposes; this knowledge led up to the discovery of artificial lighting. Since the end of the 19th century, artificial lighting has been the subject of a continuous and fascinating evolution; 20th-century scientists and development engineers worldwide created such a wide range of lighting solutions for every lighting application. Today, the importance and application of these "legacy" lighting technologies is decreasing[1].

Since the 21st century, artificial lighting has constituted a significant portion of global energy consumption. In 2017, lighting consumed 2900 TWh of electricity, accounting for 16.5% of worldwide energy usage (Fig.1-1(a)) The International Energy Agency (IEA) predicted in 2013 that, relying solely on conventional policies (e.g., banning incandescent/halogen lamps), global electricity consumption for lighting would surge to 4,250 TWh by 2030, representing approximately 20% of total global electricity demand [2]. According to the prediction made by experts in 2017, from 2020 to 2030, the adoption of Minimum Energy Performance Standards (MEPS) or/and the use of the Best Available Technology (BAT) can lead to more drastic savings (up to an additional 21%). From its side, the US Department of Energy (DoE) estimates that if BAT efficiency follows the expected track, the savings attained by 2035 could amount to 4.8 quads (1 400 TWh) per year in the US only. Conversely, adopting advanced technologies such as light-emitting diodes (LEDs) could significantly reduce energy consumption from lighting (Fig.1-1 (b))

In the different scenarios, all new lighting installations—including indoor, outdoor, emergency, roadway, and automotive applications—now exclusively utilize LED-based equipment [3]. However, as conventional artificial light sources are universally replaced by LEDs, enhancing LED performance across multiple parameters to meet evolving societal demands becomes imperative.

In terms of the commercially available III-V LEDs, they exhibit stable emission and extended operational lifetimes, making them suitable for general illumination. Conversely, organic LEDs (OLEDs), characterized by low driving voltages, wide viewing angles, and high brightness, have gained significant traction in display technologies [4].

Metal halide perovskites (MHPs) represent an emerging class of materials demonstrating exceptional commercialization potential due to their high color purity, tunable bandgap, and high charge carrier mobility [5]. Life cycle analysis (LCA) further reveals substantial cost advantages of perovskite LEDs (PeLEDs) over conventional LEDs. Zhang et al. indicate that PeLEDs exhibit environmental impacts comparable to OLEDs, both being an order of magnitude lower than those of gallium nitride (GaN) LEDs. This disparity primarily stems from the high energy consumption associated with GaN crystal growth, cutting, and polishing. Moreover, transitioning from laboratory-scale to industrial production could reduce PeLED fabrication energy consumption by 50% to 90% [6].

Although OLED manufacturing costs are lower than GaN-based PeLEDs, PeLEDs exhibit superior defect tolerance. This characteristic enables more flexible fabrication approaches and facilitates greater utilization of solution-based processes for PeLEDs. Consequently, PeLEDs retain significant advantages compared to OLEDs [7]. These attributes establish MHPs as promising candidates for next-generation LED emissive layers.

However, current PeLED development remains immature, as evidenced by their low external quantum efficiency (EQE). Although the highest reported EQE for perovskite LEDs has reached 32% [8], this remains substantially lower than the 40% achieved by OLEDs [9]. This limitation primarily stems from high densities of bulk defects and interfacial defects in PeLEDs. In this chapter, I will first introduce MHPs, addressing bulk defects within perovskites and common passivation strategies. Subsequently, I will discuss typical PeLED architectures, highlighting interfacial defects therein. Finally, the objectives of this study will be presented.

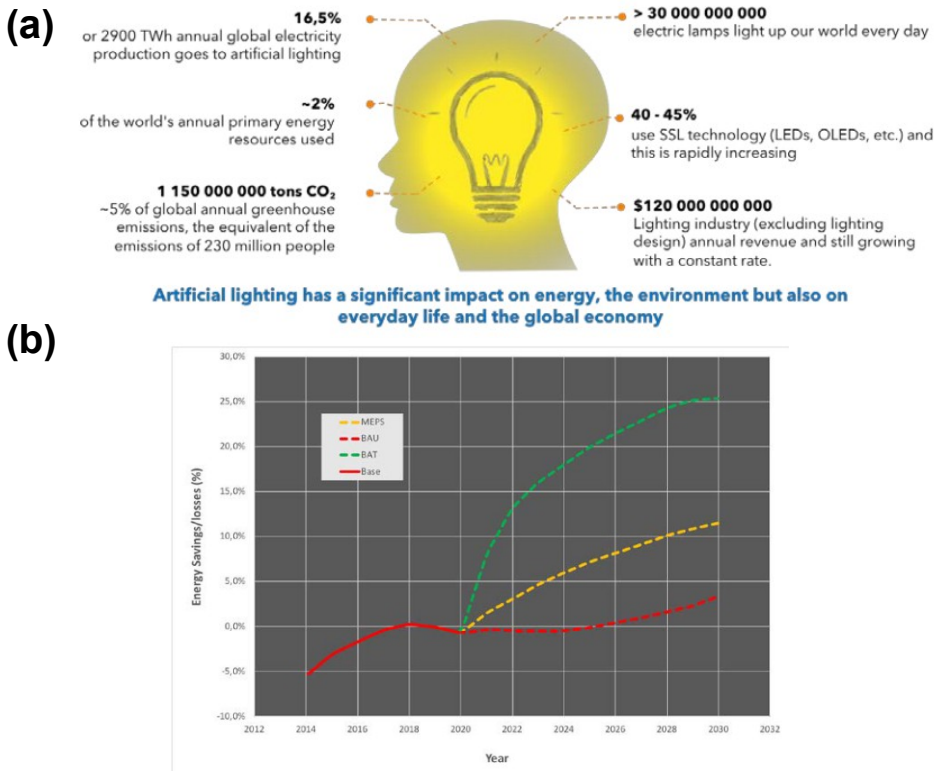

Figure 1-1: (a) A summary of global artificial lighting impact in 2017 (b) Variation of electricity Savings/Losses for lighting from 2013 till 2030 following different scenarios. The "Base" line is calculated extrapolating observed consumption values, the reference year is set to 2017; BAU (Business as usual) scenario admits massive replacement of legacy light sources by LEDs; MEPS scenario suppose the adoption of Minimum Energy Performance Standards worldwide; BAT scenario assumes the use of the Best Available Technology in the market.[1]

1.1 Introduction of Perovskite Materials

Perovskite are a class of materials defined by their unique crystal structure, named by the Russian mineralogist Perovsky, who first discovered this structure in the Ural Mountains. Their three-dimensional network consists of corner-sharing MX_6 octahedra, with "A" cations occupying the cubo-octahedral cavities to ensure electroneutrality (Fig.1-2(a)). The idealized form of perovskite is a cubic structure (space group Pm3m, no. 221). The orthorhombic (e.g. space group Pnma, no. 62, or Amm2, no. 38) and tetragonal (e.g. space group I4/mcm, no. 140, or P4mm, no. 99) structures are the most common non-cubic variants [10].

For MHPs,the A-site is typically occupied by monovalent cations such as Cs^+, formamidinium ($CH_5N_2^+$, FA^+), and methylammonium ($CH_3NH_3^+$, MA^+), the B-site by divalent cations like Pb^{2+}, Sn^{2+}, or Cu^{2+}, and the X-site by halogens (Cl^-, Br^-, I^-) (Fig.1-2(a)). This compositional diversity enables exceptional tunability. When modeling all ions as spheres in a close-packed configuration, the Goldschmidt tolerance factor t concept is derived (Eq. 1-1). Generally, MHPs remain structurally stable within the tolerance factor range of $0.8 \leq t \leq 1$

$$(R_A + R_X) = t\sqrt{2}(R_B + R_X) \tag{1-1}$$

This tunability presents a dual nature. On one hand, it enables bandgap engineering in MHPs, facilitating performance customization. On the other hand, it results in soft lattice characteristics, which increase susceptibility to lattice instability and elevate defect formation energies. Consequently, these factors induce performance degradation in MHP-based optoelectronic devices. This chapter will start from these two characteristics of MHPs and introduce how researchers can utilize tunable bangap while suppressing the occurrence of defects.

1.1.1 Tunable Bandgap in Metal Halide Perovskites

Bandgap modulation strategies are diverse but generally fall into two categories: direct compositional tuning of perovskite constituents to alter the bandgap, or modification of the entire precursor solution system to control crystal dimensions. When crystal dimensions are changed in the nanometer range, the quantum confinement effect becomes significant and changes the bandgap of the crystal.

Compositionally, since the B-site in MHPs is typically occupied by Pb^{2+}, substitution with alternative elements like Sn^{2+} increases oxidation sensitivity, promotes defect formation, and degrades device performance [11]. Consequently, bandgap tuning in MHPs is predominantly achieved through A-site and X-site compositional engineering.

Research has shown that the A-site cation significantly affects the band structure. Borriello et al. demonstrated that cations of varying radii induce distortions in the BX_6 octahedra, altering the band structure slightly[12]. Filip et al. quantified these changes by studying variations in the X-B-X bond angle caused by different A-site cations, which affect the bandgap (Fig. 1-2(b)) [13]. However, practical A-site cations are limited due to constraints imposed by optical properties.

Halogen doping is another method for tuning the bandgap. when the halogen ions at the X-site changes from $I \rightarrow Br \rightarrow Cl$, the covalent nature of the B-X bond increases, resulting in a wider bandgap (Fig.1-2(d))[13]. However, The presence of small halogen ions in MHPs poses significant stability challenges. Small halogen ions exacerbate ion migration, generating abundant vacancies and interstitials defects that facilitate non-radiative recombination. This degradation pathway accounts for the rapid efficiency decay observed under operational bias[14].

Quantum confinement effects is a more versatile and practical tuning approach. Low-dimensional perovskites constitute the most prevalent implementation strategy. By introducing long-chain ligands into A-site, bulk perovskites can be transformed into low-dimensional structures, enabling precise bandgap tuning while simultaneously enhancing optoelectronic properties [9], whose detailed discussion will be presented in Sec.1.1.3.

As illustrated in Fig.1-2(e), the Ruddlesden-Popper (RP) phase represents one of the most extensively studied low-dimensional perovskite structures. This configuration forms when long-chain

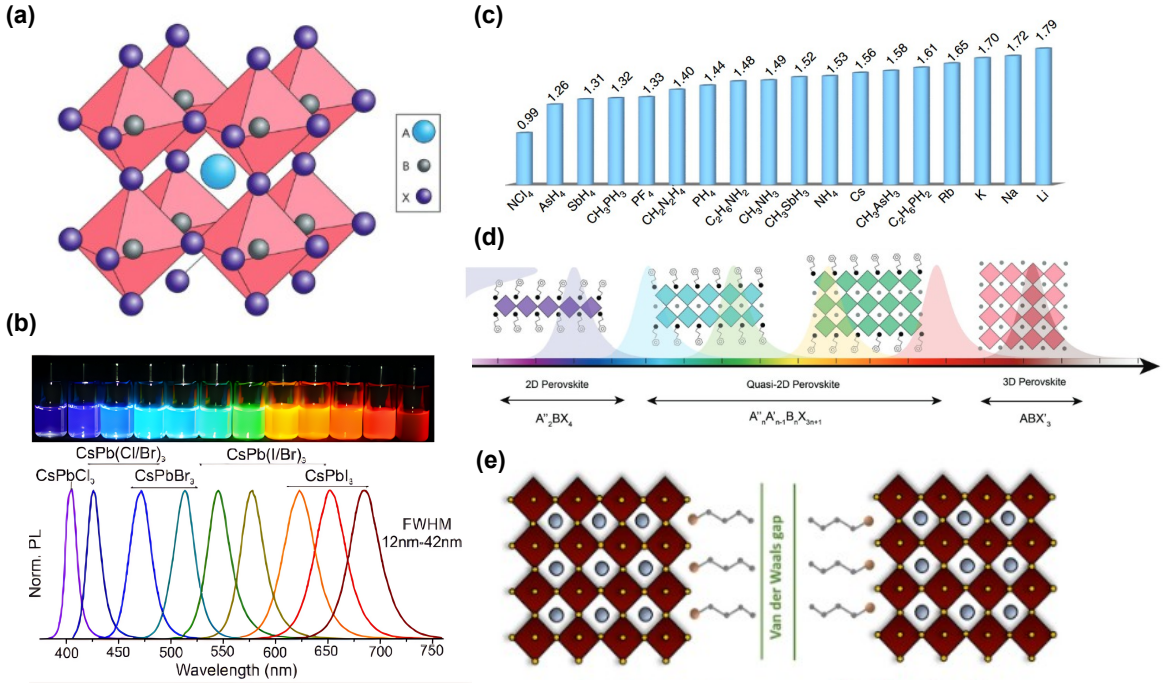

Figure 1-2: (a) Structure of Typical 3D perovskite [5] (b) Relation between bandgap and A-site cation[13] (c)The relation between emission wavelength and perovskite's composition [18] (d) The relation between emission wavelength and perovskite's dimension[5] (e) common structures of low dimensional perovskite [15]

aliphatic or aromatic ammonium cations (R-NH_3^+), such as 2-phenylethylammonium (PEA) or diphenylphosphinamide (DPPA), are incorporated. These cations partition bulk perovskites into layered structures with the general formula $(R\text{-}NH_3)_2A_{n-1}B_nX_{3n+1}$, where n denotes the number of metal halide layers between organic spacers [15]. Increasing n enhances octahedral layer stacking, weakening quantum confinement effects and reducing the bandgap. Consequently, the photoluminescence (PL) peak redshifts as shown in Fig. 1-2(d). Conversely, decreasing n induces a blueshift.

Beyond low-dimensional perovskites, rational ligand engineering enables perovskite crystallization as nanocrystals or quantum dots. Precise size control of these nanostructures provides an alternative route for bandgap engineering [16, 17].

1.1.2 Soft Lattice in Metal Halide Perovskites

Although ABX_3 perovskites can be stable within the conditions defined by Eq. 1-1, the low defect formation energy associated with soft lattices facilitates halogen migration, thereby introducing the bulk defect and reducing the efficiency of PeLEDs [12, 19, 14].

Oranskaia et al. [14] conducted computational studies on defect formation energies in $FAPbBr_3$ and $MAPbBr_3$. They modelled these perovskites and calculated the formation energies of two representative defects—bromide vacancies (V_{Br}) and bromide interstitials (I_{Br})—under Br-poor (Pb-rich), moderate, and Br-rich (Pb-poor) conditions. Their findings revealed that V_{Br} and I_{Br} formation energies in $MAPbBr_3$ were lower than those in $FAPbBr_3$ (Table 1-1). This difference was attributed to two factors: MA^+'s smaller volume, which provides more free space for ion migration, and the favorable dipole-dipole interactions in MA^+ compared to the $\pi - \pi$ interactions in FA^+.

While larger-radius cations like FA^+ can suppress defect formation and enhance efficiency, they also risk lattice distortion, triggering structural transitions from cubic to orthorhombic or tetragonal

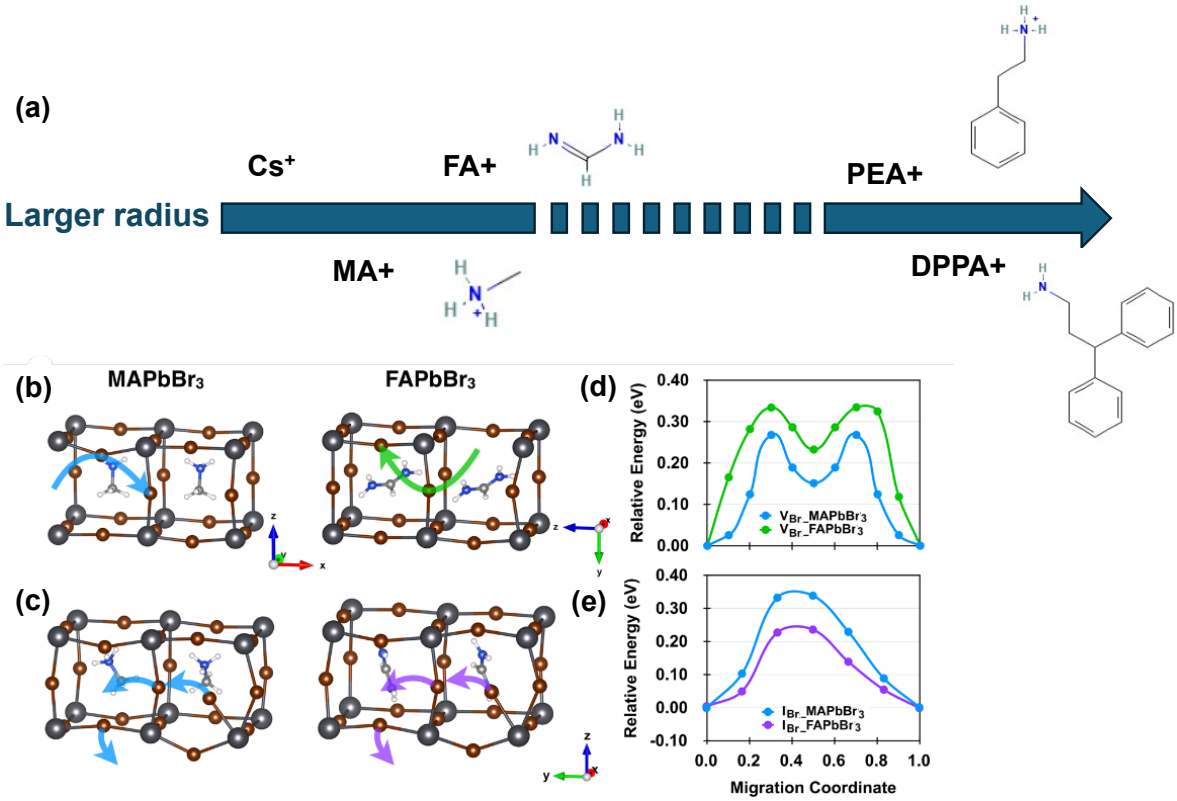

Figure 1-3: (a) Partial A-site dopant ions and radius; (b, c) Bromide vacancy (V_{Br}) and interstitial (I_{Br}) migration pathways; (d, e) Energy profiles along migration paths in $MAPbBr_3$ and $FAPbBr_3$. Relative energy refers to the minimum energy of the optimized crystal structure before ion migration [14].

Table 1-1: Comparison of formation energy (in eV) of V_{Br0} and I_{Br0} for $MAPbBr_3$ and $FAPbBr_3$ under A (Br-Poor, Pb-Rich), B (Moderate), and C (Br-Rich, Pb-Poor) Growth Conditions. Adapted from [14]

Defect	V_{Br0}			I_{Br0}		
	A	B	C	A	B	C
$MAPbBr_3$	1.25	2.01	2.77	1.64	0.88	0.12
$FAPbBr_3$	1.28	2.04	2.80	1.82	1.06	0.30

phases (Fig.1-4(a)) [20]. For example, Han et al. [21] demonstrated that $CsPbI_3$ exists in two phases: the radiative α-phase (cubic phase) and the nonradiative δ-phase (orthorhombic phase). The α-phase remains stable only above 300°C, spontaneously transitioning to the δ-phase at room temperature, reducing efficiency. Adding long-chain cations like 2-(naphthalene-1-yl)ethanamine (NEA) can suppress this transition thereby enhancing PeLED stability. Similarly, adding MA^+ and FA^+ has been proposed to stabilize the lattice and improve performance [21, 22].

The addition of long-chain cation 2-(naphthalene-1-yl)ethanamine (NEA) has been shown to suppress this phase transition and enhance the stability of PeLEDs. Furthermore, the potential of adding MA^+ and FA^+ to stabilize the lattice and improve device performance has also been proposed [21]. However, for pure $FAPbI_3$, it can form the α-$FAPbI_3$ phase at temperatures above 150°C but will still spontaneously degrade into the δ-$FAPbI_3$ phase at room temperature [22].Therefore, for perovskite without A-site doping, the performance challenges mainly come from two aspects: one is the increase in defects concentration caused by soft lattice, and the other is the decrease in thermal stability due to spontaneous phase transformation, thereby decrease radiative recombination efficiency. As all defect influence radiative recombination efficiency, the study on both challenges could be done through some common characterization technology such as PL, PLQY and TRPL etc (detailed in Sec.2.3.3).

To balance defect density and phase stability, alloying $FAPbI_3$ with small amounts of non-native cations such as Cs^+, MA^+, and Rb^+ is a common strategy. Pellet et al. [23] studied the effects of MA^+ and FA^+ ratios on phase transitions and defect density, finding that adding 20% MA^+ to the FA dipping bath avoided the undesirable δ-phase. Photoluminescence measurements revealed that $MA_{0.6}FA_{0.4}PbI_3$ exhibited the longest carrier lifetime, indicating reduced defect density.

Chu et al. [24] demonstrated that doping Cs^+ with $CH_3CH_2NH^{2+}$ (EA) formed $PEA_2(Cs_{1-x}EA_xPbBr_3)_2PbBr_4$. PL measurements showed a blue shift in the peak wavelength and an increase in PLQY from 42% to 70%, although excessive doping (ratio of EABr$\geq$ 80%) reduced efficiency. Zhang et al. [25] compared $CsPbBr_3$ with $Cs_{0.87}MA_{0.13}PbBr_3$, observing significantly higher PL intensity in the MA-doped samples.

These studies underscore the importance of A-site doping in improving PeLED efficiency. A combination of larger- and smaller-radius cations is essential to balance defect suppression and phase stability. While larger-radius cations mitigate the soft lattice issue, they can destabilize the α-phase. Achieving optimal performance requires a well-designed mixture of A-site cations tailored to specific device requirements.

1.1.3 Quasi-2D Perovskite

As shown in Fig. 1-3(a), ligands such as PEA^+ and $DPPA^+$, characterized by the presence of benzene rings, are significantly larger than smaller cations like Cs^+, MA^+, and FA^+. Unlike their smaller counterparts, these larger ligands do not distort the lattice but instead split it, forming low-dimensional perovskites.

This unique structure introduces diverse opportunities for perovskite modification. By altering the dielectric constant of the ligands, researchers can fine-tune the properties of multiple quantum wells, enabling control over exciton binding energies. Similarly, modifying the binding energy between ligands

and inorganic perovskite layers facilitates control over the n-phase distribution, a crucial parameter in perovskite optimization [26].

Ligands are particularly effective in defect passivation. During fabrication, the surface of perovskite thin films often lacks organic components, leading to vacancy defects. Terminal groups such as -NH_2 or -NH_3^+ can occupy these vacancies on the perovskite film surface and passivate related defects (Fig.1-4(b)). Furthermore, in perovskites with varying n-phase distributions formed during the spin-coating process, ligands filling A^+ vacancies can extend the growth of the original crystals and connect perovskites with different phases, creating high-quality heterostructures. For example, Huang et al. demonstrated that BA^+ ligands could grow 2D $(BA)_2PbI_4$ perovskite on top of 3D $MAPbI_3$, combining the high stability of 2D perovskites with the high efficiency of 3D perovskites [27, 28].

Besides, small amount of such ligands can also passivate A-site vacancy without changing n-phase distribution. Zheng et al. [29] introduced 0.1 wt% ligands with varying alkyl chain lengths into their multi-cation alloyed perovskite composition $Cs_{0.05}(FA_{0.92}MA_{0.08})_{0.95}Pb(I_{0.92}Br_{0.08})_3$ and used TRPL to measure the carrier lifetimes of the films, thereby qualitatively inferring the defect density. Notably, this small amount of ligands did not induce significant phase transitions in the perovskite but primarily acted to passivate defects. Results of Zheng et al. [29] showed that ligands with longer alkyl chains, such as oleic acid (OA) and oleylamine (OAm), exhibited significantly longer carrier lifetimes (OA: τ = 789 ns; OAm: τ = 1049 ns) compared to ligands with shorter alkyl chains, such as BA (τ = 195 ns) and PEA (τ = 265 ns). Both sets of ligand-modified films had longer carrier lifetimes than the original film (τ = 114 ns). These findings indicate that the introduction of ligands can effectively suppress non-radiative recombination and improve film quality [29].

In addition to directly binding with vacancies, the unique organic-inorganic alternating structure formed in quasi-2D perovskites by ligands can also inhibit ion migration in the (emissive layer) EML during operation. Huang et al. [30] investigated vertical ion migration by fabricating quasi-2D using allylammonium (ALA) ligands. They employed time-of-flight secondary ion mass spectroscopy (TOF-SIMS) to compare the vertical migration rate of I^- in PSCs made from quasi-2D perovskites versus those made from 3D perovskites without added ligands. The experimental results showed that the migration of I^- from the perovskite layer to the Au electrode in the PSCs made with quasi-2D perovskites was only one-quarter of that in PSCs made with 3D perovskites. Moreover, the quasi-2D perovskite layer exhibited higher PL intensity, demonstrating the excellent properties of long-chain ligands in suppressing perovskite decomposition.

Studies have also shown that 2D perovskite passivation influences surface morphology, including grain size and roughness. This effect is attributed to the changes in the perovskite dimensionality and the introduction of ligands, which impact the recrystallization process described in Sec.2.2.1 [28]. For instance, Zou et al. found that treating $MAPbI_3$ with BAI increased the grain size (Fig.1-4(c)) [31]. Chen et al. [32] utilized long-chain diammonium ligands to form stable ligand–perovskite complexes, improving perovskite nucleation and growth to create high-quality thin films. By substituting heteroatoms in the spacer ligands, they enhanced the ligand–perovskite coordination affinity, enabling precise control over the crystallization behavior. These functionalized spacer ligands strengthened coordination bonding, producing films with reduced residual strain (Fig.1-4(d)). Characterization results revealed that this approach effectively improved defect passivation and suppressed non-radiative recombination in the devices [32].

While ligands improve defect passivation and stability, their insulating nature can hinder charge transport. Balancing their beneficial effects with carrier injection efficiency is crucial, particularly for long-chain ligands [33, 5].

Currently, leveraging long-chain ligands to form quasi-2D perovskites has become a common strategy for enhancing PeLED performance. Feng et al. used PEA^+, Cs^+, and MA^+ as A-site dopants, combined with poly(vinylidene fluoride) (PVDF) post-treatment, to achieve PeLEDs with an EQE of 22.29% [34]. Similarly, Ma et al. introduced fluorinated triphenylphosphine oxide as an additive to a $PEA_2Cs_{1.6}MA_{0.4}Pb_3Br_{10}$ composition, achieving nearly 100% PLQY and an EQE of 25.6% [35].

The stabilizing effects of long-chain ligands also facilitate the use of single A-site molecules in high-quality EMLs. For instance, Guo et al. enhanced $PEA_2(FAPbBr_3)_{n-1}PbBr_4$ with alkali metal

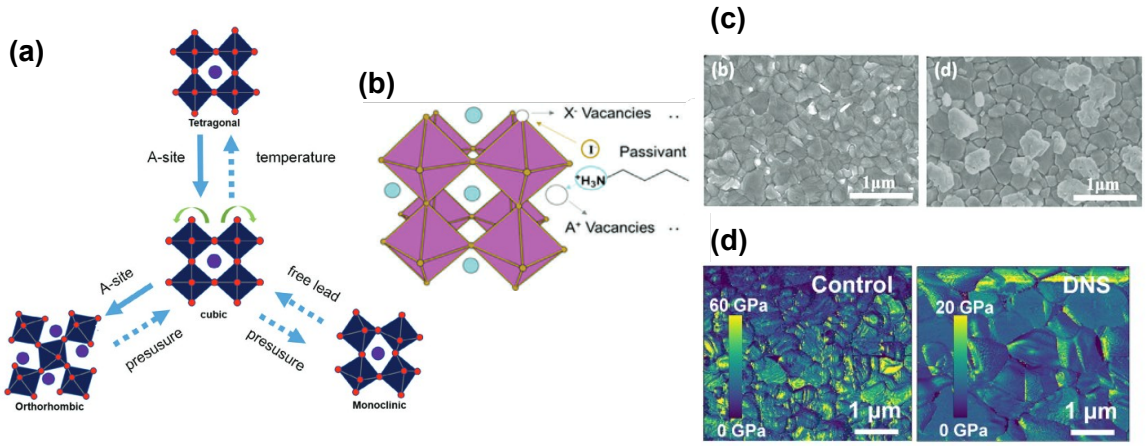

Figure 1-4: (a) Phase transition of perovskite crystal structure due to A-site cations of varying radii. (b) Long-chain ligand passivation of X-site and A-site vacancies in perovskites[27]. (c) SEM images of perovskite films on SnO_2/FTO substrates with and without BAI. Left: without BAI; right: with 1 mg/ml BAI[32].

bromides, achieving a PLQY of 75.4% [36]. Bai et al. doped $FAPbI_3$ with PEABr, obtaining a PLQY of 82.14% and an EQE of 30.84%, the highest reported for green PeLEDs to date [37]. With PEA^+ ligands, both of studies maintain the α structure in perovskite with only FA^+ as small A-site molecule.

These studies demonstrate the transformative role of ligands in PeLEDs, enabling defect passivation, enhanced stability, and high efficiency. However, optimizing ligand design remains crucial for balancing their insulating effects with charge transport to maximize device performance.

1.2 Introduction of Perovskite Light Emitting Diodes

The structure of PeLEDs is inspired by perovskite solar cells and organic LEDs, featuring multiple heterojunction layers, as illustrated in Fig. 1-5. At the heart of these devices is the EML, where the radiative recombination of electron-hole pairs generates light. Adjacent to the EML are the n-type electron transport layer (ETL) and the p-type hole transport layer (HTL), which facilitate the injection of electrons and holes, respectively [38]. These transport layers play a critical role in ensuring device efficiency by balancing charge injection, preventing an excess of one carrier type that can lead to nonradiative recombination. They also act as energy barriers, reducing backflow of carriers, and protecting the EML from environmental degradation by oxygen and moisture [38, 39].

To achieve efficient and balanced charge carrier injection, the energy band structure of PeLEDs must be carefully optimized. For devices with a transparent conducting oxides (TCO)/HTL/EML/ETL/Electrode configuration, the HTL's highest occupied molecular orbital (HOMO) should align between the TCO and EML to minimize the hole injection barrier, while its lowest unoccupied molecular orbital (LUMO) should be slightly higher than the EML's LUMO to block electron injection. Similarly, the ETL's LUMO should align between the electrode and the EML's LUMO, with its HOMO slightly lower than the EML's HOMO [38].

Flexible strategies are often adopted to fine-tune charge transport layers (CTLs). These also include using multi-layer HTLs with different compositions to reduce energetic barriers for hole transport [40], doping CTLs to improve energy alignment [41], and introducing an insulating layer with controlled thickness to adjust carrier injection rates and achieve balance [42].

Beyond energy level alignment, interfacial compatibility between CTLs and perovskites constitutes another critical consideration. Researchers typically pursue CTLs exhibiting smooth surfaces [43], lattice matching with perovskite crystals [44], and favorable wetting properties [45], collectively

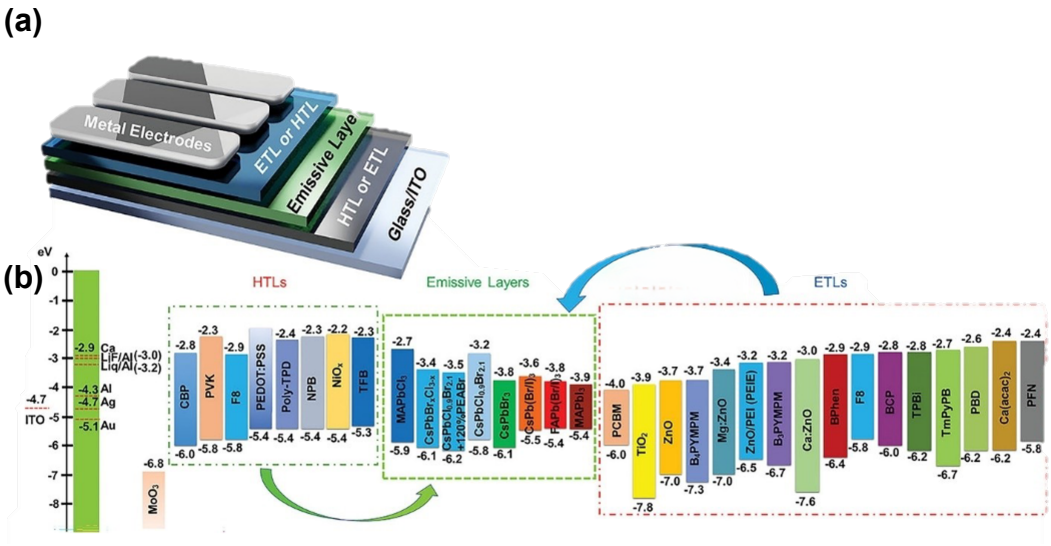

Figure 1-5: (a) Typical structure of PeLEDs (b) Common materials in PeLEDs and their energy structures. The arrows indicate the injection direction of charge carriers, the green arrow indicates the injection of holes, and the blue arrow indicates the injection of electrons[38].

minimizing interfacial defect at perovskite/CTL interfaces.

Consequently, researchers have conducted extensive investigations into HTL/ETL selection, simultaneously evaluating energy level alignment and favorable interfacial properties to optimize device performance.

1.2.1 Common Hole Transport Layer in Perovskite Light Emitting Diodes

In PeLEDs, the HTL generally plays a more critical role than the ETL. This predominance stems from the higher effective mass of holes compared to electrons in conventional semiconductors [46], which renders hole injection more challenging than electron injection. Mainstream PeLED HTLs are categorized into two classes: polymeric semiconductors and metal oxides (MOs).

Polymeric Semiconductor: Common polymer HTLs include PEDOT:PSS, poly[N,N'-bis(4-butylphenyl)-N,N'-bis(phenyl)-benzidine] (polyTPD), poly[9,9-dioctylfluorene-co-N-[4-(3-methylpropyl)]-diphenylamine] (TFB), poly(N-vinylcarbazole) (PVCz), and poly(9-vinylcarbazole) (PVK). However, during spin coating, polymer HTLs can dissolve into the perovskite precursor solution, leading to direct contact between the perovskite EML and the ITO anode. This contact can quench excitons in the perovskite and reduce EQE. Among these materials, PEDOT:PSS remains the only HTL widely used in commercial organic/perovskite optoelectronic devices [47].

A series of PEDOT:PSS products have been developed. Among these, PEDOT:PSS aqueous solutions (Clevios^{TM}) are widely used in laboratory-scale electronics. For instance, Clevios^{TM} PH500, PH510, and PH1000 are commonly employed for preparing flexible and stretchable electrodes, while Clevios^{TM} P VP AI 4083, Solar, and P VP8000 are primarily used as hole-transporting/injection layers. As a complex composed of substituted polythiophene and polyanionic compounds, PEDOT:PSS films exhibit high uniformity and smoothness. After chemical doping treatment, PEDOT:PSS films with a thickness of 30–40 nm at $\lambda = 550\,\text{nm}$ demonstrate over 92% optical transparency. Their tunable conductivity ranges from 10^{-3} to $10^{3}\,\text{S}\,\text{cm}^{-1}$, and the adjustable work function spans 4.7–5.3 eV. Additionally, PEDOT:PSS exhibits superior mechanical flexibility, with the ability to endure tensile strains exceeding 20% [48].

Despite these advantages, PEDOT:PSS has notable drawbacks, such as hydrophilic, which causes moisture absorption and accelerates perovskite degradation [5, 38]. This issue can be mitigated by

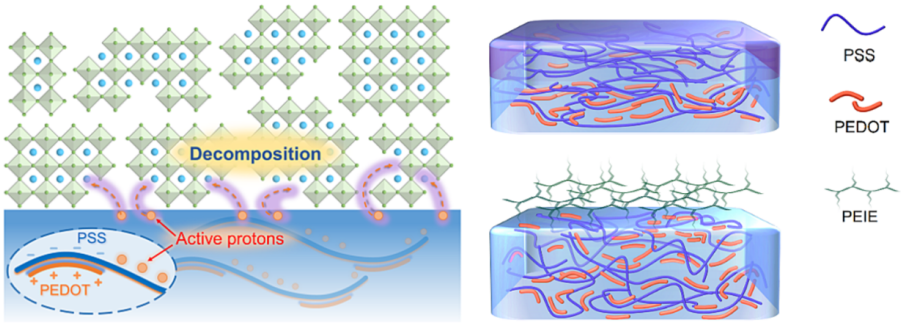

Figure 1-6: Schematic of PSSH degradation and PEIE neutralization [51].

preparing films under low-humidity conditions ($RH < 40\%$) [49]. Doping PEDOT:PSS with hydrophobic materials is another effective strategy. Yang et al. doped PEDOT:PSS with poly(3-hexylthiophene-2,5-diyl) (P3HT), enhancing hydrophobicity and increasing the PCE of PSCs from 17.04% to 19.78% [50].

Another issue with PEDOT:PSS is its corrosive effect on ITO. PEDOT exhibits acidity, which can corrode both the ITO and the perovskite layer, thereby reducing the optoelectronic performance of devices [38]. Neutralization has become a primary strategy for researchers to address this problem.

Peng et al. focused on modifying the PSSH component in PEDOT:PSS. They discovered that PSSH, a component of PEDOT:PSS, releases protons that contribute to the degradation of perovskites. By using polyethylenimine ethoxylated (PEIE), which binds with PSSH, they effectively protected the perovskite layer (Fig. 1-6(d)(e)). Their results showed that PeLEDs based on PEDOT:PSS/PEIE achieved efficiencies over seven times higher than the original devices [51].

Metal Oxide: MOs represent another promising class of HTL materials, offering solutions to the issues of acidity and hygroscopicity associated with PEDOT:PSS, which can degrade device efficiency. MOs are more environmentally stable, non-toxic, cost-effective, and can be deposited using solution-based methods[52].

However, MOs face challenges related to optical transparency due to band-to-band and intra-band absorption, as well as suppression of transparency below the plasma oscillation frequency. There is typically a trade-off between conductivity and transparency in MOs. For MOs used as HTLs, a slight reduction in conductivity can be acceptable, as reducing the HTL thickness can still enhance charge transport efficiency[52].

Nevertheless, this approach introduces additional challenges, such as ensuring the compactness and uniformity of the intermediate layer to avoid pinholes. This consideration is particularly critical when fabricating HTLs through solution-based methods[52].

Currently, common MOs used as HTLs include NiO_x and CuO_x. Additionally, other MOs with high work functions, such as MoO_3, V_2O_5, and $CuCrO_2$, have also been reported [53]. Compared to CuO_x, NiO_x has demonstrated superior performance, primarily due to its higher optical transparency and ease of processing. Solution-processed NiO_x has been deposited using various techniques, including electrodeposition, sol-gel-derived thin films, spray deposition, and nanoparticle formation [52]. These methods make NiO_x a versatile and scalable choice for HTL applications.

Bai et al. successfully optimized the performance of NiO_x-based HTLs by controlling the Mg doping concentration in NiO_x. This approach ensured the film exhibited suitable conductivity (with an electron mobility of $4.91 \times 10^{-4}\,\mathrm{cm^2V^{-1}}$ under an applied voltage of 5.44 V) and high transmittance for incident light in the 520–540 nm range. Moreover, their HTL design, incorporating $Ni_{0.9}Mg_{0.1}O_x$/PVK/PEG, significantly reduced the hole injection barrier. This design enabled the achievement of a record EQE of 30.84% [37].

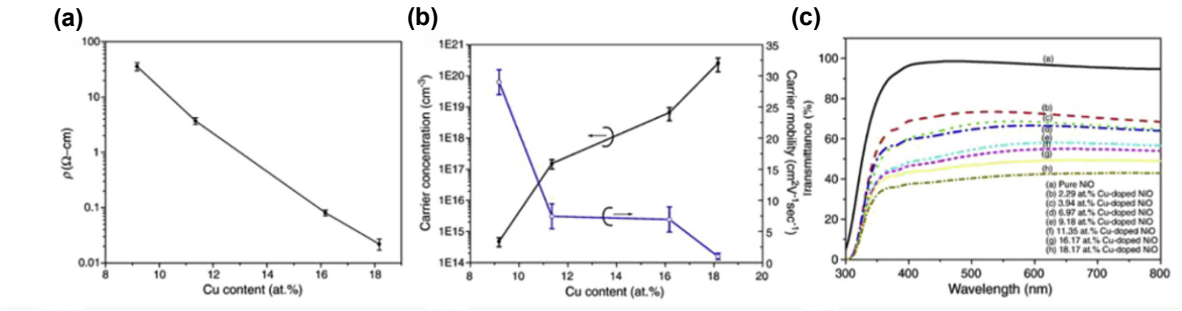

Figure 1-7: (a) Resistivity, (b) Hall measurements, (c) spectral transmittance of Cu-doped NiO_x films with different Cu contents[54].

1.2.2 Common Electron Transport Layer in Perovskite Light Emitting Diodes

Compared to the diverse HTL systems, most studies consistently select 1,3,5-Tris(1-phenyl-1H-benzimidazol-2-yl)benzene (TPBi) as the ETL for PeLEDs. This preference arises from both the higher electron effective mass discussed previously and TPBi's excellent electro-optical properties.

Undoped TPBi exhibits a HOMO of approximately -6.2 eV and LUMO of -2.7 eV, demonstrating favorable energy level alignment [55] and a high electron mobility of $1.0 \times 10^{-4} cm^2 V^{-1} s^{-1}$. Additionally, TPBi shows a high glass transition temperature, and its interface with the EML effectively passivates interfacial defects [56].

However, the higher electron mobility in TPBi layers relative to hole transport layers causes excessive electron overflow into HTLs, inducing substantial non-radiative recombination that reduces device efficiency. Consequently, several TPBi optimizations have been developed. One approach reduces electron mobility, exemplified by Liu et al. who incorporated tris(8-hydroxyquinoline)aluminum (Alq_3) into TPBi-based ETLs. This modification balanced electron and hole mobilities, ultimately enhancing EQE [57]. Alternatively, introducing electron-blocking layers (EBLs) at the EML/HTL interface effectively balances carrier injection. For instance, Bai et al. implemented polyethylene glycol (PEG) as an EBL to suppress excessive electron injection [37].

Although the method of blocking excess electrons has made some achievement in the current PeLEDs system, from a long-term perspective, enhancing hole mobility in HTLs to match the electron mobility of TPBi layers represents a more sustainable approach for boosting PeLED luminance.

1.3 Research Objectives

This chapter commences with contemporary global energy challenges, highlighting the cost and color-rendering advantages of PeLEDs over conventional LEDs as next-generation lighting technology. It subsequently examines the operational principles of PeLEDs, optimization strategies for the critical EML, and recent advances in complementary HTLs/ETLs. The analysis demonstrates that synergistic passivation using large and small A-site ligands constitutes the most effective approach for defect suppression in perovskite layers. Concurrently, the chapter underscores the imperative to enhance HTL hole transport efficiency and passivate interfacial defects.

The primary objective of this Master's thesis project is to develop a working PeLEDs, establishing a fabrication and characterization framework for the PVMD group. It should be emphasized that this work constitutes the PVMD group's pioneering effort in PeLED fabrication, with no prior device testing or characterization baseline processes. Consequently, this thesis requires comprehensive development of the PeLED architecture through sequential layer-by-layer design. While commercially sourced ITO/glass substrates and established photovoltaic electrode processes provide foundational elements, our primary focus centers on designing and fabricating the three core functional layers:

the HTL, EML and ETL. The challenges mentioned above are addressed in the following research objectives::

1. **Enhance perovskite stability against ambient moisture to enable reliable data acquisition.** As in all characterization techniques used in this study, except for device-level PeLED testing (as detailed in Sec.2.4), require access to equipments within the Optoelectronic Materials (OMs) Group at TU Delft's TNW Faculty. Notably, these instruments lack comprehensive nitrogen atmosphere protection. With the exception of vacuum-required techniques such as scanning electron microscopy (SEM), all measurements are conducted under ambient atmospheric conditions. This requires implementation of protective strategies to mitigate moisture-induced degradation of perovskite samples during characterization.

2. **Establish quantum efficiency characterization protocols for both PLQY (EML) and EQE (PeLEDs).** Current PLQY characterization utilizes the FLS 980 set-up within the OMs Group facility. Although this instrument includes thin-film measurement capabilities, this functionality remained unused prior to our work. During initial testing, we identified significant alignment issues that introduced substantial measurement uncertainty. Optimization of the optical configuration is therefore required to obtain reliable quantitative data. Concurrently, the absence of dedicated EQE measurement set-up presents a separate challenge. To address this limitation, our approach involves extracting critical material parameters through alternative characterization methods, and developing a specialized EQE test platform with appropriate spectral calibration and current-voltage-luminance synchronization capabilities.

3. **Investigate the impact of TPBi thickness on PeLEDs' optical performance.** Though we find thermal evaporation deposition is the predominant method for TPBi layer fabrication, this approach risks contaminating the deposition chamber in the thermal evaporation system of PVMD group. Therefore, we propose using spin coating as an alternative deposition technique. However, thickness variations inherent to spin coating may interfere with optical interference phenomena, potentially substantially altering the device's optical characteristics. To quantitatively evaluate this thickness-dependent effect, we need to do optical modeling and simulation approaches to predict performance outcomes across the anticipated thickness range.

4. **Develop high-photoluminescence EML through A-site doping and additive engineering.** To achieve high-efficiency perovskite LEDs, we need optimize the EML through controllable processing parameters. This requires simultaneous attainment of four critical characteristics: (1) precise spectral tuning of the emission peak, (2) enhanced crystalline quality, (3) improved morphological uniformity, thereby maximized PLQY.

5. **Adapt existing self-assembled monolayer (SAM) recipes from the PVMD group's PSC protocols for HTL fabrication in PeLEDs.** As PVMD group has demonstrated expertise in SAM-based HTLs for photovoltaics. Implementation of optimized SAM recipes will streamline device development and eliminating redundant process optimization.

6. **Fabricate a operational PeLEDs, analyze their optoelectronic characteristics, and elucidate the functional mechanisms of SAMs within PeLED.**

2 Methodology

As established in the preceding chapter, defects in metal halide perovskites (MHPs) critically determine the operational efficiency of PeLEDs. These defects arise from both composition-dependent factors and fabrication process parameters. This chapter delineates common fabrication processes and characterization techniques for state-of-the-art PeLEDs.

2.1 Simulation

This report utilizes COMSOL Multiphysics software to simulate light propagation in Multi-film structure.

COMSOL Multiphysics® features two defining characteristics: First, the "COMSOL" acronym represents computational solutions. Complex geometries often preclude analytical solutions to partial differential equations (PDEs). The finite element method (FEM) addresses this by subdividing physical systems into discrete elements. These finite elements are interconnected through boundary conditions, assembling local equations into global systems. The solution approximates the PDE through variational methods that minimize error functionals.

Second, "Multiphysics" denotes coupled physics simulation. Integrated multiphysics interfaces enable simultaneous modeling of interacting phenomena (e.g., heat transfer, fluid dynamics, electromagnetics, structural mechanics). This framework integrates diverse formulations and solvers, allowing users to define parameters, geometry, boundary conditions, and meshing for streamlined computation.

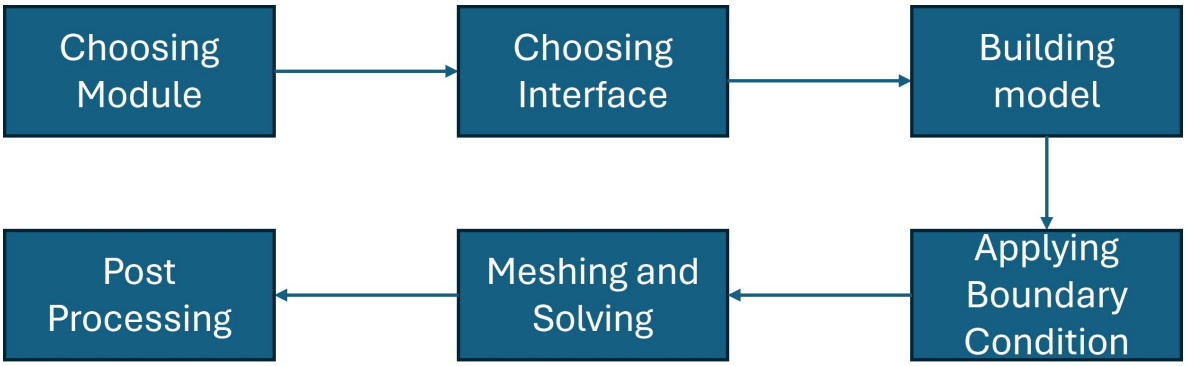

Figure 2-1: Flowchart for using COMSOL Multiphysics

The software provides specialized optical modules: - **Wave Optics**: Computes electromagnetic fields when wavelengths are comparable to device features (e.g., nanophotonics, plasmonics, waveguides, light scattering) - **Geometric Optics**: Models ray propagation when wavelengths are negligible relative to geometry, calculating intensity, phase, and optical path length

For PeLED optical interference simulations, the wave optics module is essential given nanoscale layer thicknesses (∼10-100 nm).

2.1.1 Interface in Wave Optic Module

This module contains multiple physics interfaces (nodes). Different interfaces couple Maxwell's equations with optical response equations of various materials, thereby transforming them into different partial differential equations (PDEs). The Wave Optics Module provides four core interfaces[58]: The Electromagnetic Waves, Frequency Domain Interface (ewfd), The Electromagnetic Waves, Transient Interface (ewt), The Electromagnetic Waves, Time Explicit Interface (teew), and The Electromagnetic Waves, Beam Envelopes Interface (ewbe).

The ewfd interface solves frequency-domain wave equations for electric fields, primarily modeling the propagation of electromagnetic waves through different media and structures. By reformulating equations, it solves eigenvalue problems to determine the eigenfrequencies of structures, or calculates propagation modes in waveguides and transmission lines at specified frequencies. Typical applications include waveguide devices, grating structures, and light scattering analysis of small particles[58].

The ewt interface solves time-domain wave equations for electric fields, mainly applied to electromagnetic wave propagation problems requiring time-domain solutions, such as non-sinusoidal waveform propagation or interactions in nonlinear media. Typical application cases cover electromagnetic pulse transmission and harmonic generation in nonlinear optical media[58].

The teew interface solves systems of first-order partial differential equations for electric and magnetic fields (Faraday's law and Maxwell-Ampère's law) using the time-explicit discontinuous Galerkin method. Excitation sources can be bulk currents/magnetic currents or boundary surface currents/-fields. This interface primarily simulates electromagnetic wave propagation in linear media, with typical applications including transient transmission of electromagnetic pulses[58].

The ewbe interface solves frequency-domain wave equations for single or dual electric field envelopes, where the electric field is expressed as the product of the field envelope and a rapidly oscillating predefined phase function. Since the spatial variation of the field envelope is slower than the original electric field, coarser meshing can be employed. Therefore, the Beam Envelopes interface is suitable for simulating large-scale optical structures (dimensions much larger than the wavelength). Excitation sources can be incident fields at boundaries, surface currents, or boundary electromagnetic fields. This interface can handle transmission problems at fixed frequencies and eigenfrequency solutions for resonant structures. Typical applications include waveguide devices (e.g., directional couplers), nonlinear optical effects, and laser beam transmission[58].

In this work, simulations of PeLEDs exhibit the following characteristics: 1. Spatial scale: Optical response structures are smaller than the excitation wavelength (this work uses 530 n m green light excitation, with thickest layer 120 nm and thinnest layer 2 nm). Since structural dimensions are smaller than excitation wavelength, ewbe interface is not suitable. 2. Temporal scale: Under steady-state illumination, changes in device optical response are extremely slow and can be regarded as constant, eliminating the need to obtain time-dependent response functions. Therefore, ewt and teew interfaces are unsuitable. In summary, the ewfd interface is the optimal choice for this work. The next section will detail the governing equations used by this interface.

2.1.2 Principal Equation Employed by The Electromagnetic Waves, Frequency Domain Interface

COMSOL's ewfd interface includes two main solvers: the eigenfrequency solver, used to determine the eigen frequencies of structures, and the frequency solver, used to analyze device responses to specific light frequencies.

Maxwell's equations (Eq. 2-1) describe all macroscopic electromagnetics, including wave and geometric optics. To simplify the analysis of light propagation in photonic crystals, we apply four key assumptions:

1. Neglect nonlinear effects due to low electric field strength. 2. Assume isotropic materials, allowing $\vec{D} = \epsilon \cdot \vec{E}$. 3. Ignore material dispersion outside the frequency range, treating dielectric constants as constant. 4. Assume lossless materials with real, positive dielectric constants.

$$\begin{cases} \nabla \cdot \vec{B} = 0, \nabla \times \vec{E} + \frac{\partial \vec{B}}{\partial t} = 0 \\ \nabla \cdot \vec{D} = \rho, \nabla \times \vec{H} - \frac{\partial \vec{D}}{\partial t} = \vec{J} \end{cases} \tag{2-1}$$

With these assumptions, Maxwell's equations reduce to the principal equation for structure light propagation (Eq. 2-2), which resembles an eigenvalue problem similar to the Schrödinger equation (Eq. 2-3), explaining the optical band structure observed in some structure, akin to semiconductors.

$$\nabla \times \left(\frac{1}{\epsilon(\vec{r})} \nabla \times \vec{H}(\vec{r}) \right) = \left(\frac{\omega}{c} \right)^2 \vec{H}(\vec{r}) \tag{2-2}$$

$$\Theta \vec{H}(\vec{r}) = \left(\frac{\omega}{c} \right)^2 \vec{H}(\vec{r}), \quad \Theta = \nabla \times \left(\frac{1}{\epsilon(\vec{r})} \nabla \times \right) \tag{2-3}$$

With a known dielectric constant, this equation simplifies to an eigenvalue problem, $Ax = \omega^2 Bx$, where A and B are matrices and x is the eigenvector. Solving for eigenvalues reveals allowed modes in the system, forming a band diagram—basis for the eigenfrequency solver.

For analyzing transmission and reflection, the frequency domain solver models finite structures, adding a constant-frequency current source $\vec{J}(\vec{r})e^{-i\omega t}$ to Maxwell's equations. The frequency response equation (Eq. 2-4) includes an additional current term, allowing the solver to iteratively calculate electric field distribution based on known currents.

$$\left[\nabla \times \nabla \times - \frac{\omega^2}{c^2} \epsilon(\vec{r}) \right] \vec{E}(\vec{r}) = i\omega\mu_0 \vec{J}(\vec{r}) \tag{2-4}$$

2.1.3 Model Building

Regarding model building, COMSOL provides three-dimensional, two-dimensional, and one-dimensional modeling approaches. In this thesis work, excluding the substrate (glass), the total device thickness does not exceed 1 μm, while the sample dimensions measure 2.5×2.5 cm^2 - a difference exceeding 10^4. This substantial dimensional contrast permits approximation as an infinitely extended plane in two dimensions, meaning the structure varies only along one dimension. However, due to the requirement to simulate the structure's response to light incident at various angles, we employ two-dimensional modeling.

2.1.4 Boundary Condition

This chapter primarily employs three boundary conditions: Continuous, Port, and Periodic Boundary Condition. Their descriptions follow[58].

1. Continuity: Ensures continuity of parameters across internal boundaries without abrupt changes.

2. Port boundary conditions are used when electromagnetic energy enters or exits the model. A port boundary condition can absorb or launch specific modes. Among the options provided in the Port boundary condition settings, this thesis uses the simplest periodic port to define our incident mode. In the port interface, an electric field oriented along (001) defines the TE wave, while a magnetic field oriented along (001) defines the TM wave.

3. Periodic Boundary Condition: The periodic condition establishes mappings between geometrically identical source and destination boundaries. Three periodic condition types are available: Continuity - Tangential solution components are equal on source/destination boundaries; Antiperiodicity - Tangential components have opposite signs; Floquet periodicity - Tangential components exhibit phase shifts determined by the wave vector and source-destination distance. Floquet periodicity is typically used for plane waves interacting with periodic structures. This thesis uses Floquet periodic boundary condition with "From periodic port" to obtain the k-vector for Floquet periodicity.

2.2 Fabrication

In this project, the CTL and EML are fabricated by spin coating, and the electrode is fabricated by thermal evaporation deposition (TED).Therefore, This section will first introduce spin coating and focus on its application in MHPs. Then the principle of TED will be given.

2.2.1 Spin Coating

Spin coating is a widely used technique for creating uniform thin films on flat substrates. The process begins by depositing a small droplet of precursor solution at the substrate's center, followed by rapid spinning, typically at speeds around 3000 rpm. The centrifugal force spreads the solution evenly across the substrate and removes excess material at the edges, leaving behind a thin film. The film's thickness and properties depend on factors such as the precursor solution's characteristics (e.g., viscosity, drying rate, solid content, surface tension) and the spin-coating parameters (e.g., acceleration, rotational speed, spin time). The device used for this process is commonly referred to as a spin coater or spinner [59].

Spin coating involves four key stages. The first is the dispense stage, which can be performed statically or dynamically. In static dispense, a droplet of fluid is deposited at the center of the substrate, with the droplet size determined by the fluid's viscosity and the substrate's dimensions. In dynamic dispense, the substrate rotates at a low speed during the fluid deposition, spreading the solution across the surface and reducing material waste. Dynamic dispense is particularly useful when the wetting properties between the fluid and substrate are poor, as it minimizes potential voids [59].

The second stage, substrate acceleration, involves rapidly increasing the substrate's rotation speed. This motion expels most of the fluid from the surface. During this stage, spiral streaks may temporarily appear due to inertial effects caused by the twisting motion of the fluid layer as it accelerates. Once the fluid layer becomes sufficiently thin, it rotates uniformly with the substrate. Generally, higher rotation speeds and longer spin times during this stage result in thinner films [59].

The third stage is fluid thinning, where the fluid layer continues to decrease in thickness. However, edge effects can cause slight variations in the coating's thickness near the substrate's perimeter. As the fluid flows outward uniformly, it forms droplets at the edges before being expelled, leading to these minor inconsistencies [59].

The final stage is the solvent evaporation stage. In this phase, the flow of the fluid stops due to increased viscosity, and solvent evaporation becomes the dominant process. As the solvent evaporates, the viscosity of the remaining liquid increases, ultimately solidifying the film into its final form [59].

Spin coating has become a well-established method for fabricating MHPs films, leveraging the strong ionic interactions between metal cations and halide anions. During the process, precursors composed of metal halides $BX(_2)$ and organic or inorganic halides AX undergo convective self-assembly, resulting in well-crystallized perovskite structures. To optimize crystallization dynamics and kinetics, two additional steps are often integrated into the standard spin-coating procedure for PeLED synthesis: the use of anti-solvent and annealing [60].

The anti-solvent step involves adding a solvent that does not dissolve the perovskite material but is miscible with the precursor solvent (e.g., γ-butyrolactone (GBL), DMF, DMSO, or N-methyl-2-pyrrolidone). Common anti-solvents, such as toluene or chloroform, are applied during the uniform rotation phase. This technique reduces the solubility of the precursor solution, inducing the early precipitation of perovskite materials and promoting uniform crystallization. For example, Xiao et al. developed a fast deposition-crystallization (FDC) procedure, where an anti-solvent was added to a precursor solution in DMF during the first few seconds of spin coating. Conducted in a nitrogen-filled glovebox, this approach produced compact films with complete surface coverage. Without anti-solvent, uncontrolled needle-like structures formed on the substrate (Fig. 2-2(a)) [61].

CB has proven to be an effective anti-solvent, particularly when applied 4–6 seconds after reaching a constant spin rate. During the first 3 seconds at 5000 rpm, removing excess precursor solution dominates. Adding CB during this period leads to incomplete surface coverage because the solution has not yet reached saturation. Between 4–6 seconds, solvent evaporation concentrates the precursor solution, and adding CB promotes the formation of dense and uniform films. Beyond 7 seconds, the drying process begins, and anti-solvent addition has little effect. The immediate darkening of the film upon CB addition (yellow to light brown) signals the initiation of crystallization. Subsequent annealing at 100°C for 10 minutes fully solidifies the film, producing micrometer-sized crystals with large grains free of vertical boundaries, which enhance charge transport and recombination dynamics (Fig. 2-2(c))

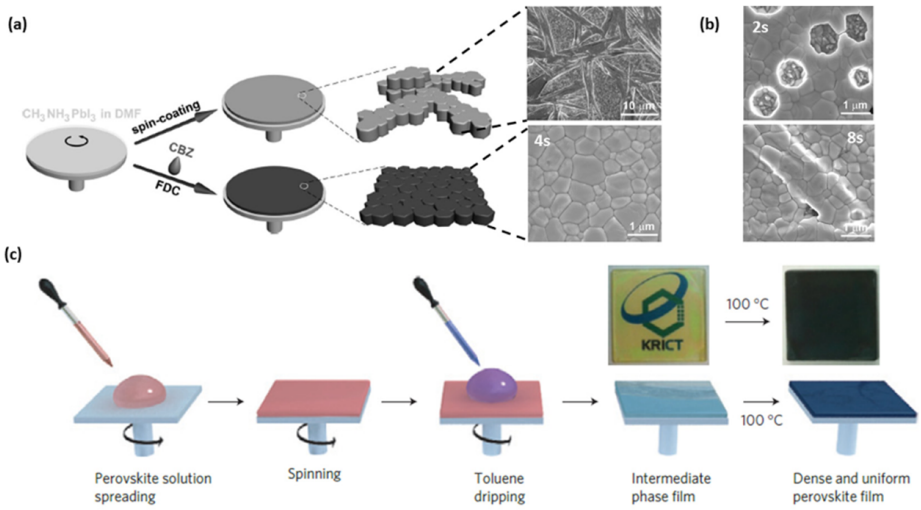

Figure 2-2: (a) Schematic illustration of anti-solvent dripping and conventional spin-coating process for fabricating perovskite films. Conventional spin-coating results in a gray film composed of rod-like crystals. Anti-solvent dripping forms a light brown film consisting of uniformly sized perovskite grains [61]. (b) SEM images of the surface morphology of films prepared by adding anti-solvent at different delay times (after 2 s and 8 s) [61]. A delay time between 4 and 6 s produces optimal morphology. (c) Conventional perovskite processing[61].

[61].

Annealing is a critical step for completing the crystallization of spin-coated perovskite films. By applying controlled temperatures, annealing facilitates phase transitions and improves film quality. Grazing-incidence wide-angle X-ray scattering (GIWAXS) is often used to study these transitions. For instance, Wiesner et al. observed the thermally induced structural evolution of $MAPbI_{3-x}Cl_x$, noting a crystalline precursor peak at $q = 11\,\mathrm{nm}^{-1}$ at the experiment's onset. After 50 minutes at 80°C, this precursor transitioned into polycrystalline perovskite, completing the transformation at 90°C after 60 minutes [62].

The annealing window must be carefully selected to ensure high-quality perovskite formation. Minchao Qin et al. used GIWAXS to reveal the detailed crystallization process of mixed perovskites during spin coating. They identified three stages: the precursor solution stage (Stage 1), where anti-solvent had not yet been added; the hexagonal δ-phase stage (Stage 2), marked by solvent evaporation and film thickening; and the complex phases stage (Stage 3), where solid perovskite forms. They emphasized that annealing during Stage 2 prevents the formation of hexagonal polytypes. Additionally, incorporating Cs^+ into the perovskite extends the annealing window, enabling greater control over the crystallization process (Fig. 2-3) [63].

2.2.2 Thermal Evaporation Deposition

TED is one of the earliest and most widely used coating technologies. It involves heating raw materials to vaporize them, followed by deposition onto a substrate under high vacuum conditions. This technique is extensively applied in the semiconductor industry, particularly for OLEDs and thin-film photovoltaics. TED comprises three main stages. The first stage is vaporization, where the material is heated to a temperature sufficient to vaporize a significant number of its atoms or molecules. The second stage, transport, takes place in a high-vacuum environment, ensuring that the vapor travels from the source to the substrate without collisions. The final stage, deposition and film growth, occurs when vaporized atoms or molecules condense on the substrate, nucleating and forming a thin film [43].

The mechanisms governing thin-film growth include the Volmer-Weber mode (island growth), the

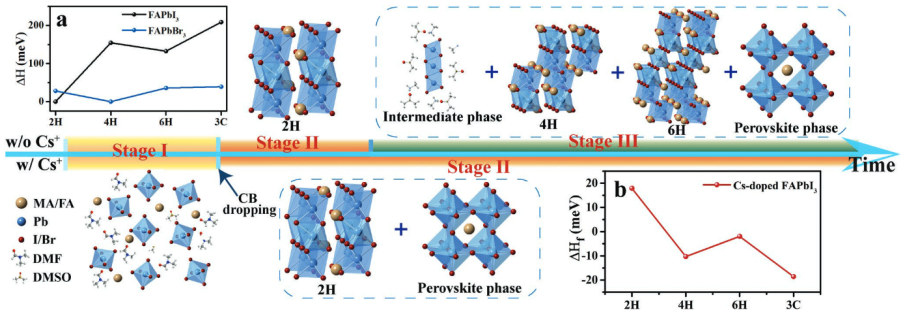

Figure 2-3: Schematics of phase transition pathways and DFT results. Phase transition pathways of mixed perovskites without and with Cs^+ during the spin-coating operation: (a) Formation energy (ΔH) of $FAPbI_3$ and $FAPbBr_3$ relative to the most stable structure, and (b) formation energy gain per formula unit at 12.5% Cs^+ doping relative to the undoped case [63].

Frank-Van der Merwe mode (layer growth), and the Stranski-Krastanov mode (layer-island growth) (Fig. 2-4(c)). In the Volmer-Weber mode, atoms or molecules nucleate directly as islands on the substrate, which later coalesce into a continuous polycrystalline film. This mode is prevalent when the bonding among adsorbates is stronger than their interaction with the substrate. Conversely, the Frank-Van der Merwe mode occurs when the bonding between atoms and the substrate is stronger, leading to layer-by-layer growth, often observed in epitaxial systems. When the two interactions are comparable, the Stranski-Krastanov mode emerges, combining layered and island growth. For PeLEDs with heterojunction structures, the substrate lattice generally does not match the perovskite material's lattice, resulting in films that predominantly grow via the Volmer-Weber mode [43].

If TED is simplified to a point evaporation source model (Fig. 2-4(b)), the deposition rate onto the substrate, measured as the number of ions condensed per unit area per unit time (N_d), can be expressed as:

$$N_d = \frac{N_e A \cos\theta}{4\pi r^2} a_1 \tag{2-5}$$

Here, a_1 is the sticking coefficient, A is the source area, r is the distance from the source to the substrate, and θ is the angle relative to the substrate's normal direction. The evaporation rate N_e, defined as the number of atoms or molecules leaving the surface per unit time, is given by:

$$N_e = \frac{a_2(p - p_0)}{\sqrt{2\pi m_k T}} \tag{2-6}$$

In this equation, m_0 is the molecular mass, k is Boltzmann's constant, T is the evaporation temperature, and p and p_0 are the saturated vapor pressure and hydrostatic pressure, respectively. The evaporation coefficient a_2 depends on the surface condition [43].

2.2.3 Fabrication in This Work

Materials: All of the reagents and chemicals employed in this work were purchased from commercial sources and used as received. Formamidinium bromide (FABr; 99.99%) and Phenethylammonium bromide (PEABr; powder) were purchased from Greatcell Solar Material. Lead(II) Bromide ($PbBr_2$; 99.999%) and Potassium bromode (KBr; 99%) were purchased from the Millipore-Sigma. 2,2',2"-(1,3,5-Benzenetriyl)tris(1-phenyl-1H-benzimidazole) (TPBi; 98%) were purchased from TCI AMERICA. Toluene anhydrous (TL; 99.8%)were purchased from Sigma-Aldrich. All SAMs molecules include [2-(9H-Carbazol-9-yl)ethyl]phosphonic Acid (2PACz; 98.0%), [2-(3,6-Dimethoxy-9H-carbazol-9-yl)ethyl]phosphonic Acid (MeO-2PACz; 98.0%) and [4-(3,6-Dimethoxy-9H-carbazol-9-yl)butyl]phosphonic Acid (MeO-4PACz, 98%) are purchased from TCI. All solvent, include Ethanol

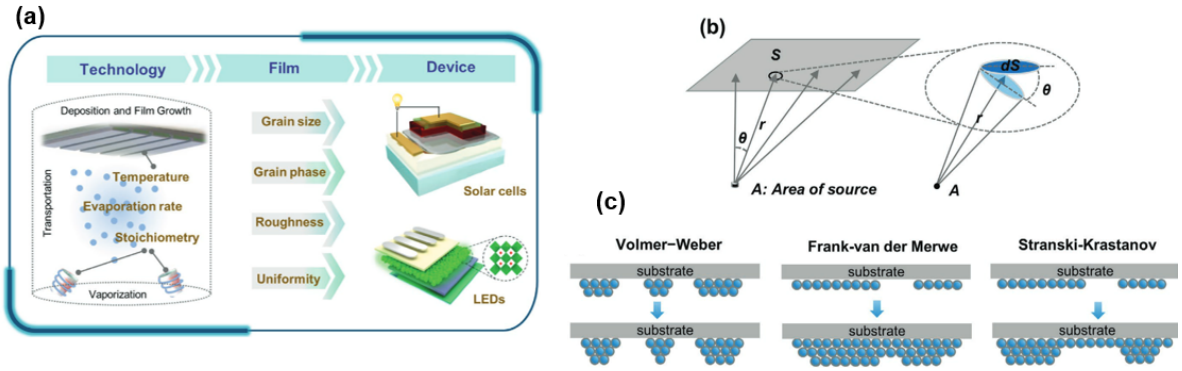

Figure 2-4: (a) Thermal evaporation procedures, illustrating how technological parameters affect film quality and device performance. The evaporation chamber schematic is reproduced with permission. (b) Schematic diagram of the point evaporation source. (c) Growth mechanisms of perovskite films[43].

(EtOH; 99.5%), Ethyl acetate (EA; 99.9%), Toluene (TL; 99.8%), 2-Propanol (IPA; 99.8%), Chlorobenzene (CB; 99.8%) and N,N-Dimethylformamide (DMF; 99.8%), Dimethyl sulfoxide (DMSO; 99.9%).

Perovskite and CTL Precursor Preparation: The perovskite precursor solutions were prepared according to previously reported methods. The perovskite precursor solution was prepared by dissolving $PbBr_2$, FABr, and PEABr with a molar ratio of 3:2:2 were dissolved in a mixed solvent (V_{DMSO}:V_{DMF} = 1:4). The concentration of Pb_{2+} was kept at 0.5 mol/L. The solution was stirred overnight to obtain the perovskite precursor solution. The solution was filtered through 0.20 μm PTFE syringe filter and the concentration of Pb_{2+} was diluted to 0.25 mol/L before using. To add KBr and 2PACz into perovskite precursor, they were firstly dissolved in a mixed solvent (V_{DMSO}:V_{DMF} = 1:4) with the concentration of 5 mg/ml for KBr and 10 mg/ml 2PACz. Varying amounts of additive solution were added into pervoskite precursor with the concentration of Pb^{2+} kept at 0.5 mol/L and diluted solution with the concentration of Pb^{2+} to 0.25 mol/L. The ETL solution was prepared by dissolving TPBi to a concentration of 5.0 mg/ml in CB. The HTL solutions was prepared by dissolving NiO_x nanoparticle into dionized water to a concentration of 20 mg/ml. SAMs precursor was prepared by dissolving MeO-2PACz and MeO-4PACz with the molar ratio of 1:1 into ethanol to a concentration of 4 mg/ml.

Device Fabrication: The ITO coated glass substrates were sequentially 15 mins ultrasonic cleaning with detergent, deionized water, deionized water, anhydrous ethanol. followed by blowing dry with nitrogen gun. The cleaned substrates were ultraviolet ozone treated for 20 min before use. NiO_x was layer was prepared by spin-coating at 3000 rpm for 30 s and annealling 150°C for 30 min. SAMs layer was prepared by spin coating at 3000 rpm for 60 s and annealling 120°C for 15 min. Perovskite layer was prepared by spin coating at 4000 rpm for 60 s,antisolvent (toluene) was dropped quickly onto the surface after 20 s, followed by annealing at 80 °C for 10 min. TPBi layer was spin-coated at 2000 rpm for 60 s, placed in the transition chamber, applied negative pressure, and vacuum dried for 20 min. Finally, 21 nm LiF and ***80*** nm Ag were thermally evaporated under a vacuum of 2×10^{-3} Pa through a shadow mask to produce a 0.09 cm^2 active area.

EML film Encapsulation: EML was encapsulated by PMMA, PMMA precursor was prepared by dissolving PMMA to a concentration of 20 mg/ml in EA. film was prepared by dynamic spin coating, firstly spining at 1000 rpm for 10s, followed by spinning at 4000 rpm, 30s. Applying precursor at first 10 s.

2.3 Characterization

For PeLEDs, we typically conduct characterizations both on the EML layer films and the device level. At the EML level, for quasi-2D MHPs-based EML, we focus on their emission color and efficiency.

The color is primarily determined by the n-phase distribution, while the efficiency is mainly influenced by the crystallinity and composition of the MHPs. This necessitates a multi-angle understanding of the MHPs film formation. In this chapter, we will first introduce the phase characterization of MHPs, followed by their morphology characterization, and finally describe how we employ different PL techniques to evaluate the comprehensive performance of MHPs.

At the device level, due to the lack of commercial options, this chapter will focus on the establishment and application of our LED test instrument.

2.3.1 Phase Characterization

For MHPs, we focus on two types of phase distributions: the n-phase distributhe crystalline phase. The n-phase distribution affects the bandgap of MHPs and determines the PL emission peak of perovskites. Typically, we use Ultraviolet-Visible (UV-Vis) Spectroscopy to observe the n-phase distribution of perovskites. The second type is the crystalline phase; in practical perovskite preparation, it's challenging to prepare completely crystalline MHPs. To improve the efficiency and color purity of EML, we aim for higher and more uniform crystalline phases in EML, which can be characterized by X-Ray Difraction (XRD). This section will introduce the roles of these phases and provide methods to analyze their properties.

Ultraviolet-Visible Spectroscopy: In its broadest sense, UV-Vis spectroscopy examines the interaction between electromagnetic radiation in the ultraviolet and visible regions and matter. The UV spectrum is typically divided into three main regions: UVA (320–380 nm), UVB (280–320 nm), and UVC (100–280 nm). The visible light region generally covers the 380–750 nm spectral range. UV-Vis spectroscopy is associated with the excitation of outermost electrons in atoms, which participate in molecular bonding, and is thus often referred to as "electronic spectroscopy". Measurements in the UV-Vis region are commonly conducted in transmission, reflectance modes, which require a reference material for calibration[64].

In Quasi-2D MHPs-based EML, researchers often use UV-Vis spectroscopy to measure the absorption capability of perovskite materials across different incident wavelengths. Due to the quantum confinement effect, perovskites with different n-phase structures have varying bandgaps, resulting in distinct peak wavelengths in their absorption spectra. As a result, UV-Vis spectroscopy can be employed to analyze the n-phase distribution of low-dimensional perovskites [26, 65].

The formation of quasi-2D perovskites depends on both the binding energy between large A-site dopants (introduced in Sec.1.1.3) and the perovskite framework, and the stoichiometric ratio of large A-site dopants to Pb^{2+}. However, solution-processing kinetics invariably yield multiple n-phase distributions, as evidenced by UV-Vis spectroscopy in Fig. 2-5(a). Distinct absorption peaks correspond to different n-phases, demonstrating that incorporating 1,6-hexanediammonium (HDA) ligands into 1,10-decanediammonium (DDA) effectively suppresses high-n-phase formation [65].

Notably, different multilayered halide perovskites (MHPs) sharing the same n-phase exhibit variations in bandgap and absorption peak positions. Therefore, identifying which n-phase corresponds to the peaks observed in UV-Vis absorption spectra requires referencing established literature reports [65, 37].

X-Ray Diffraction: X-ray Diffraction (XRD) utilizes the elastic scattering of light, also known as Rayleigh scattering. This scattering typically occurs when photons interact with electrons around atomic nuclei. In this process, the scattered wavelength remains unchanged, and the initial phase of the incident light is preserved. However, due to the periodic nature of the crystal structure, coherent or destructive scattering occurs, which can be described by Bragg's law (Eq. 2-7) [68]:

$$n\lambda = 2d_{hkl}sin(\theta) \tag{2-7}$$

Where, n represents the order of diffraction, λ is the wavelength of the incident beam, d_{hkl} denotes the lattice spacing, and θ is the diffraction angle in degrees. In polycrystalline, fine-grained, and texture-free materials, diffraction can occur from all crystal planes and orientations that satisfy Bragg's

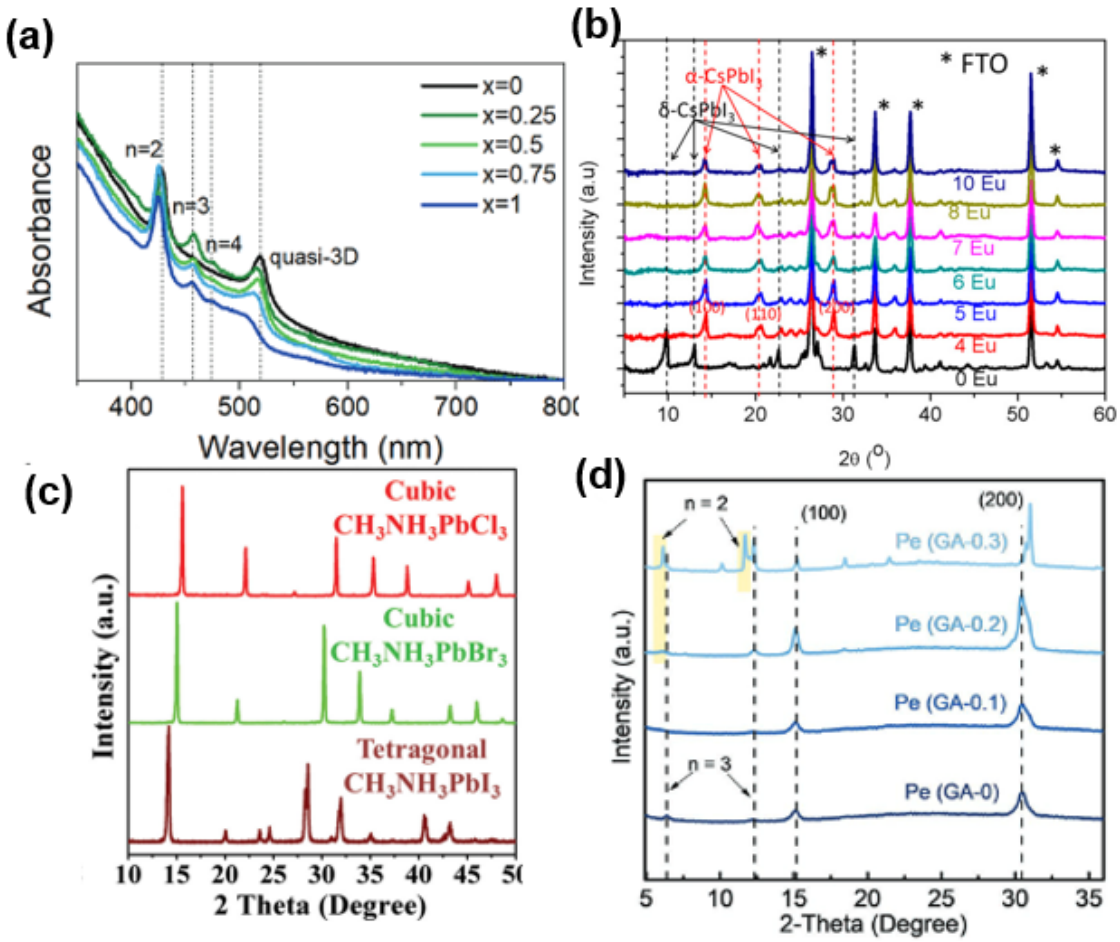

Figure 2-5: (a)Absorption spectra (with indicated peak positions corresponding to different phases) of $(DDA_xHDA_{1-x})Cs_{n-1}PPb_nBr_{3n+1}$, [65] (b) XRD patterns of $CsPbI_3$:xEu (x = 4,5,6,7,8,and 10 mol %) films (Cu K_α) [21] (c) Comparison of bulk perovskite with different structures (Cu K_α) [66] (d) Comparison of XRD patterns between different low dimensional perovskite in n=2 and n=3 respectively (Cu K_α) [67]

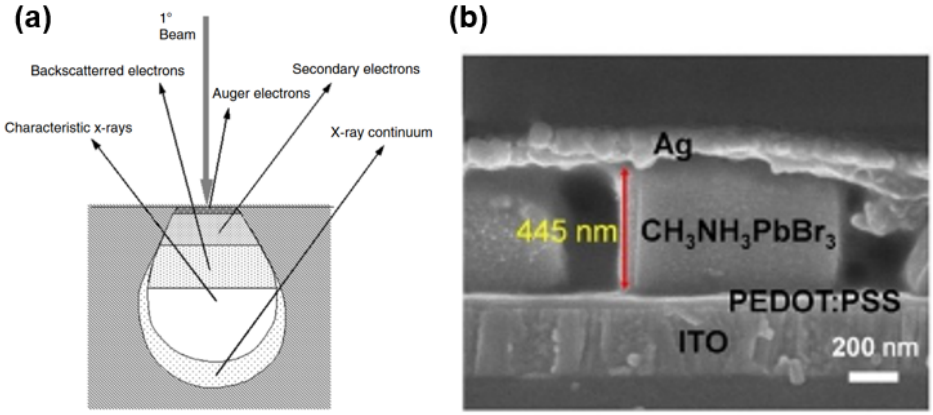

Figure 2-6: (a)Interaction between electrons and matter [71] (b)Uneven distribution film distribution of PeLEDs [38]

law under constructive interference. The intensity of the diffraction peaks is positively correlated with the volume fraction of the corresponding crystal structure in the material [68].

XRD is now widely employed in perovskite research. Typical bulk perovskites used in optoelectronic devices (e.g., photovoltaics, LEDs, and photonic sensors) generally adopt the α-phase structure, exhibiting distinct (100) and (200) diffraction peaks near 15° and 30° [69, 66, 67, 70]. Compositional variations weakly alter the lattice parameters of multilayered halide perovskites (MHPs), causing minor XRD peak shifts. However, since only α-phase MHPs are functionally viable, these two characteristic XRD peaks persist (Fig. 2-5(b-d)).

Characterizing quasi-2D perovskites—particularly those in PeLEDs—remains challenging due to their reduced thickness. Studies indicate that quasi-2D perovskites typically exhibit XRD peaks primarily below 10°, while maintaining high-n phase peaks at 15° and 30° (Fig. 2-5(d)) [65].

2.3.2 Morphology Characterization

In scanning electron microscopy (SEM), image formation relies on signals generated by the interactions between the electron beam and the sample, which can be categorized into elastic and inelastic interactions. Elastic scattering occurs when incident electrons are deflected by the nuclei or high-energy outer-shell electrons of the sample atoms, with negligible energy loss during the collisions. The scattering direction of the electrons changes significantly, often at wide angles. Incident electrons scattered elastically at angles greater than 90 ° are referred to as backscattered electrons (BSE), which generate signals useful for imaging the sample. Inelastic scattering, on the other hand, occurs when incident electrons interact with the sample's electrons and atoms, transferring a significant amount of energy. The energy loss depends on whether the sample electrons are excited individually or collectively and on the binding energy of the electrons within the atoms. The excitation of sample electrons during atom ionization produces secondary electrons (SE), typically defined as electrons with energy less than 50 eV, which are commonly used for imaging or analysis of the sample. In addition to the signals used for imaging, electron beam interactions with the sample generate other signals, such as characteristic X-rays, Auger electrons, and cathodoluminescence [71]. For MHPs, SEM frequently utilizes SE imaging to directly visualize thin-film layers and analyze defects in the films. For example, SEM can reveal issues such as uneven coating distribution (Fig. 2-6(b))[38] and pinhole defects[72].

2.3.3 Photoluminescence Spectroscopy

Photoluminescence Spectroscopy (PL) refers to the process where a semiconductor, upon being excited by external light, generates non-equilibrium carriers that undergo recombination.

The recombination of carriers includes both radiative and non-radiative processes, which compete with each other. The overall recombination process can be expressed as[73]:

$$I = -\frac{1}{\tau_1}A_1 - \frac{1}{\tau_2}A_2 - \frac{1}{\tau_3}A_3 \tag{2-8}$$

Here, τ_1, τ_2, τ_3 represent the lifetimes of monomolecular (defect-related MR), bimolecular (radiative BR), and Auger (three-body) recombination processes, respectively, with A_1, A_2, A_3 being their respective probabilities. At low carrier concentrations, carriers recombine through shallow-level defects, while higher concentrations lead to radiative recombination. Excessive illumination intensity results in Auger recombination [73].

MR in semiconductors involves nonequilibrium carriers recombining through centers formed by impurities or intrinsic defects which can be broadly categorized into two types: bulk defects, which are commonly found in the EML, and interface defects, which occur at the interface [74].

BR is widely utilized in the characterization of perovskite optoelectronic thin films. PL-based analysis provides a range of insights into the carrier dynamics of perovskite materials. The two commonly used PL techniques are Time-Resolved PL (TRPL) and Steady-State PL.

Time-Resolved Photoluminescence: Time-Resolved Photoluminescence (TRPL) is a technique for measuring transient PL, as illustrated in Fig. 2-7(a). Using the Time-Correlated Single Photon Counting (TCSPC) method, a timing device connects a pulsed light source with a single-photon-sensitive detector, such as an avalanche photodiode or a photomultiplier tube. It records the number of photons detected during each pulse period. The pulse period must be carefully chosen to allow the excited sample sufficient time to return to its relaxed (dark) state. If not, charge carriers may accumulate in the sample, leading to unpredictable additional recombination losses. This process is repeated millions of times to obtain the average carrier lifetime of the sample. Since a higher defect state density reduces radiative recombination probability and facilitates carrier recombination, PeLEDs with longer carrier lifetimes are typically expected [73, 75, 76]. A typical TRPL data plot is shown in Fig. 2-7(b) [77]. By fitting the curves in the plot using Eq. 2-8, the contributions of MR, BR, and Auger recombination can be quantified. Analyzing these contributions helps researchers understand the relationship between their fabrication protocols and the defect state density of the thin films [77].

Steady-State Photoluminescence: The typical setup for steady-state PL is largely consistent with that of TRPL, but it typically uses a charge-coupled device as the detector and solid-state laser diodes as the excitation source. A typical PL spectrum is shown in Fig.2-7(c), where the peak wavelength of the PL spectrum indicates the band-edge emission of the semiconductor material and aligns with the peak wavelength of EL [76].

Photoluminescence Quantum Yield: Photoluminescence Quantum Yield (PLQY) is another critical parameter, representing the ratio of the number of photons emitted to the number of photons absorbed by the sample. It provides insight into the radiative recombination efficiency of the material. Measuring PLQY requires a PL setup calibrated for absolute photon numbers. The most common implementation involves placing the sample in an integrating sphere and exciting it with a Ultraviolate light coupled to the sphere. The detailed setting are shown in Sec. 3.2 [78, 76].

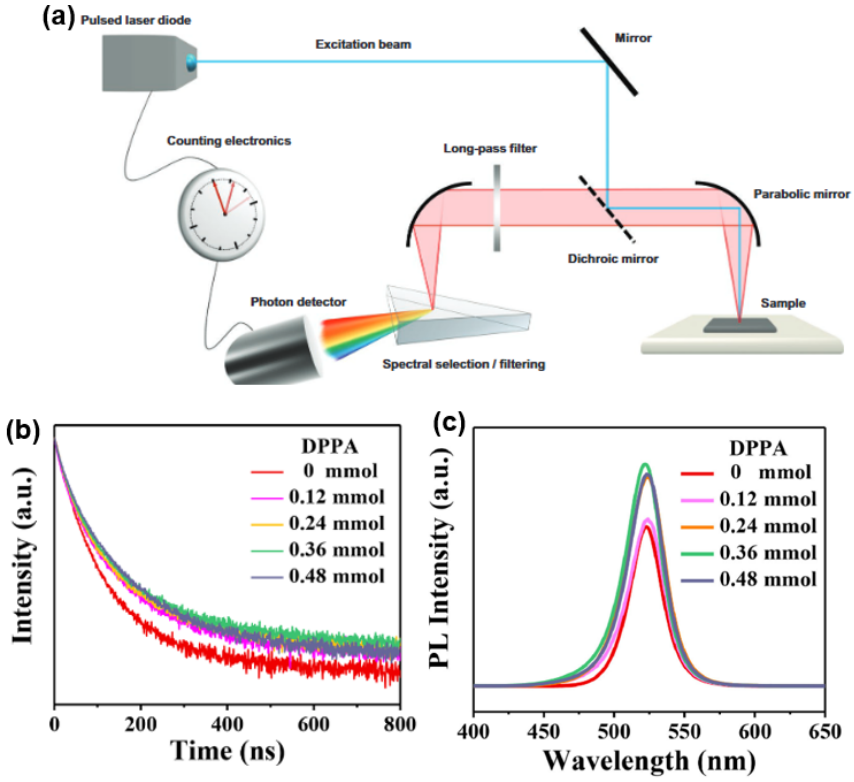

Figure 2-7: (a) Setup of typical TRPL [75](b) Typical measuring result of TRPL [77] (c) Typical PL spectrum (DPPA is a kind of additive) [77]

2.4 LED Test Instrument

For LEDs, the most critical performance metrics are electrical and optical characteristics, characterized by three interrelated parameters: voltage, current, and luminance. Electrical properties are typically straightforward to obtain through voltage sweeps across the PeLED, which yield corresponding current measurements. In mainstream academic journals, PeLED electrical characterization commonly presents current density-voltage (J-V) curves (Fig.2-8(a)), derived by normalizing current to the device's active area. Some publications supplement these with current-voltage (I-V) curves (Fig.2-8(b)).

Optical data processing presents greater complexity. Measurements of critical PeLED metrics—EQE and PLQY—require an integrating sphere to capture omnidirectional emitted photons, coupled with spectrometer detection (Fig.2-9). However, the non-ideal reflectance of the sphere's internal coating introduces photon losses.

To compensate, system calibration using standardized light sources establishes the absolute spectral responsivity ($R_{\text{abs}}(\lambda)$) of the integrated sphere-spectrometer assembly. The true spectral photon flux (Φ_λ) is then derived as:

$$\Phi_\lambda = \frac{I_{\text{det}}(\lambda)}{R_{\text{abs}}(\lambda)} \tag{2-9}$$

where $I_{\text{det}}(\lambda)$ denotes the spectrometer-recorded intensity, thereby accounting for wavelength-dependent system responsivity.

Spectrometers typically report light intensity in either digital counts or optical power units. For count-based measurements, the signal can be directly converted to photon flux, enabling EQE calculation as the ratio of emitted photons to injected electrons. For power-based measurements, the intensity

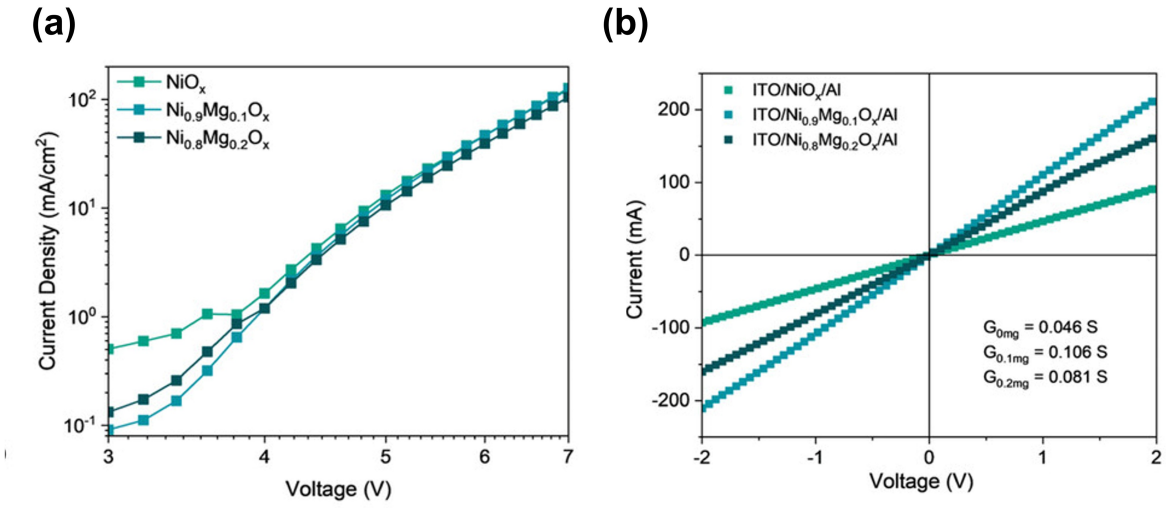

Figure 2-8: J-V (a) and I-V (b) curves displayed in PeLEDs [37]

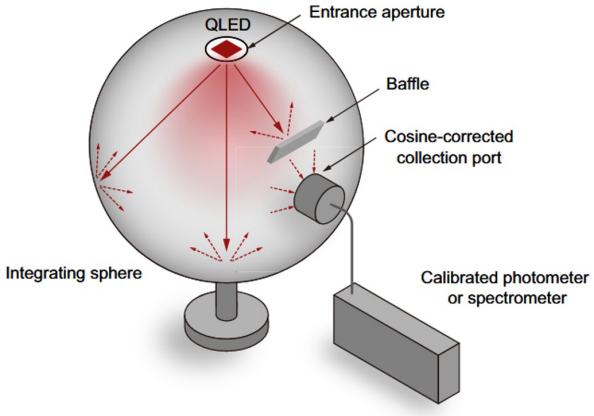

Figure 2-9: Common integrating sphere set-up for EQE testing of LEDs. Baffle and cosine-corrected collector port can reduce measurement errors caused by different incident angles [79].

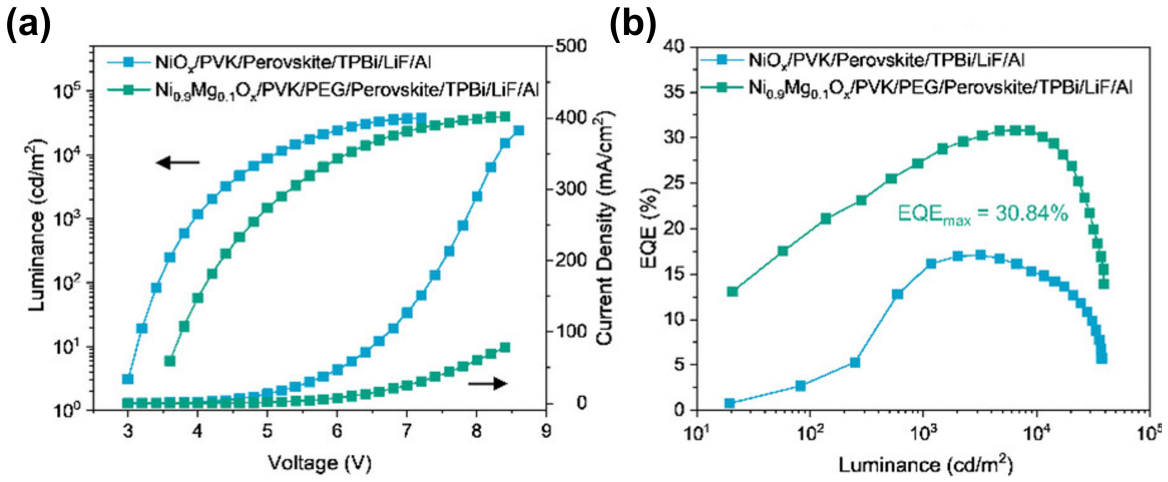

Figure 2-10: J-V-L (a) and EQE-L (b) curves displayed in PeLEDs [37]

must first be converted to photon flux using the photon energy ($E_{\text{photon}} = hc/\lambda$) before deriving EQE (Eq.2-10) [79].

$$\text{EQE} = \frac{\Phi_{\text{em}}}{N_{\text{inj}}} (\text{power-based}) \tag{2-10}$$

where N_{inj} = injected electrons.

Beyond EQE, luminance (cd/m^2) constitutes another critical PeLED metric. As a photometric quantity defined by the human photopic response, it cannot be directly calculated from radiative photon flux. Conversion requires: (1) transforming photon flux to spectral radiant power, (2) applying the photopic luminosity function $V(\lambda)$ to compute luminous flux (lumens), and (3) normalizing by the emitting area to obtain luminance(Eq.2-11) [79, 80].

$$L_v = \frac{\int P(\lambda) V(\lambda) d\lambda}{A \cdot K_m} \quad \text{with} \quad K_m = 683 \text{ lm/W} \tag{2-11}$$

where L_v = luminance (cd/m^2), A = emitting area (m^2), $V(\lambda)$ = CIE photopic luminosity function.

Combining the acquired I-V relationships with corresponding EQE and luminance measurements enables generation of essential PeLED performance plots, including Current Density-Voltage-Luminance (J-V-L) characteristics and EQE versus Luminance (EQE-L) profiles etc (Fig.2-10).

In this thesis, the absence of dedicated LED characterization instrument and limited access to integrating spheres within the PVMD group precluded comprehensive optoelectronic analysis using systems such as that depicted in Fig.2-11. Consequently, device evaluation employed a pragmatic approach: current injection via the group's solar simulator source meter coupled with visual inspection of electroluminescence.

At the end of this Master's project, we successfully secured an integrating sphere from the Electronic Instrumentation (EI) group at TU Delft and assembled the LED test setup shown in Fig.2-11. This system enabled spectral characterization of commercial green LEDs. However, due to time constraints, no automated control protocol was implemented. Measurements currently require manual operation:

- Voltage application via standalone power supply
- Spectral acquisition through dedicated spectrometer software
- Manual data saving for each measurement point

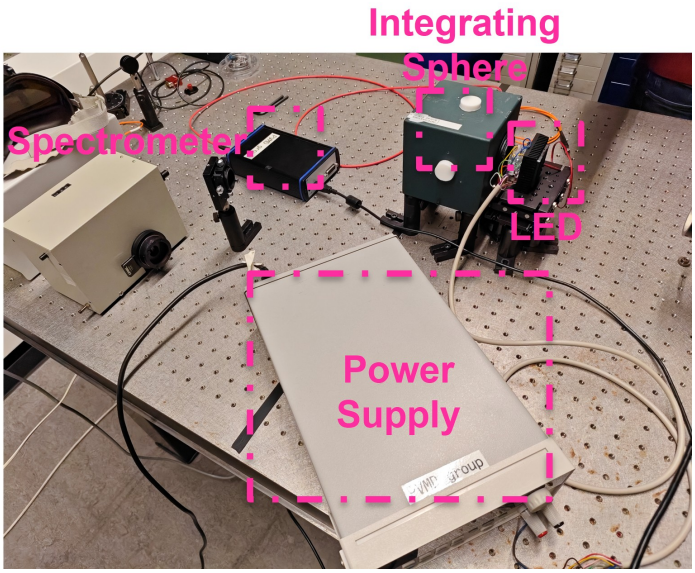

Figure 2-11: Home-made EQE test system, consisted by a power supply, integrating sphere and spectrometer

Future development will focus on implementing automated voltage scanning with synchronous spectral capture, enabling comprehensive optoelectronic characterization of PeLEDs across operational bias conditions.

3 Enhancement of Characterization Reliability: Protocol Optimization for TRPL and PLQY in Perovskite Films

The development of PeLEDs represents a new research direction within the PVMD group. This necessitates implementing novel protocols to ensure reliable fabrication and characterization. This chapter details newly introduced protocols and associated challenges encountered during PeLED development.

3.1 Carrier Lifetime Decay Modeling of PMMA-Protected Perovskites: Dynamic Spin Coating for Delayed Degradation Kinetics

As detailed in Sec.2.3.3, TRPL spectroscopy probes carrier recombination dynamics at semiconductor, serving as a sensitive indicator of defect density. Higher defect concentrations accelerate carrier depletion, manifested as rapid photoluminescence decay and reduced average carrier lifetime (τ_{avg}). Conversely, lower defect densities yield slower PL decay and longer τ_{avg}, where τ_{avg} represents the weighted mean of monomolecular and bimolecular recombination lifetimes.

This technique theoretically enables assessment of CTL/EML interface quality. At well-coupled interfaces, photogenerated free carriers efficiently diffuse across the EML/CTL junction via built-in electric fields, accelerating carrier depletion in the CTL. Consequently, CTL/EML heterostructures should exhibit significantly shorter τ_{avg} than isolated EML films. Poor interfacial coupling suppresses this effect, while completely dysfunctional interfaces yield identical lifetimes for both configurations.

To evaluate TPBi/EML interfacial characteristics, we measured τ_{avg} for both pristine perovskite films and perovskite/TPBi heterostructures (sample structures in Fig.3-1). Contrary to theoretical expectations, the perovskite/TPBi sample demonstrated longer τ_{avg} than the CTL-free reference.

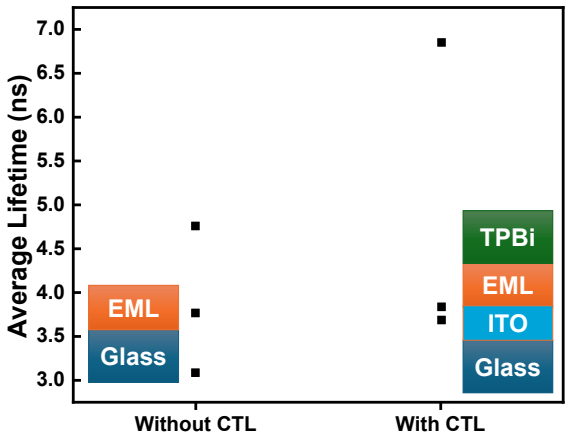

Figure 3-1: Average lifetime of perovsite with CTL and without CTL

This anomaly is attributed to the measurement protocol: all samples were stored in vials within sealed bags prior to testing. During sequential measurements, vials insufficiently protect samples from the progressive air exposure. Typically, perovskite reacts with water in the air as follows[81].

$FAPbX_3 + H_2O \longrightarrow FAX(aq) + PbI_2(s)$

Crucially, samples without TPBi exhibited significant lifetime reduction with increasing air exposure time (Fig.3-1(c)). In contrast, the TPBi layer acted as a protective barrier against ambient moisture/oxygen, preserving the EML integrity. These findings indicate that ambient exposure duration—rather than intrinsic material properties—dominated the measured lifetimes. Implementation of improved encapsulation methods is urgently required for reliable characterization.

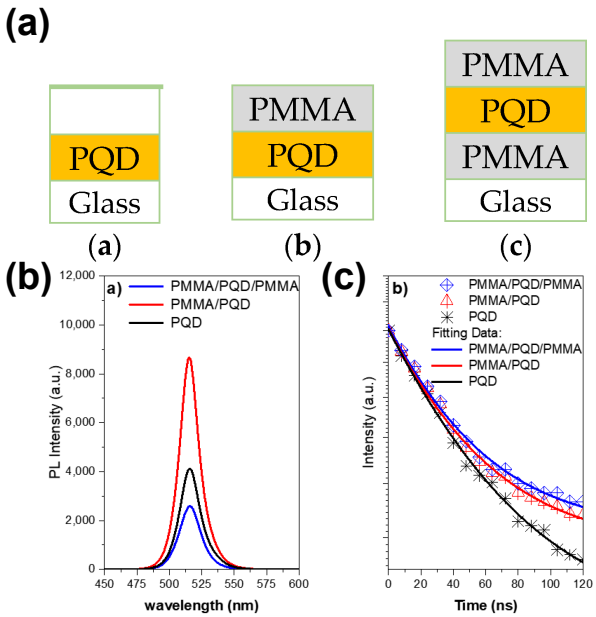

Figure 3-2: PMMA Reported to enhance the environmental robustness (a) Device structure in report (b) PL intensity and carriers lifetime achieved by PMMA encapsulation [82]

3.1.1 PMMA by Static Spin Coating

PMMA is a widely used encapsulation polymer [82, 81]. Qaid et al. demonstrated that coating $CsPbBr_3$ quantum dot layers with PMMA significantly enhances both PL intensity and carrier lifetime in TRPL measurements (Fig.3-2)[82]. These results confirm that a single PMMA overlayer effectively boosts quantum dot performance by increasing PL intensity and extending carrier lifetimes.

Therefore, this work employs PMMA encapsulation layer to protect EML from degradation. To rigorously evaluate the PMMA layer's barrier efficacy against ambient degradation, an experimental protocol was created and implemented, it is illustrated in Fig.3-3 was implemented:

1. Start timing: unsealing fo the encapsulation bag
2. All samples undergo sequential carrier lifetime measurements. Typically, The initial sample measurement requires approximately four minutes to optimize the detector's operational intensity range based on the sample's photoluminescence characteristics, while subsequent measurements require approximately 2.5 minutes per sample.
3. After completing the measurements of all the samples, measurements are repeated in identical order.
4. Three complete measurement cycles are performed.

This methodology enables statistical averaging of lifetime decay rates across samples exposed to comparable time intervals, thereby quantifying PMMA's protective performance under controlled degradation conditions.

As shown in Fig.3-4, experimental results demonstrate poor reproducibility across all PMMA-encapsulated samples except the pristine group. Significant lifetime variations were observed among nominally identical samples under equivalent processing conditions. This inconsistency stems from two interrelated factors: (i) Suboptimal wettability of EA-based PMMA solutions on perovskite surfaces, which further deteriorates with increasing PMMA concentration due to enhanced hydrophobicity.

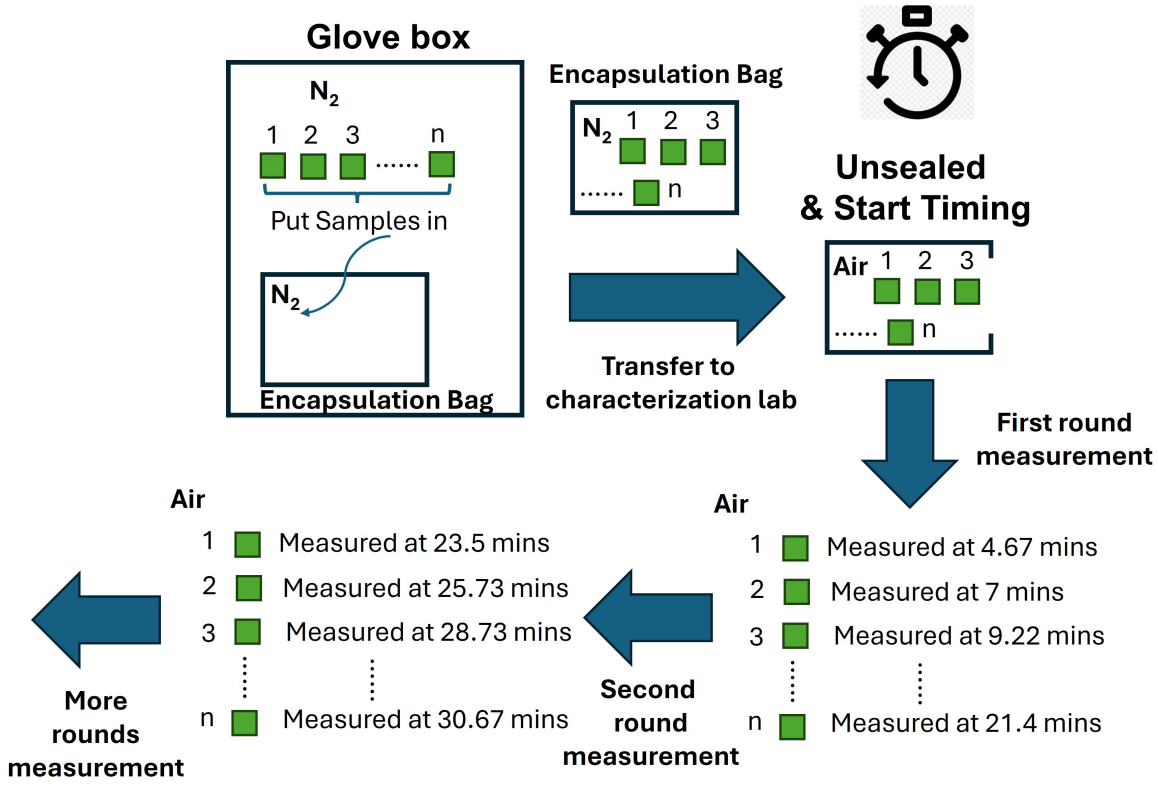

Figure 3-3: The order in which samples are measured under timing conditions. The test time of each sample is from Fig.3-4

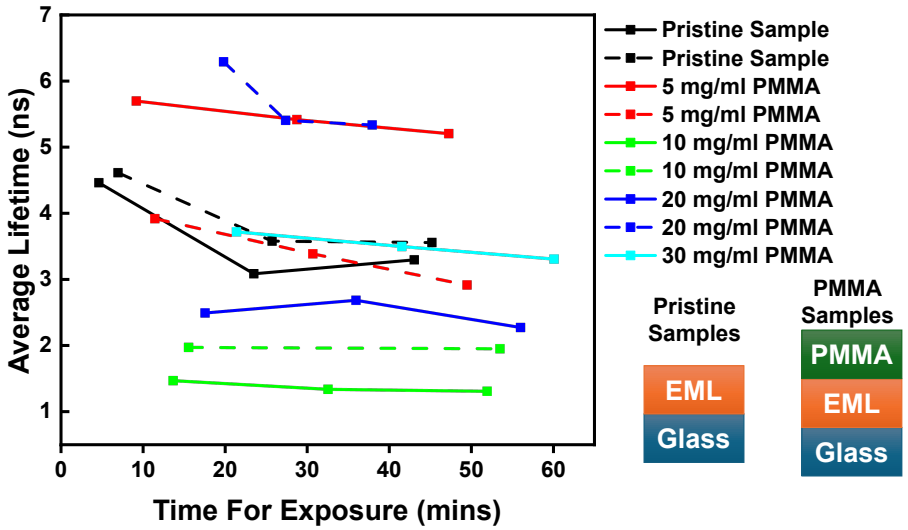

Figure 3-4: Evolution of average lifetime of samples encapsulated with different PMMA layer concentrations. The exposure time refers to exposure in ambient air after unsealed encapsulation bag.

(ii) Concentration-dependent hydrophobicity necessitates varying solution dispensing volumes during spin coating, while inherently low wettability compromises PMMA film uniformity. These combined effects create sample-specific encapsulation heterogeneity, ultimately preventing statistically consistent results.

Despite poor sample reproducibility, the observation that champion PMMA samples were processed from 20 mg/ml PMMA solutions suggests potential efficacy at this concentration. In addition, although the 5 mg/mL PMMA samples exhibited favorable properties, given the reproducibility challenges observed at both concentrations, subsequent investigations will focus exclusively on the 20 mg/mL PMMA solution (higher concentration) system as a precautionary measure.

3.1.2 PMMA by Dynamic Spin Coating

Based on the inclusive results shown in Fig.3-4, a different way to improve the PMMA coverage is considered. Dynamic spin coating enhances film coverage for hydrophobic precursors by employing a two-stage process [83]:

1. Low-speed stage: The substrate rotates at a constant low speed while the precursor solution is dispensed, enabling uniform dispersion.

2. High-speed stage: Rotation accelerates to achieve thin-film formation.

This sequential approach may overcomes poor wettability to produce homogeneous films.
To investigate dynamic spin coating for PMMA encapsulation, three sample groups were prepared:

1. Group 1: Static spin coating (reference);

2. Group 2: Standard dynamic spin coating (dispensing at low speed only);

3. Group 3: Modified dynamic spin coating (dispensing in both the low speed stage and high speed stage).

All samples underwent identical degradation characterization following the protocol in Fig. 3-3.

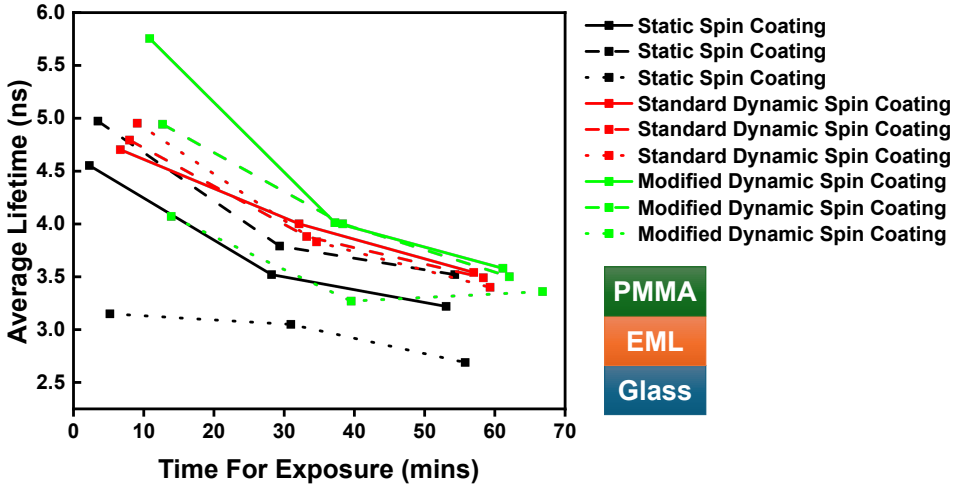

Figure 3-5: Evolution of average lifetime of samples encapsulated with PMMA layer fabricated by different spin coating method (static spin coating, standard dynamic spin coating and mdified dynamic spin coating). The exposure time refers to exposure in ambient air after unsealed encapsulation bag.

Measurement result are shown in Fig.3-5, demonstrate that standard dynamic spin-coated samples exhibit longer lifetimes and superior reproducibility compared to static and modified dynamic approaches. While modified dynamic spin coating produced two samples with extended lifetimes, its reproducibility remained poor. This limitation likely stems from compromised film-forming capability and coverage during high-speed rotation. Although dual-layer PMMA deposition potentially enhances environmental robustness, it sacrifices process repeatability. Consequently, standard dynamic spin coating is determined to produce PMMA films with optimal thickness uniformity and coverage.

However, comparing lifetimes in Fig.3-5 (PMMA-protected perovskite) with Fig.3-4 (unprotected perovskite) reveals a paradox: Unprotected samples showed initial average lifetimes of 4-5 ns, decreasing to 3-4 ns after 40 minutes of air exposure—values comparable to well-PMMA-encapsulated EML. These measurements are hard to demonstrate significant protective benefits of PMMA against ambient degradation.

3.1.3 The Function of PMMA and the General Decay in Emissive Layer

while Sec.3.1.2 reports minimal differences in initial and long-term carrier lifetimes between PMMA encapsulated and pristine perovskite samples exposed to air, a comparative analysis reveals a notable divergence during intermediate exposure periods. The unencapsulated pristine sample (Fig.3-4) exhibits carrier lifetimes of 3-4 ns after 20 min air exposure, whereas the PMMA-encapsulated sample fabricated via standard dynamic spin coating (Fig.3-5) maintains lifetimes of 4-5 ns under identical exposure conditions.

Consequently, this thesis proposes a lifetime decay model for air-exposed with and without the PMMA encapsulation film, as illustrated in Fig.3-6. Based on the experimental phenomena of previous samples (Fig.3-5 and Fig.3-4), although the specific chemical process of perovskite erosion by air is not yet known, we speculate that when the EML is exposed to ambient air, perovskite rapidly degrades, transitioning to a metastable state within approximately 10 minutes. This metastable state maintains its relative stability for a long period of time under air exposure. Crucially, PMMA encapsulation delays the perovskite's degradation to this metastable state.

To validate the proposed lifetime decay model, this thesis developed an optimized test scheme (Fig. 3-7) involving six perovskite samples consisting of three PMMA-encapsulated and three pristine samples. Fabricated samples were sealed into two nitrogen-sealed bags (PMMA and non-PMMA

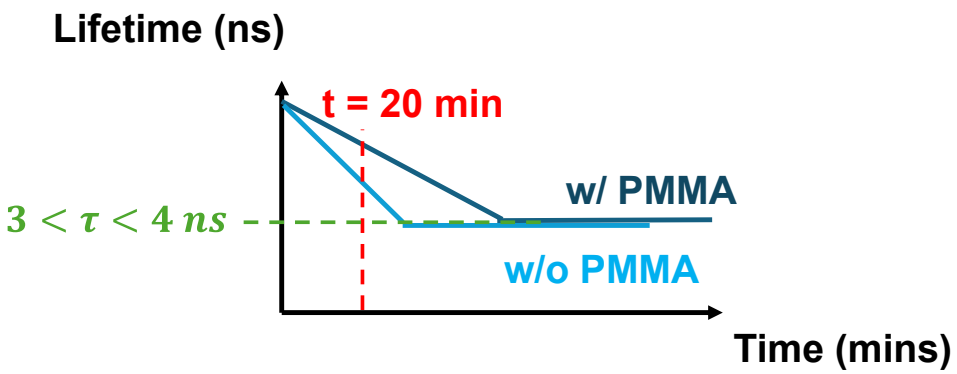

Figure 3-6: Lifetime decay model of perovskite w/ and w/o encapsulation layer in air.

groups). Testing commenced by opening one bag and performing sequential time-resolved TRPL measurements on all three samples. After recording results with precise timestamps, the sequence was repeated from the first sample, completing nine full cycles to track lifetime evolution over 40 minutes. The second bag was subsequently opened and subjected to identical testing protocol.

The experimental results presented in Fig.3-8 reveal three data processing challenges:

First, significant lifetime fluctuations were observed during individual sample measurements. Since perovskite lifetime should monotonically decrease under air exposure without special treatment, observed lifetime rebounds are attributed to measurement artifacts. These likely stem from the TRPL sample holder design—spring-loaded clips provide vertical constraint but lack horizontal fixed position. Consequently, samples repositioning between measurements may displace the mode-locked laser spot (about 0.5 μm diameter) to different sample regions, introducing positional variability.

Second, sequential measurement of three samples prevents simultaneous lifetime acquisition, precluding direct temporal averaging. To resolve this, this thesis implemented an interpolation algorithm: (1) Generate a master time grid, (2) For each grid point, identify bounding measurement times for each sample, (3) Compute expected lifetime via linear interpolation between adjacent measurements, (4) Average interpolated lifetimes across all three samples at each grid point (the solid line in Fig.3-8).

Third, optical system calibration required about 4 minutes of air exposure before pristine lifetime measurement. This initialization delay likely prevented capture of the initial rapid degradation phase, particularly critical for unencapsulated samples where significant lifetime loss occurs within the first 2-3 minutes of air exposure.

As shown in Fig.3-8, PMMA-encapsulated samples exhibit characteristic lifetime behaviors across different exposure durations:

1. Short-term (10 min): Lifetimes range between 4.5-5 ns
2. Mid-term (20-40 min): Stabilize around 4 ns

Both regimes align quantitatively with standard dynamic spin-coated samples in Fig.3-5.

For extended exposures (>40 min), the lifetime decay rate progressively decreases (Fig.3-5). While measurement variability obscures precise determination beyond 10 min, the observed trend suggests lifetimes likely converge to 3.5-4 ns—consistent with standard samples in Fig.3-5. Given the exceptional reproducibility demonstrated by standard dynamic spin-coated references, these measurements reliably capture the air-exposure degradation dynamics.

In summary, in this thesis, we successfully observe the phase transition from unstable to metastable states in PMMA-encapsulated perovskites under ambient conditions. The measured lifetime evolution qualitatively matches the model prediction in Fig.3-6.

For unencapsulated EML samples, lifetime variations exhibit minimal temporal dependence. The 10-min lifetime measurements here are lower than those in Fig.3-4. Rather than experimental inac-

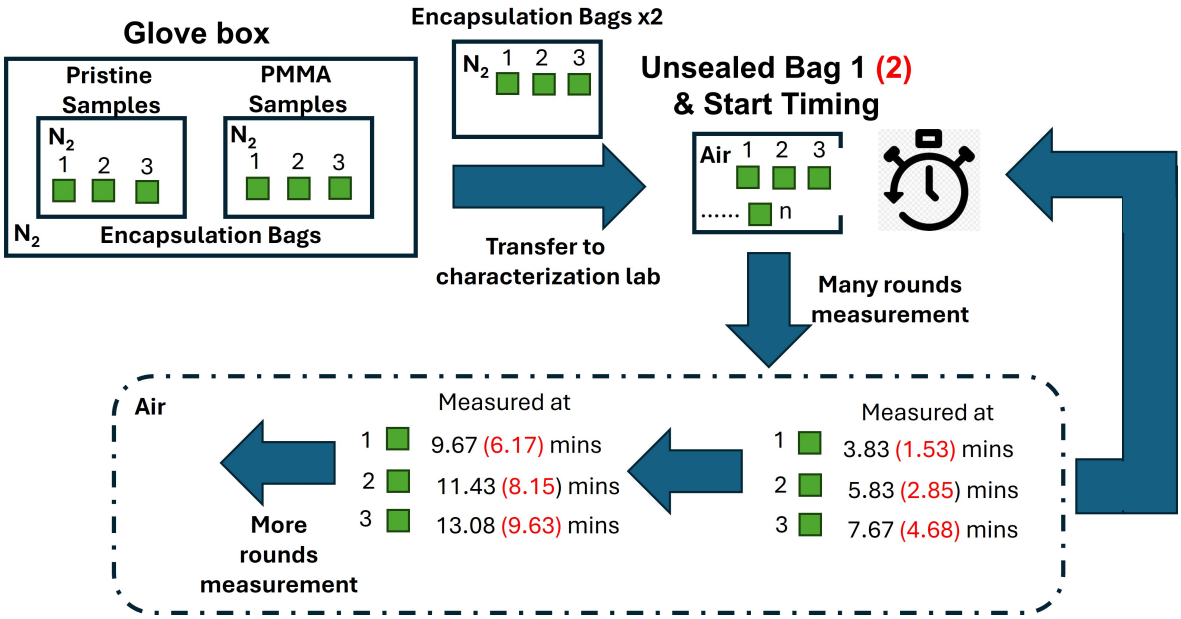

Figure 3-7: Test scheme to confirming the decay model hypothesis, The test time of each sample is from Fig.3-8

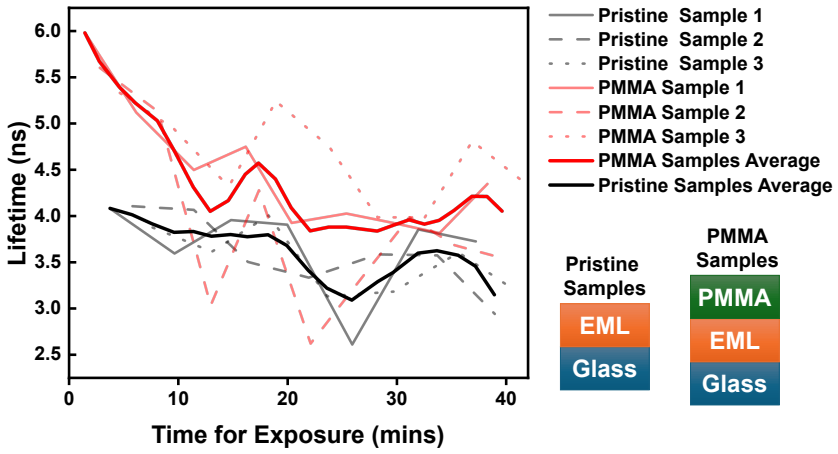

Figure 3-8: The lifetime of six samples of two types changes with the air exposure time. The test sequence is shown in the Fig.3-7

curacy, this discrepancy likely originates from linear interpolation artifacts during data processing in Fig.3-4.

Considering the decay model hypothesis (Fig.3-6), rapid initial degradation kinetics explain the observed divergence: Measurement timing differences between pristine samples in Fig.3-4 (earlier measurement) and this work (later measurement) yield substantially different lifetimes due to the steep early-stage decay slope.

Conversely, both datasets demonstrate near-constant lifetimes during extended exposure (>30 min), converging toward ∼3.5 ns. This long-term stabilization aligns with the metastable state predicted in Fig.3-6.

Collectively, these experimental results provide comprehensive validation of two critical aspects:

1. The degradation hypothesis proposed in Fig.3-6 accurately describes perovskite lifetime evolution under ambient exposure,

2. PMMA encapsulation effectively delays the degradation kinetics, delay the metastable state compared to pristine samples.

Although this thesis demonstrates PMMA's efficacy in retarding perovskite degradation, several limitations warrant acknowledgment:

Firstly, the measured lifetimes (typically several nanoseconds) in this thesis fall significantly below state-of-the-art perovskite PeLEDs exhibiting tens to hundreds of nanoseconds in nitrogen environments [37, 36]. The origin of this discrepancy remains unresolved: whether attributable to intrinsic material quality differences or rapid air-exposure degradation occurring within seconds remains uncertain.

Secondly, time constraints inherent to a Master's program precluded comprehensive investigation of quasi-2D perovskite degradation kinetics under ambient conditions. While existing studies elucidate bulk perovskite degradation mechanisms [84], they lack molecular-level dynamics analysis and seldom address quasi-2D systems specifically.

Methodologically, conventional techniques like XRD and SEM-EDS employed in alloyed perovskite degradation studies [85] is unsuitable for our rapidly evolving systems. The requisite measurement timescales (XRD scanning duration, SEM vacuum chamber transfer) exceed the unstable-to-metastable transition period. Instead, *in situ* Raman spectroscopy under controlled low-humidity conditions presents a promising alternative, enabling:

1. Deciphering bond-specific degradation signatures through vibrational mode shifts

2. Continuous monitoring of chemical bond formation/dissolution kinetics

This approach could ultimately establish a molecular degradation model for air-exposed quasi-2D perovskites.

3.2 PLQY Uncertainty Quantification: Protocol Redesign for Valid Perovskite Emission Efficiency Characterization

PLQY is one of the most important parameters characterizing EML quality, as it quantitatively reflects the defect level within the EML. PLQY is defined as the ratio of emitted to absorbed photons (Eq. 3-1). The FLS 980 used in this thesis requires replacing the PL sample holder (used for PL test) by an integrating sphere component (used for PLQY test). Measurements were taken for both the sample (perovskite/quartz) and blank reference (Quartz) using the integrating sphere, obtaining the relationship between spectral intensity and wavelength for both. The intensity difference in the excitation peak was integrated to obtain $n_{absorbed}$, while the intensity in the emission peak was integrated to obtain $n_{emitted}$. PLQY was calculated as the ratio of these two values.

It should be emphasized that rigorous determination of PLQY requires absolute quantification of absorbed and emitted photons. However, the integrating sphere cannot collect every emitted photon,

and the photomultiplier tube (PMT) in the FLS 980 system lacks single-photon counting capability. Consequently, the derived values of n_{absorbed} and n_{emitted} represent calibrated ratios of PMT signals to the instrument's spectral sensitivity. This work considers the calibrated light intensity measurements from the FLS 980 PLQY setup to accurately represent the photon flux.

$$\eta_{PLQY} = \frac{n_{emitted}}{n_{absorbed}} \tag{3-1}$$

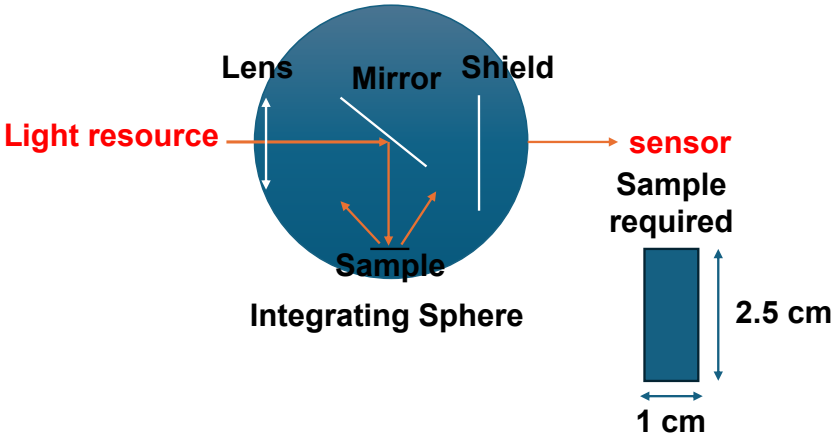

Figure 3-9: PLQY measurement setup and samples size required by the FLS 980

Following the instrument requirements, we firstly prepared a series of samples to investigate the PLQY of samples obtained by using different additives and antisolvents in Sec.4. This thesis aims for relatively consistent measurement results within each sample group during testing.

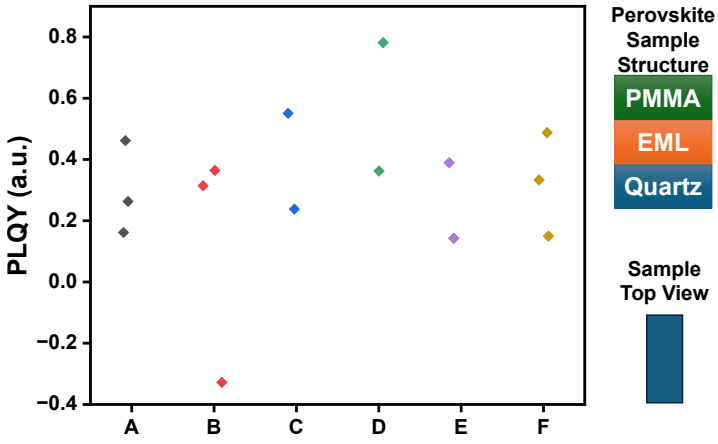

Figure 3-10: PLQY tested by default configuration of FLS 980. A, B, C, D, E, and F are different sample groups. The samples in each group were prepared under the same conditions.

The experimental results are presented in Fig. 3-10. Different samples within the same group exhibited substantial variations in PLQY. Notably, Group B even yielded negative PLQY values, indicating either lower light absorption by the perovskite/quartz sample compared to the quartz substrate, or higher emission from the perovskite/quartz sample than from quartz. Clearly, these measurements indicate that the results lack reliability. To address the origin of the large spreading of results, we further analyzed the PLQY spectra.

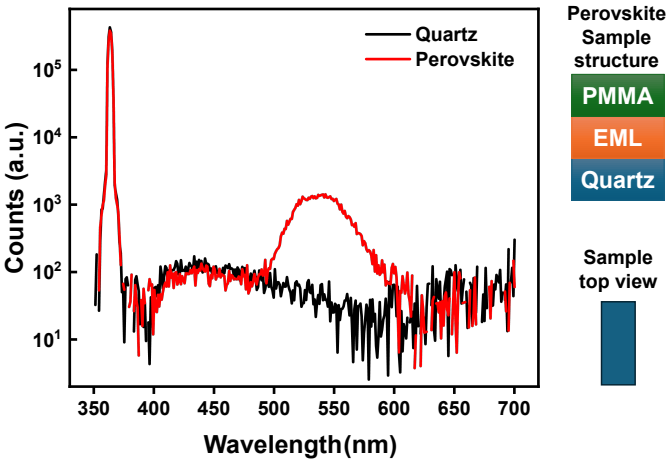

Figure 3-11: PLQY Spectra obtained using the default setup and quartz substrate for FLS 980

PLQY spectra of quartz and perovskite coated with PMMA are shown in Fig.3-11. When using a logarithmic scale axis, we find there are no significant differences between the two curves at the absorption peak, while more pronounced intensity differences appear under the excitation peak. Although in terms of absolute interpolation, the difference at the excitation peak still exceeds that at the absorption peak, the error source is more likely attributable to the emission peak. However, considering the typical uncertainty of several percent (frequently exceeding 2%) for instrument integrating spheres, the situation differs.

For the situation in Fig.3-11, the excitation peak intensity reaches approximately 5×10^5 counts. Given the difficulty in obtaining specifications for the uncertainty of the FLS 980's specific integrating sphere, this thesis conservatively estimate it at 2%, yielding a potential error magnitude of 10^4. This order of magnitude aligns with the observed difference in excitation peaks between the two samples. Consequently, the denominator in Eq.3-1 would contain inacceptably large errors. This implies that the observed discrepancies originate from measurement equipment (integrating sphere and sensor) even though these equipments demonstrate adequate performance specifications.

To further identify error sources and exclude instrument aging as a potential cause, this thesis performed two PLQY spectral measurements on the same quartz sample under 365 nm excitation. Results are shown in Fig.3-12(a)(b).

First, in absolute terms, the maximum difference between the two quartz tests occurs at 365 nm, with smaller differences at other wavelengths. This aligns with the excitation peak position in Fig.3-11. It is evident that this significant error originates from the high excitation peak.

Second, regarding the difference ratio, larger ratios occur outside the excitation peak range where spectral intensity depends entirely on environmental noise. Thus, spectral ratios beyond the excitation peak range are entirely random and uninformative.

From Fig.3-12(b), at the wavelength of maximum difference ($\lambda = 365$ nm), the ratio is approximately -0.1. Considering this uncertainty is derived from the subtraction of two PLQY measurements, the integrating sphere's uncertainty in this measurement is about 5%, consistent with experimental expectations.

Therefore, it is concluded that while experimental errors indeed stem from integrating sphere uncertainty, improving measurement accuracy by replacing with higher-performance integrating spheres and sensors would be inefficient in this experiment.

Beyond component replacement, the FLS 980 offers additional functions to improve measurement conditions. First, adjusting slit widths can modulate incident and emitted light intensity. However, this only proportionally scales both the excitation peak and sample absorption, failing to effectively reduce

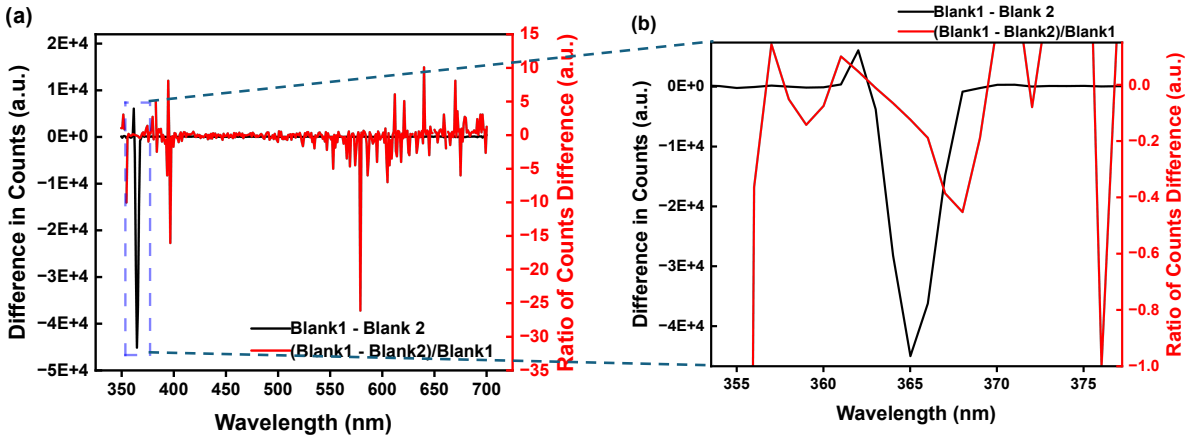

Figure 3-12: Repeat the measurement twice on the same quartz substrate to measure the error level of FLS 980. The first measurement result is blank1, and the second measurement result is blank2 (a) Full spectra of $blank1 - blank2$ and $(blank1 - blank2)/blank1$ (b) Local spectra of $blank1 - blank2$ and $(blank1 - blank2)/blank1$

uncertainty in the denominator of Eq. 3-1. Second, increasing PL integration time with repeated measurements for averaging is inadvisable due to rapid perovskite degradation in air observed in Sec.3.1.

Therefore, this thesis proposes modifying the default protocol. Typically, in a well-calibrated PLQY instrument(spatially modulated point light source), the light incident on the sample forms an Airy disk where light intensity follows Airy relation relative to the disk center [86]. Consequently, using larger-area samples as depicted in Fig.3-13 could enhance light absorption while maintaining excitation light intensity. This approach would increase the expected value in the denominator of Eq.3-1 without altering its uncertainty, thereby reducing the uncertainty in η_{PLQY}.

Measurement results using the new protocol are presented in Fig.3-14. First, some data gaps ($360 < \lambda < 410$) are observed beyond the absorption and emission peaks. The data gaps are formed since these data gap regions primarily originate from environmental noise, and some noise components fall below zero, these minus signal are precluded by the logarithmic scale axis introduced in Fig.3-14. However, these non-signal regions are excluded from analysis and thus do not affect results.

Second, comparison with Fig. 3-11 reveals approximately 10-fold enhancement in emission peak intensity alongside significant improvement in excitation peak difference. This demonstrates that larger substrates effectively increase the expected value in the denominator of Eq.3-1, reducing η_{PLQY} uncertainty and yielding more reliable measurements.

However, this reveals a new issue. Assuming proper instrument calibration producing an ideal Airy disk centered at the sample's diagonal focus, most light intensity should concentrate at the center with gradual radial decay.

As illustrated in Fig.3-15, for any Airy distribution and all spot profiles where light intensity non-strictly monotonically decreasing with radial distance, the maximum achievable light absorption enhancement from a 2.5-fold larger sample area is fundamentally limited to 2.5 times the original absorption.

Under such conditions, the observed 10-fold intensity difference between substrates differing only 2.5-fold in area (Fig.3-13) exceeds the theoretical maximum of 2.5× enhancement. This indicates likely optical misalignment in the FLS 980's integrating sphere setup.

One probable scenario, illustrated in Fig.3-16, involves:

1. For small quartz substrates: The Airy disk barely grazes the sample edge, resulting in minimal absorption

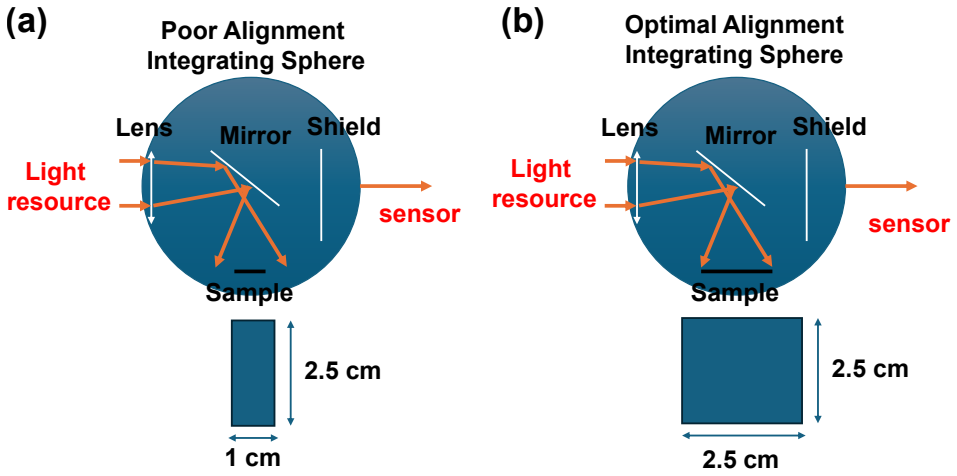

Figure 3-13: The optical path of PLQY when using the (a) default quartz substrate (b) ITO glass. Optimizing the PLQY measurement setup by increasing the sample area can improve the sample's absorption of light.

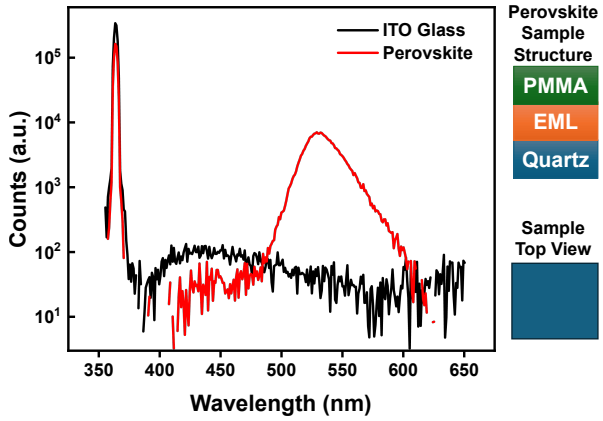

Figure 3-14: PLQY Spectra obtained using the optimal setup with ITO glass substrate

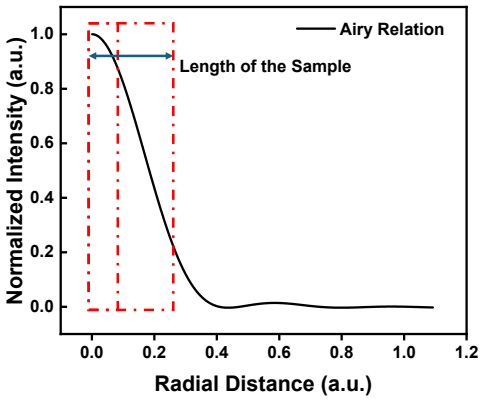

Figure 3-15: Light absorption enhancement limits for scaled sample areas. For any Airy distribution and beam profiles with non-strictly monotonically decreasing radial intensity, a 2.5-fold larger sample area yields exactly 2.5-fold stronger absorption *only* under uniform intensity distribution (constant intensity). All other configurations produce absorption enhancement factors less than 2.5.

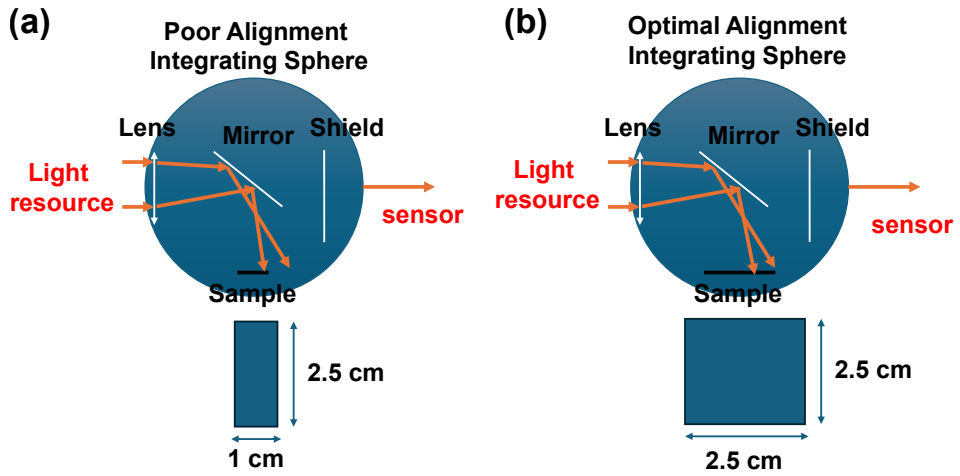

Figure 3-16: Possible serious misalignment in PLQY setup (a) When applying a small sample, a very small part of the light spot illuminate the sample (b) When applying a large sample, the main part of the light spot is on the sample.

2. For large ITO glass substrates: The primary lobe illuminates the sample periphery, enabling substantial absorption and emission

Under these conditions, while PLQY measurements remain feasible for perovskite/ITO/glass samples as shown in Fig.3-16(b), the spin-coated samples predominant in this study (Sec.2.2.1) typically exhibit poor uniformity. Consequently, the measured PLQY values likely underestimate actual performance. Due to restricted access permissions for adjusting integrating sphere mirrors/lenses and time constraints inherent to the Master's program, no further calibration of the FLS 980 was performed.

3.3 Summary

This chapter addresses challenges encountered during TRPL and PLQY measurements. For TRPL characterization of pristine samples, we identified that air exposure time—rather than intrinsic material properties—predominantly governs lifetime decay behavior. To obtain stable measurements, this thesis implemented PMMA encapsulation layers to isolate samples from ambient effects. Through optimized methodologies, this study achieved dual advancements:

1. Refinement of PMMA fabrication processes that effectively decelerate perovskite degradation.
2. Proposition and experimental validation of a decay model for air-exposed quasi-2D perovskite lifetimes.

Regarding PLQY measurements, this thesis' investigation revealed optical misalignment within the measurement setup through rigorous data analysis. By strategically increasing sample dimensions, this thesis successfully reduced PLQY uncertainty and obtained significantly more reliable quantitative results.

4 Crystallinity Manipulation of the Emissive Layer

EML constitutes the core of PeLEDs, whose fundamental design principle involves sequentially transporting carriers through corresponding CTLs for injection into the EML, where radiative recombination generates light(for more details see Sec.1.1). Thus, its crystallinity and defect density directly affect device performance. Typically, EMLs exhibiting higher PLQY possess fewer defects, enabling devices with enhanced EQEs.

This chapter optimizes the PLQY of EML via two approaches: (1) passivating defects in perovskite films using additives and (2) improving perovskite crystallinity through anti-solvent selection.

4.1 Suppression of Crystallization Defects by Small Molecule Additives

Typically, multiple factors within the EML can suppress radiative recombination. For MHPs, the most critical factor inhibiting radiative recombination is ion migration, as detailed in Section 1.1.2. Ion migration can be inhibited through A-site doping. Additionally, optimizing the crystallization process of perovskite facilitates defect suppression.

Several studies also report small molecules improving perovskite crystallization [87, 88, 89, 90, 91]. For example, Yang et al. demonstrated that K^+ significantly enhances crystal orientation. KBr-incorporated samples exhibit higher perovskite peak intensity in XRD patterns, increasing PLQY from 52% to 64% [91]. Analogous effects are observed with self-assembled molecules. Huang et al. found that MeO-2PACz enhances (111)-oriented crystallization and passivate grain boundary defects [87].

Due to the universal optimization ability of small molecules in various EMLs, this thesis also incorporates additives into perovskite to enhance film performance. Prior to this thesis work, a PhD student in our research group discovered that incorporating 2PACz into PSCs significantly enhances PL intensity. Building on this finding and Huang et al.'s report of defect passivation by MeO-2PACz [87], we systematically compared PL intensities of perovskite layers incorporating different 2PACz concentrations to evaluate its defect passivation efficacy. However, it is important to note that the aforementioned studies focused solely on bulk perovskite. As discussed in Section 1.1.3, quasi-2D perovskite offers higher radiative recombination efficiency and a tunable bandgap. Therefore, this study aimed to fabricate quasi-2D perovskite films incorporating 2PACz to determine if the additive retains the advantageous quasi-2D structure across different concentrations. To verify this, we first conducted XRD measurements on the perovskite films containing 2PACz.

The quasi-2D perovskite fabrication process followed the procedure detailed in Sec.2.2.3. Since the spin-coating parameters align with those reported by Bai et al. [37], the resulting perovskite layer thickness is expected to be approximately 60 nm, consistent with their findings. The substrates used during spin-coating were commercially purchased ITO glass, as specified in Sec.2.2.3, featuring an ITO layer of $\sim$150 nm and a glass substrate several millimeters thick.

Given the minimal thickness of both the perovskite and ITO layers, X-rays readily penetrate these films during XRD measurements. Consequently, the diffraction pattern is anticipated to contain two distinct signal components:

1. *Perovskite signals*: Under ideal conditions, only low-dimensional phase peaks (characteristically appearing at $2\theta < 10°$, as discussed in Sec.2.3.1) would be observed. However, practical limitations in achieving phase purity typically result in the additional presence of a bulk-phase peak near $2\theta \approx 15°$.

2. *Substrate signals*: X-rays penetrate the thin ITO layer, yielding diffraction peaks from both ITO and the underlying glass. The ITO layer is expected to produce sharp, crystalline peaks indicative of good crystallinity, while the glass substrate contributes a broad amorphous halo.

The XRD measurement results, presented in Fig. 4-1(a), align with expectations by exhibiting signals from both the substrate and perovskite layer. Both samples shown in Fig. 4-1(a) contain the substrate signals comprise two distinct components: a prominent amorphous background from

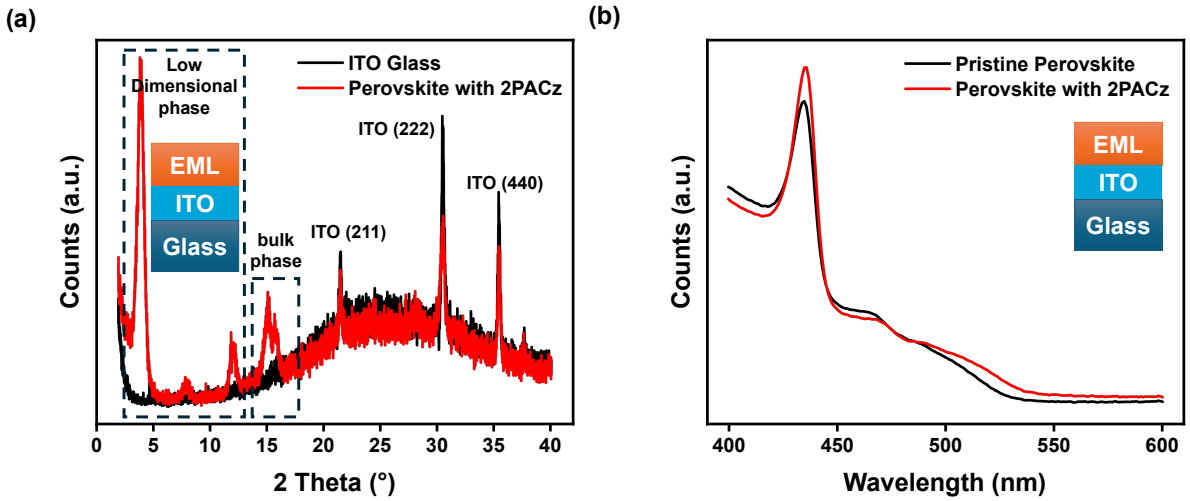

Figure 4-1: Using XRD and UV-Vis spectroscopy to study the phase distribution of perovskite (a) XRD result of 2PACz-perovskite and substrate (b) UV-Vis spectra of pristine perovskite and 2PACz-perovskite

the glass, and a series of crystalline peaks observed at $2\theta = 20.9°$, $30.4°$, and $35.4°$. These peak positions correspond closely to the diffraction pattern reported for ITO by Kerkache et al. [92]. The perovskite (Fig. 4-1(a)) signals show characteristic low-dimensional phase peaks below 15° and bulk-phase features about 15° [67]. Crucially, the XRD patterns reveal that perovskite films incorporating 2PACz exhibit significantly more intense low-dimensional phase peaks compared to bulk-phase signals, indicating excellent formation and distribution of the low-dimensional phase structure.

Following confirmation that the quasi-2D perovskite films fabricated in this study are predominantly composed of low-dimensional phases, the subsequent objective was to characterize their n-phase distribution (for definitions, refer to Section 1.1.3). As detailed in Section 2.3.1, distinct n-phases exhibit different bandgaps arising from quantum confinement effects. This enables the determination of n-phase distribution through UV-Vis absorption spectroscopy. Accordingly, to find out the influence of 2PACz on n-phase distribution, we performed UV-Vis measurements on perovskite samples both with and without 2PACz.

Given the identical fabrication method and composition to quasi-2D perovskite reported by Bai et al[37], the control sample (without 2PACz) is expected to replicate their reported absorption spectrum: a dominant peak at $\lambda \approx 440$ nm corresponding to the n=3 phase, accompanied by less prominent high-n phase features at $\lambda > 440$ nm. Furthermore, since photons with energies exceeding the bandgap of any n-phase can be absorbed, the absorption probability increases at shorter wavelengths (higher energies) where more n-phases contribute to absorption. This results in a characteristic spectral profile with decreasing absorption toward longer wavelengths.

The UV-Vis absorption spectroscopy results, presented in Fig.4-1(b), consistent with Bai et al. [37], both pristine perovskite and 2PACz-incorporated samples exhibit superimposed absorption features from low-dimensional perovskite and large-n phases. The dominant peak at $\lambda = 437$ nm corresponds to the n=3 low-dimensional phase. Additional weaker features appear at $\lambda = 461$ nm (n=4 phase) and $\lambda = 479$ nm (n=5 phase), followed by bulk-phase absorption onset near $\lambda \approx 500$ nm. This progression aligns with characteristic quasi-2D perovskite UV-Vis absorption patterns [93].

It is noteworthy that despite the strongest absorption occurring at $\lambda = 437$ nm, the emission peak emerges at $\lambda \approx 525$ nm due to mixed-phase recombination effects [93].

The absorption spectra profile(Fig.4-1) confirms successful formation of perovskite films with well-distributed n-phases. Notably, perovskite samples incorporating 2PACz additive demonstrate a significantly more pronounced n=3 phase peak. This enhanced prominence indicates improved phase purity

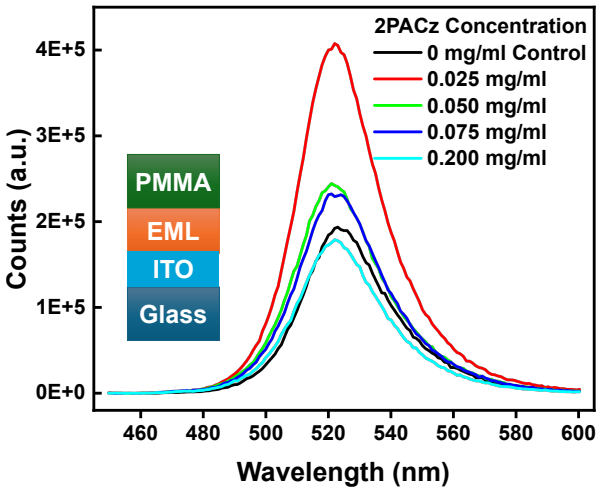

Figure 4-2: PL spectra of perovksite containing different concentrations of 2PACz. The sample with 2PACz concentration of 0.025 mg/ml showed the best PL intensity.

specifically for the n=3 configuration.

After confirming that 2PACz incorporation preserves favorable n-phase distribution in quasi-2D perovskite, this thesis next investigated its defect passivation efficacy. Huang et al. demonstrated that optimal MeO-2PACz concentrations enhance crystal orientation and passivate grain boundary defects, while excess amounts accumulate at boundaries and impede crystal growth [87]. To identify the optimal 2PACz concentration within our quasi-2D system, this thesis tested the following concentration gradient: 0.025, 0.050, 0.075, and 0.2 mg/mL. Besides, to minimize the air-induced degradation on perovskite PL intensity, the measurements employed a PMMA encapsulation layer, as optimized in Sec.2.2.3. The tested device structure consisted of glass/ITO/EML/PMMA.

The PL test results, presented in Fig. 4-2, show that the perovskite sample incorporating 0.025 mg/mL of 2PACz additive exhibited the highest PL intensity (higher PL intensity typically indicating superior quality, as detailed in Sec.2.3.3). Moreover, the PL intensity progressively decreased as the concentration of 2PACz increased. Notably, at a concentration of 0.2 mg/mL, the PL intensity fell below that of the control sample without 2PACz. This demonstrates that, within the concentration range investigated in this study, a 2PACz concentration of 0.025 mg/mL provides the most effective passivation of defects in the perovskite film.

Although this thesis find that 2PACz as an additive demonstrates excellent defect passivation capabilities, recent reports on PeLEDs indicate that employing two or more additives can generate synergistic effects for enhanced defect passivation in perovskite films [94, 95]. Building on this foundation, this thesis further introduced KBr into the 2PACz-perovskite system to explore a further enhancement in crystallinity. PL measurements (Fig.4-3) reveal comparable PL intensities between the control (2PACz-perovskite without KBr) and the 1% KBr sample (relative to Pb^{2+} in precursor). However, PL intensity progressively decreases with higher KBr concentrations. PL intensity shows that adding KBr to the 2PACz-perovskite system cannot effectively improve the PL intensity of perovskite.

Although PL measurements can qualitatively compare luminescence intensities within a sample batch and infer film quality, several limitations prevent its use for quantitative film quality assessment. First, PL intensity is measured using a small excitation spot focused on the film's central region, providing only localized characterization. Second, the open optical path introduces measurement variability when sample position shifts; as detailed in Sec.2.3.3, our PL setup requires manual recalibration of the sample holder between measurements, introducing potential inconsistencies. Finally, PL intensity comparisons are only valid for films with similar chemical compositions. When compositions differ significantly, films with higher extinction coefficients absorb more excitation light. Consequently, sam-

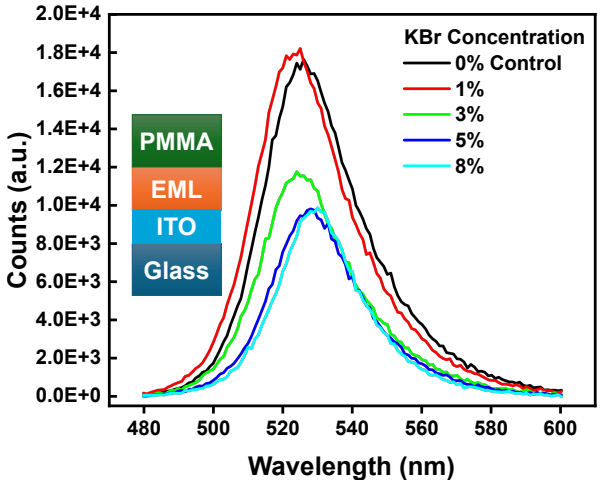

Figure 4-3: PL spectra of 2PACz (0.025 mg/ml)-perovskite with different KBr Concentration(ratio to Pb^{2+}), PL intensity decreases with increasing KBr concentration.

ples with identical radiative recombination efficiency but different extinction coefficients would yield divergent PL intensities, potentially leading to erroneous film quality interpretations.

Therefore, we employed PLQY measurements to further assess on the quality of our samples. This technique, which secures samples within an integrating sphere while simultaneously quantifying absorbed and emitted photons (technical details in Sec.2.3.3), provides the most accurate film quality assessment. We measured PLQY for two samples: a perovskite film with 0.025 mg/mL 2PACz, and another containing both 0.025 mg/mL 2PACz and 5% KBr. As shown in Fig. 4-4, the 2PACz-only sample achieved a champion PLQY of 49%, while the KBr-containing sample showed a slightly lower value of 47%, consistent with the trend observed in PL intensity measurements.

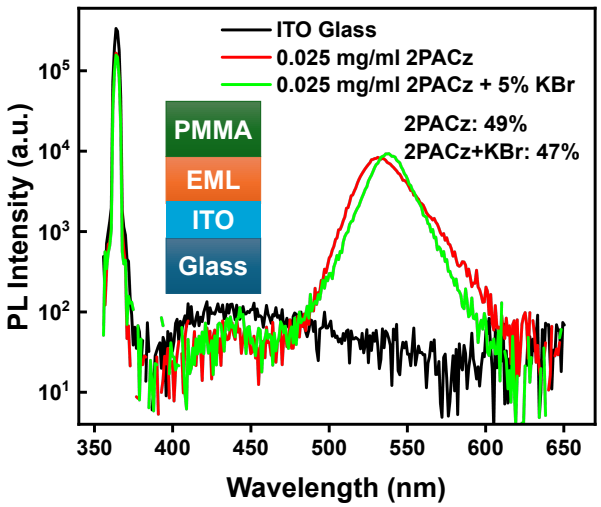

Figure 4-4: PLQY measurement for 2PACz(0.025 mg/ml)-perovskite (PLQY = 49%) and 2PACz (0.025 mg/ml)-perovskite with 5% KBr (PLQY = 47%). PLQY shows that KBr does not produce synergistic effects with 2PACz.

4.2 Antisolvent Smoothening of Thin-Film Morphology

As noted in Sec.2.2.1, the antisolvent method remains the predominant technique for perovskite deposition via spin coating. However, its effectiveness is highly sensitive to processing parameters including spin speed, temperature, and precursor composition [96, 97]. Perovskite precursors typically contain complex organic constituents, often comprising two solvents, three high-concentration organic solutes, and several low-concentration inorganic/organic additives [37, 57, 96]. Differential solubility of these components in antisolvents induces preferential solute precipitation, fundamentally altering film formation mechanisms.

Taylor et al. investigated the mechanism of different antisolvents in simple perovskite precursor systems using DMF:DMSO as solvents and organic iodide with PbI_2 as solutes [98]. They categorized antisolvents into three types (illustrated in Fig. 4-5) based on organic iodide solubility and miscibility with the precursor solvent:

1. Type 1: Type 1 exhibits high miscibility and organic iodide solubility. Rapid application promotes simultaneous, uniform crystallization of PbI_2 and organic halide, yielding well-formed films. Slow application causes rapid dilution due to high miscibility, leading to preferential PbI_2 crystallization before organic halide precipitation, resulting in unreacted PbI_2 that degrades film quality.

2. Type 2: Type 2 demonstrates high miscibility but low organic iodide solubility. This category enables uniform perovskite film formation regardless of application speed due to balanced crystallization kinetics.

3. Type 3: Type 3 features poor miscibility and high organic halide solubility. Slow application allows gradual dilution, facilitating synchronized PbI_2 and organic halide crystallization. Rapid application causes incomplete mixing with the precursor solvent due to poor miscibility, compromising film quality.

Proper antisolvent selection significantly enhances crystallinity and passivates defects.

Considering the crystallographic similarities in octahedral framework formation during crystallization between 3D and quasi-2D perovskites, this study extends Taylor's antisolvent classification methodology to EML optimization. To systematically investigate antisolvent effects on film properties, we employed IPA (Type 1), CB, EA (Type 2), and TL (Type 3) for perovskite fabrication. Subsequent characterization analyzed correlations between antisolvent-induced morphological variations and their impact on PLQY.

Perovskite films fabricated using IPA as the antisolvent exhibit the characteristics shown in Fig.4-6. The SEM image in Fig.4-6(a) reveals a porous morphology with abundant pinhole defects distributed throughout the film. Correspondingly, the PLQY data in Fig.4-6(b) demonstrate that this defective microstructure severely suppresses radiative recombination, yielding a PLQY of merely 14% for IPA-processed perovskite. This value is significantly lower than that achieved with EA as the antisolvent in the previous section. This result indicates that the antisolvent classified as type 1 in Fig.4-5 may fundamentally compromise the optoelectronic properties of our perovskite film.

Both CB and EA belong to the Type 2 antisolvent category. SEM images in Fig.4-7(a) and (b) reveal similar morphological characteristics: smooth, dark homogeneous surfaces with bright needle-like precipitates. This consistency partially validates the antisolvent classification scheme for quasi-2D perovskites.

Tailor et al. [84] investigated these white precipitates through combined SEM-EDS analysis, attributing them to phase aggregation induced by ambient oxygen and moisture exposure. Their composition corresponds to compounds formed between monovalent cations and halide ions from the perovskite lattice. Based on this mechanism, the precipitates in our system likely consist of PEABr or FABr.

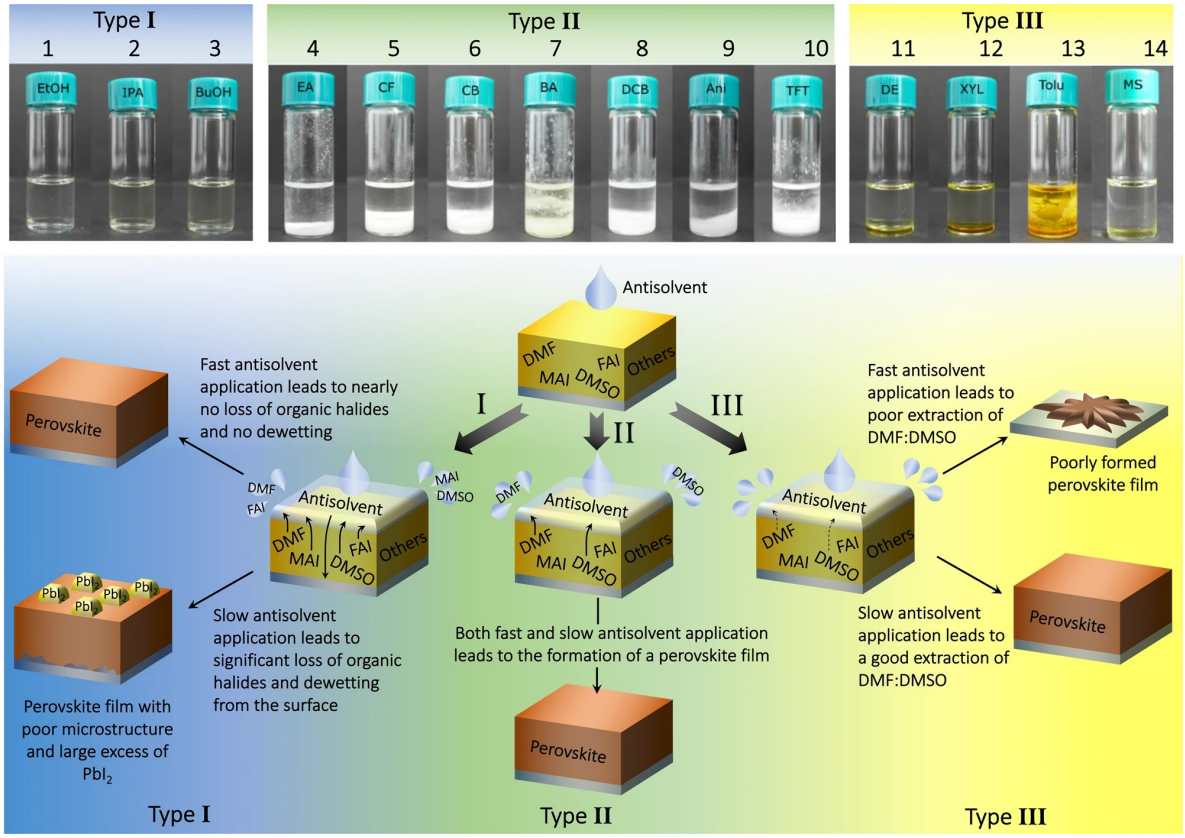

Figure 4-5: Top: solubility of MAI in a solution of DMF:DMSO:antisolvent, meant to simulate the perovskite film intermediate phase during the antisolvent step of fabrication. Bottom: summary of the various mechanisms involved in perovskite film formation by the different categories of antisolvents. ethanol (EtOH), isopropanol (IPA), butyl alcohol (BuOH), ethyl acetate (EA), chloroform (CF), chlorobenzene (CB), butyl acetate (BA), 1,2-dichlorobenzene (DCB), anisole (Ani), trifluorotoluene (TFT), diethyl ether (DEE), m-xylene (Xyl), toluene (TL), mesitylene (MS)[98].

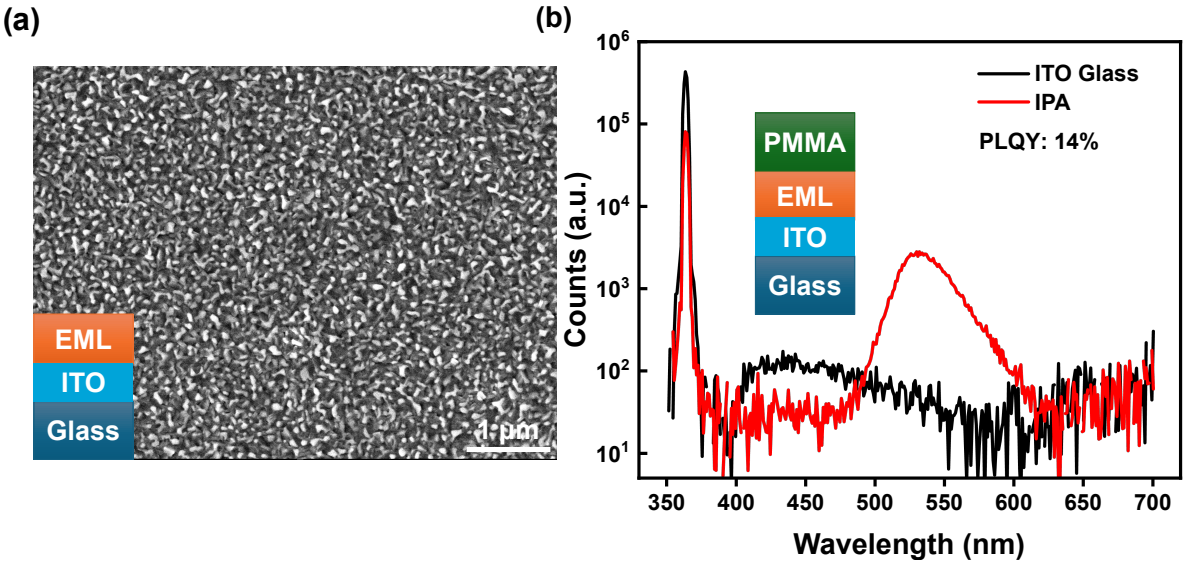

Figure 4-6: Characterization result of perovskite when apply IPA as antisolvent (a) SEM figure, Showing the porous and rough morphology of IPA-processed perovskite. (b) PLQY spectra, its PLQY is 14%, much lower than the perovskite sample mentioned in the previous section.

Despite exhibiting similar surface morphologies in perovskite films processed with CB and EA antisolvents, PLQY measurements revealed a significant discrepancy. As shown in Fig. 4-7(c)(d), EA-treated samples demonstrated substantially higher PLQY compared to their CB-treated counterparts, contradicting initial expectations of comparable optoelectronic performance based on morphological similarity.

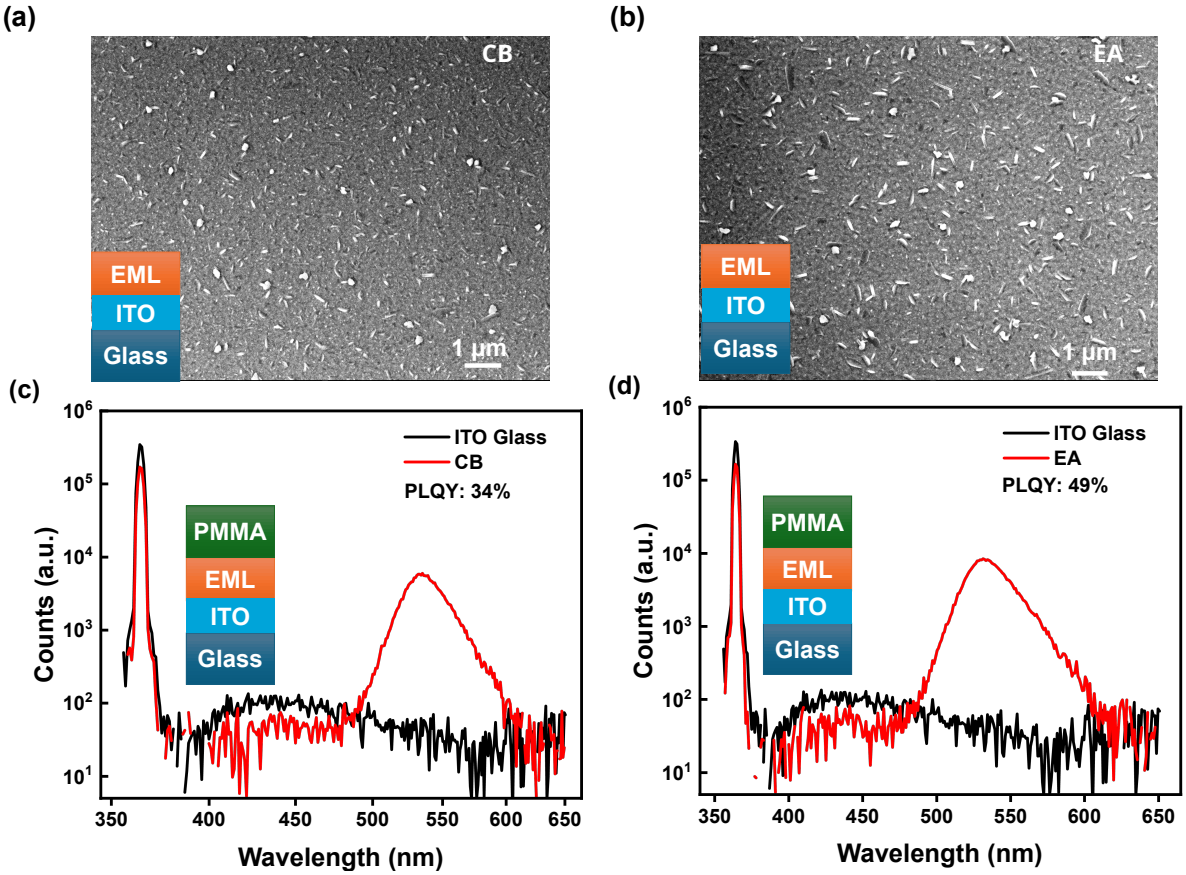

Figure 4-7: Characterization result of perovskite when apply EA and CB as antisolvent. SEM figure when apply (a) CB (b)EA. PLQY spectra when apply (c) CB (d) EA. Two antisolvents resulted in similar morphology but showed different PLQY

To investigate the origin of differing PLQY in perovskite films with identical morphology and composition, this thesis conducted XRD analysis to identify crystallographic factors influencing optoelectronic performance. Results in Fig. 4-8 reveal critical differences (peak assignments detailed in Section 4.1).

First, matching baseline intensities indicate equivalent X-ray penetration through both perovskite and ITO layers to the glass substrate, confirming comparable film thicknesses from spin-coating. This enables direct comparison of perovskite peak intensities to assess relative crystallinity.

Strikingly, EA-treated perovskite exhibits substantially stronger diffraction peaks than its CB-treated counterpart, particularly for low-dimensional phases. In bulk-phase regions, EA-processed films demonstrate not only higher peak intensities but also additional crystalline features absent in CB-processed samples. These results collectively demonstrate EA's superior efficacy in promoting perovskite crystallization.

Compared to Type 1 and Type 2 antisolvents, perovskite films processed with TL exhibit smoother morphology, with surface precipitates transitioning from needle-like to particulate structures as shown in Fig.4-9. Consequently, the superior surface morphology of TL-treated samples should theoretically yield the highest PLQY. To confirm this finding, this thesis tested the TL antisolvent and the results are shown in Fig.4-9. However, experimental measurements revealed slightly less PLQY (47%) compared to EA-processed perovskite (49%).

This thesis attribute this apparent contradiction to TL's inferior miscibility with the DMF:DMSO precursor solvent system. When applied at the same rate optimized for EA, TL likely lacks sufficient

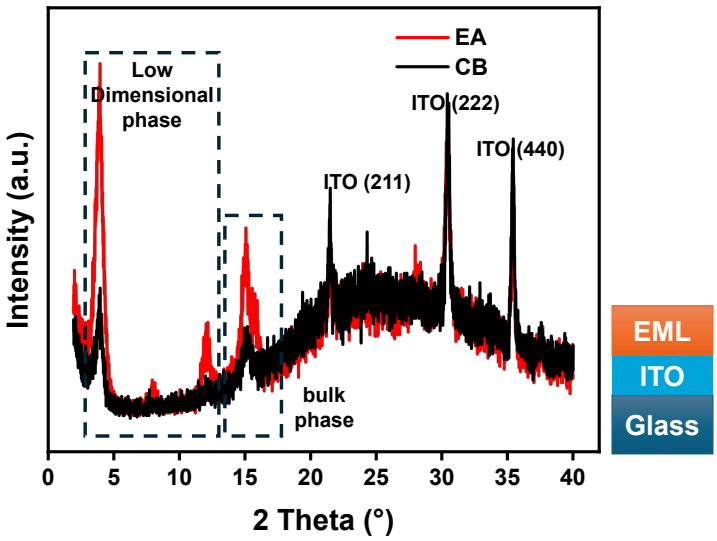

Figure 4-8: XRD measurement results of perovskite processed by EA and CB antisolvents. The high intensity peak of the EA sample reveals its better crystallinity

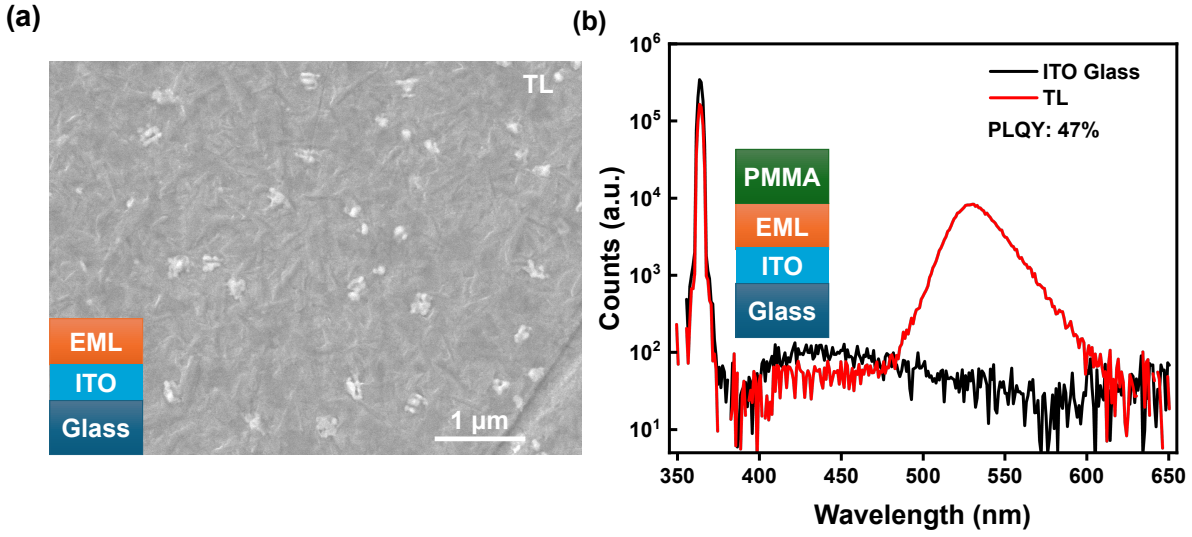

Figure 4-9: Characterization result of perovskite when apply TL as antisolvent (a) SEM figure (b) PLQY spectra

time to fully interact with the precursor solution. This incomplete mixing results in films exhibiting high-quality central morphology but degraded edge morphology.

To validate this hypothesis, this thesis conducted extensive SEM characterization across multiple TL-treated samples. Three distinct morphological regions were identified: (1) The predominant morphology (Fig. 4-9(a)) displays uniform particulate features. (2) Central regions in some samples exhibit clustered needle-like structures (Fig. 4-10(a,c)) with clear intra-cluster crystalline orientation preference but random inter-cluster orientation alignment. These misoriented clusters could create significant grain boundary defects that degrade PLQY. While the formation mechanism remains unclear, controlled growth of these clusters with uniform crystalline orientation could potentially yield high-performance emissive layers with reduced grain boundary defects. (3) Edge regions consistently show irregular surfaces with substantial roughness (Fig. 4-10(b)), attributable to insufficient precursor-antisolvent mixing at peripheral areas during rapid TL application.

During PLQY measurements, all areas of the sample within the integrating sphere theoretically contribute to the photoluminescence signal. Consequently, morphological inhomogeneities inherently reduce the measured PLQY value. Compounding this issue, the FLS 980 system used in this study suffers from suboptimal optical alignment—as detailed in Section 3.2—where the excitation beam predominantly illuminates peripheral sample regions. This configuration disproportionately amplifies contributions from morphologically inferior edges during PLQY quantification. Ultimately, despite TL-treated samples exhibiting superior morphology in most of central regions, their measured PLQY values remain lower than EA-treated counterparts due to this edge-biased illumination artifact.

The spatial heterogeneity—demonstrating morphological degradation at both central (misoriented clusters) and edge (rough texture) regions—confirms that excessive application speed prevents adequate solvent interaction. Controlled crystallization through reduced drip rates or increased TL volumes may resolve this issue by enabling complete precursor-antisolvent mixing, potentially yielding low-defect-density emissive layers.

4.3 Summary

This chapter employs PLQY as the central metric to suppress defects in perovskite films through novel additives and antisolvent optimization. Characterization reveals that among two additives, 2PACz effectively modulates n-phase distribution in low-dimensional perovskites, achieving superior PLQY, whereas KBr incorporation yields no beneficial effects. Crucially, antisolvent selection profoundly influences film morphology and crystallinity, with EA delivering optimal structural properties. The champion film ultimately achieved a PLQY of 49%.

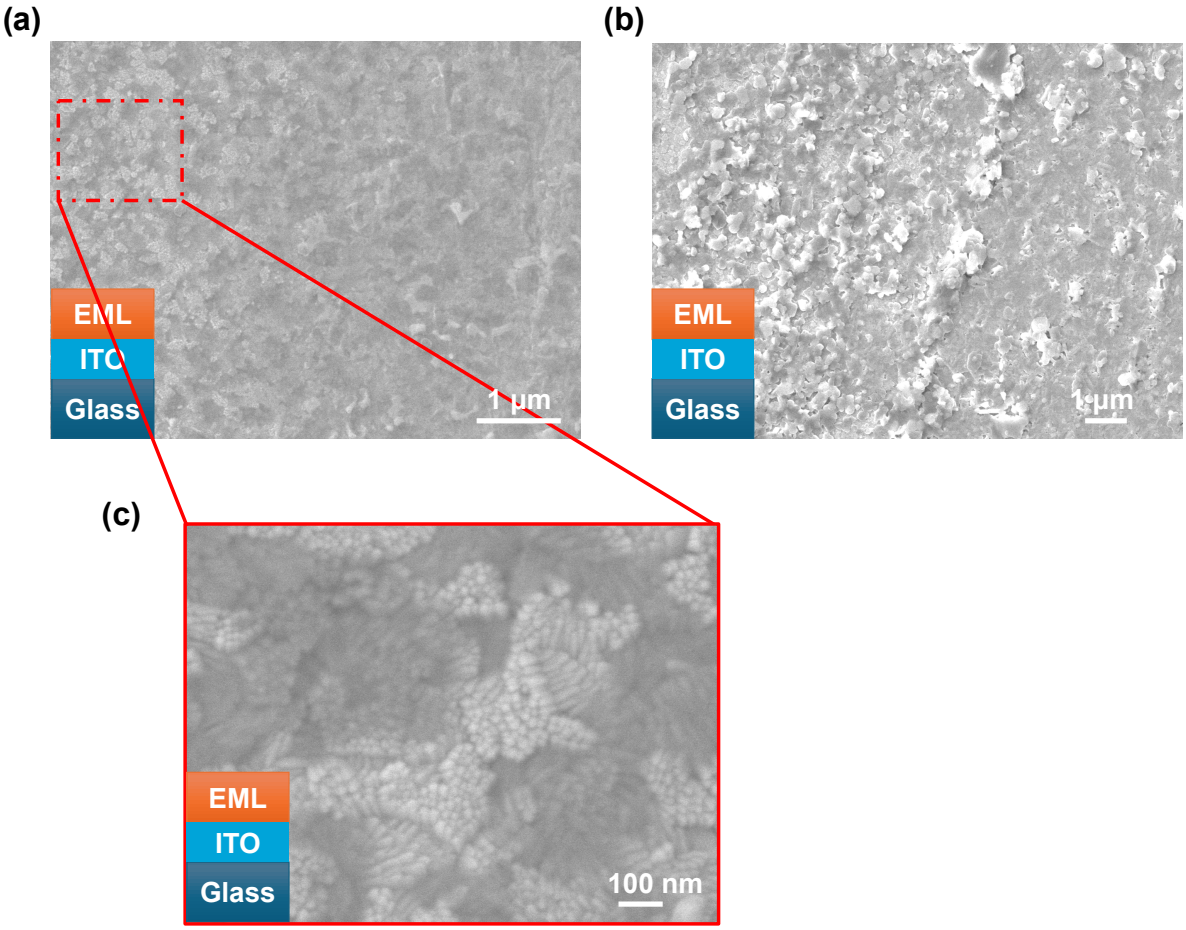

Figure 4-10: SEM characterization results of different TL-processed perovskite sample regions. (a) Clustered needle-like crystals appearing in the central area of some TL-processed samples (b) The rough structure at the edge of most samples (c) The needle-like structure under high magnification shows the intra crystal direction and the inter crystal direction.

5 Regulation of Charge Carrier and Photon Transport Dynamics in Carriers Transport Layer

As discussed in Sec.1.2, appropriate CTL materials selection may help to reduce carrier injection barriers and passivate interfacial defects at EML/CTL. This chapter focuses on the design and selection of device structures, accompanied by characterization of electroluminescence (EL) performance.

5.1 Electron Transport Layer: Spin Coating and Light Management

Most existing PeLED architectures employ thermally evaporated TPBi as ETLs (Sec. 1.2.1). However, TED deposition of organic materials like TPBi risks chamber contamination, potentially compromising other devices fabricated in the same instrument. Currently, the TED chamber within the PVMD group primarily implements an ETL protocol based on C_{60} and bathocuproine (BCP) – both commonly used in PSCs. However, significant differences exist between the band structures of ETLs suitable for PeLEDs versus PSCs. Consequently, this thesis deliberately avoids introducing TPBi into the current deposition chamber. Additionally, TED offers inferior process flexibility and deposition speed compared to solution-based techniques [99, 100]. Therefore, this thesis wants to employs spin coating—a rapid, cost-effective fabrication method non-disruptive to concurrent research activities—for pioneering exploration of PeLEDs fabrication. Inspired by Guo et al.'s demonstration of spin-coated TPBi ETLs [101], this section systematically investigates the feasibility of implementing solution-processed TPBi in functional devices.

It is worth mentioning that the demonstrated advantages of TED in standardized and large-area fabrication position it as a critical manufacturing pathway for industrial scaling[20]. Therefore, once fundamental processing protocols for PeLEDs are established, exploring TED-fabricated TPBi electron transport layers remains a critical research direction.

A primary distinction between spin coating and TED lies in TED's precise thickness control of deposited films [100]. The impact of minor TPBi thickness variations on PeLEDs manifests in two domains: electrical and optical performance. While TPBi's electrical properties exhibit linear correlation with thickness—rendering device characteristics insensitive to minor variations, optical performance cannot be trivially predicted due to light interference phenomena in dielectric films.

The optical behavior of PeLEDs critically influences light extraction efficiency—determining how much photons generated in the EML traverse subsequent layers and emerge from the device. Suboptimal optical architectures can result in significant photon absorption at the metal electrode interface, thereby reducing EQE.

Therefore, this chapter employs COMSOL Multiphysics optical simulations to quantify the influence of TPBi thickness on PeLED optical behavior.

5.1.1 Simulation Validation

Although COMSOL Multiphysics has been globally validated as effective commercial software, this does not guarantee correct implementation by every researcher. To verify the methodology in this thesis, this section establishes a simple system: a single 200 nm thick dielectric thin-film under air-incidence conditions (Fig.5-1(a)). This thesis comparatively calculate angular-dependent optical transmittance using both analytical Fresnel equations (programmed by Python) and COMSOL Multiphysics simulations (Fig.5-1(b)). If the transmittance variations with wavelength and incidence angle, computed via both methods, demonstrate agreement, the simulation conditions implemented in this thesis can be considered appropriate for COMSOL Multiphysics modeling.

For incoming from air, incident on the single-layer thin-film shown in Fig.5-1(a), undergoes to refraction and reflection events at the air/layer interface. Whenever light reaches an interface, both transmission and reflection occur. These phenomena are governed by the Fresnel equations (Eq.5-1 to 5-4). Where t_p,t_s,r_p and r_s are corresponding to transmission coefficient of p/s polarized light and reflectivity coefficient of p/s polarized light; θ_i is angle of incidence and θ_t is the angle of refraction[102].

The total transmittance shown in Fig.5-1(a) results from the cumulative effect of all transmitted light exiting the dielectric film into the air layer.

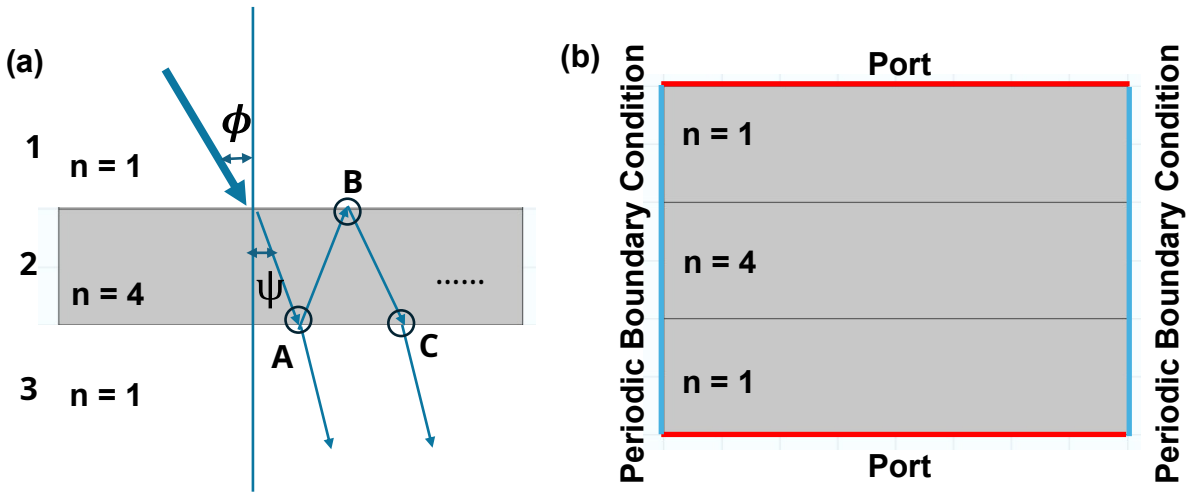

Figure 5-1: The simple model for testing COMSOL Multiphysics settings (a) Geometrical optical description of light propagation in single layer thin-films n=1 simulates the situation of incident from air and outgoing to air, which belongs to the semi-infinite region. Arrows indicate the traces of light. (b) COMSOL Multiphysics' setting. The thickness of each layer is 200 nm. The defination of periodic boundary condition and *port* are detailed in Sec.2.1.4

$$r_s = \frac{n_1 \cos\theta_i - n_2 \cos\theta_t}{n_1 \cos\theta_i + n_2 \cos\theta_t} \tag{5-1}$$

$$r_p = \frac{n_2 \cos\theta_i - n_1 \cos\theta_t}{n_1 \cos\theta_t + n_2 \cos\theta_i} \tag{5-2}$$

$$t_s = \frac{2n_1 \cos\theta_i}{n_1 \cos\theta_i + n_2 \cos\theta_t} \tag{5-3}$$

$$t_p = \frac{2n_1 \cos\theta_i}{n_1 \cos\theta_t + n_2 \cos\theta_i} \tag{5-4}$$

When light incidents into the dielectric layer, it undergoes multiple reflections between the upper and lower interfaces. Given a fixed-thickness dielectric layer, the reflection and transmission coefficients at each interface remain constant, and the phase difference between successive reflections is also invariant.

Defining t_{12} as the transmission coefficient from medium 1 to medium 2, r_{12} as the reflection coefficient from medium 1 to medium 2, and t_{123} as the total transmission coefficient from medium 1 through medium 2 to medium 3, with δ representing the phase shift accumulated during propagation through segment AB in Fig.5-1(a), and assuming incident light intensity of 1.

The light intensity at point A can be expressed as $t_{12}e^{i\delta}$. The light transmitted to medium 3 at A is $t_{12}e^{i\delta}t_{23}$. The light intensity at point B is $t_{12}e^{i\delta}r_{23}e^{i\delta}$, with no light transmitted to medium 3. The light intensity at point C is $t_{12}e^{i\delta}r_{23}e^{i\delta}r_{21}e^{i\delta}$, with transmitted intensity $t_{12}e^{i\delta}r_{23}e^{i\delta}r_{21}e^{i\delta}t_{23}$. By extension, each arrival at the lower interface exhibits an intensity multiplicative factor of $r_{21}r_{23}e^{i2\delta}$ relative to the previous cycle. Summing this geometric series yields the total transmission t_{123} as given in Eq.5-5.

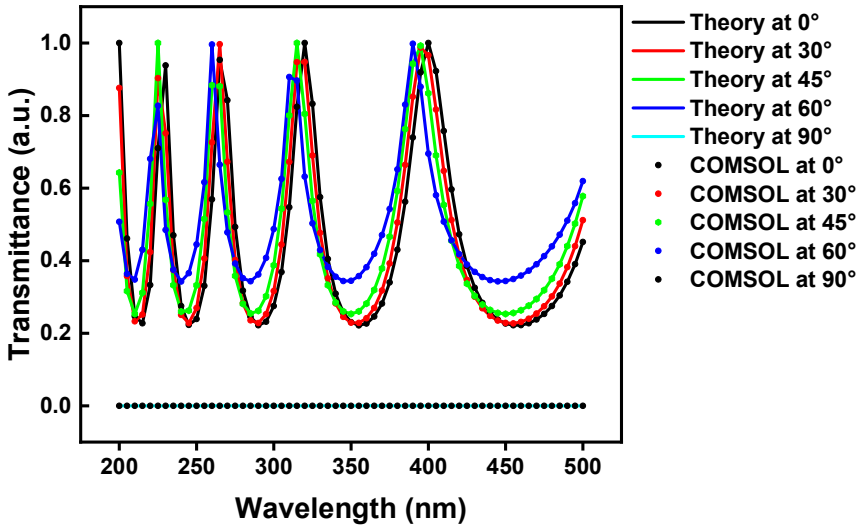

Figure 5-2: Inter verification by calculated transmittance via COMSOL Multiphysics and Fresnel equation

$$t = \frac{t_{12}t_{23}e^{i\delta}}{1 - r_{21}r_{23}} \tag{5-5}$$

$$\delta = \pi\upsilon(\frac{2n_2 d}{cos\psi} - \frac{2d}{cos\psi} sin\psi \sin\phi) \tag{5-6}$$

By combining equation Eq.5-1 to Eq.5-6, we can obtain the transmittance of light at different incident angles.

On the other hands, this section also employs COMSOL Multiphysics to simulate light propagation through the identical structure. The simulation configuration, shown in Fig.5-1(b), implements periodic *ports* at the top and bottom boundaries(The definition of different boundary conditions are detailed in Sec.2.1.4), with periodic boundary conditions applied to both lateral sides. The wave vector is specified as "From periodic *port*" to compute transmittance for both p-polarized and s-polarized light. The total transmittance is then calculated as the average of these two polarization components(defination of different boundary conditions are detailed in Sec.2.1.4).

Finally, the optical transmittance values obtained from COMSOL Multiphysics and those calculated via Fresnel equations are plotted and comparatively analyzed. As shown in Fig.5-2, near-perfect agreement is observed between both datasets, validating the accuracy of our wave optics module implementation for simulating light transmission through multilayer thin-film structures.

5.1.2 Abstraction of Physical Models

The PeLED structure is depicted in Fig.5-3(a). Photons generated within the EML propagate bidirectionally: downward-traveling light exits through the glass substrate, while upward-propagating light reflects at the metal electrode interface, reflecting the light to the front side of the device.

Theoretically, calculating outcoupling efficiency requires full optical analysis of the entire PeLED structure, including the EML. However, optical behavior within the EML involves three complex coupled phenomena:

1. *Condensed Matter Physics*: Nonequilibrium spontaneous emission under carriers injection.

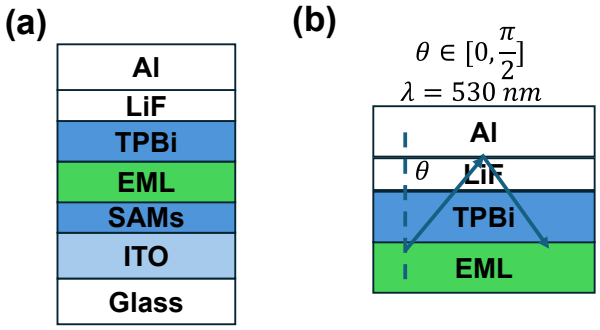

Figure 5-3: PeLEDs structure (a) the device in actual fabrication (b) the half-device optically simulated by COMSOL Multiphysics

2. *Condensed Matter-optics*: Photon absorption and re-emission during propagation through perovskite.

3. *Classical Optics*: Phase modulation and interfacial refraction/transmission/reflection in linear media.

The coupling between these effects significantly complicates comprehensive modeling.

Despite multiphysics simulations being capable of handling such multiscale problems, the time constraints of this Master's thesis necessitate a simplified approach. This thesis decouples the optical analysis by separating the PeLEDs into two substacks: Top stack: EML/TPBi/LiF/Ag and bottom stack: EML/SAMs/ITO/Glass. For a given photon generation rate in the EML, maximum outcoupling efficiency is achieved when the top stack exhibits high reflectivity while the bottom stack maintains high transmittance.

Since TPBi exclusively influences top-stack reflectivity, this thesis investigates the relationship between TPBi thickness (d_{TPBi}) and angularly averaged reflectivity at $\lambda = 530$ nm across all incident angles (Fig.5-3(b)).

This simulation employs monochromatic light at $\lambda = 530$ nm for two primary reasons. First, perovskite EL peaks exhibit narrow FWHM[5], and the material's optical properties remain relatively constant across the perovskite emission spectrum [37, 103], allowing them to be treated as wavelength-independent constants. Second, as demonstrated in Sec.4.1, most perovskite samples exhibit PL peaks between 520-530 nm, with EL peaks typically comparable with PL maxima. What's more, given that the EML fabrication process in this work follows Bai et al.'s methodology, which similarly used $\lambda = 530$ nm for simulations, this thesis adopt the same wavelength for consistency.

Optical simulations incorporate three material parameters per layer: thickness (d), refractive index (n), and extinction coefficient (k). Values for the simulated half-device from Fig.5-3 are shown in Tab.5-1.

Table 5-1: Materials and their optical property used in simulation 2($\lambda = 530(nm)$)[37, 103]

Materials	**Refractive Index**	**Extinction coefficient**	**Thickness (nm)**
Perovskite	1.94	0	30
TPBi	1.73	0	60
LiF	1.39	0	2
Al	0.93	6.4	120

Edge effects represent another critical consideration in optical system simulation. When light interacts with the boundaries of simulated structures, complex refraction phenomena at these edges

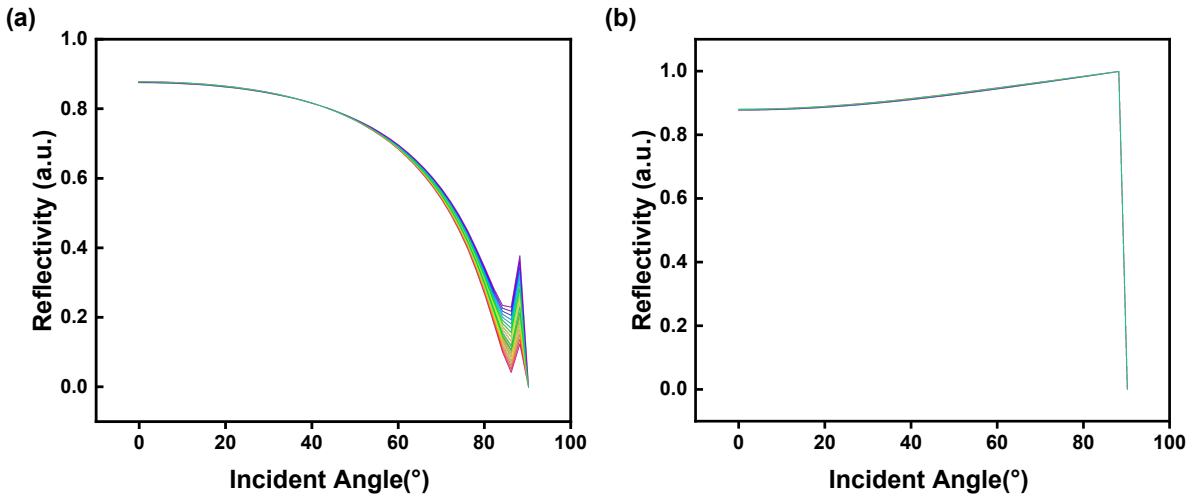

Figure 5-4: Simulation Result by COMSOL Multiphysics (a) Reflectivity of p polarized mode under different incident angle and different d_{TPBi} (b) Reflectivity of s polarized mode under different incident angle and different d_{TPBi}

may influence the overall simulation accuracy. The magnitude of such effects depends critically on the sample dimensions. Given the device's nanoscale thickness (∼10 nm) versus macroscopic lateral dimensions (2.5 × 2.5 cm^2), edge effects were neglected by approximating the structure as laterally infinite. Periodic boundary conditions were applied laterally, with *port* boundaries at top/bottom interfaces to monitor radiative energy flux.

Furthermore, the LED devices fabricated in this study function as planar light sources. Under ideal conditions, their angular emission profile follows a Lambertian distribution (Fig.5-5(a)) [104]. All optical simulations implemented this fundamental assumption.

5.1.3 Simulation Results

Simulated reflectance at $\lambda = 530$ nm for the structure in Fig.5-3, performed using the Wave Optics Module in COMSOL Multiphysics, are presented in Fig.5-4(b. Key observations reveal that the angular dependence of reflectance $R(\theta, d_{\mathrm{TPBi}})$ follows conventional optics behavior for light transitioning from lower to higher refractive index media.

For p-polarized light, $R_p(\theta, d_{\mathrm{TPBi}})$ decreases with increasing θ until reaching a Brewster-like angle, beyond which it increases. Notably, thicker TPBi layers induce both the Brewster-like angle move toward lower θ values and enhanced reflectance at the Brewster-like angle.

Conversely, s-polarized reflectance exhibits marginal reduction with increasing d_{TPBi}.

Here, the light reflectance obtained via COMSOL simulations remains a function of both incident angle and TPBi layer thickness. Therefore, the angular dependence of EML emission must be incorporated to derive the final reflectance as a function of TPBi thickness. In ideal situation, the angular variation of EML emission is typically measured using goniometric photometry [79]. However, for an ideal LED, the angular light intensity distribution often follows the Lambertian approximation. This work assumes that the angular emission profile conforms to the Lambertian approximation, expressed as $I_\theta = I_0 \cos\theta$, where I_0 is the intensity at the normal direction, θ is the emission angle relative to the surface normal, and I_θ represents the intensity at angle θ (Fig. 5-5(a)). The total reflectance of the upper half-device is subsequently calculated using Eq.5-7 to 5-9, here R_p and R_s are the reflectivity of p polarized light and s polarized light.

$$R_p(d) = \frac{\int_0^{\pi/2} R_p(\theta, d_{\mathrm{TPBi}}) \cdot I(\theta) d\theta}{\int_0^{\pi/2} I(\theta) d\theta} \tag{5-7}$$

$$R_s(d) = \frac{\int_0^{\pi/2} R_s(\theta, d_{\mathrm{TPBi}}) \cdot I(\theta) d\theta}{\int_0^{\pi/2} I(\theta) d\theta} \tag{5-8}$$

$$R_{\mathrm{total}} = \frac{R_s + R_p}{2} \tag{5-9}$$

Here, R_p and R_s are the reflectivity of p polarized light and s polarized light, Iθ is Lambertian distribution and R_{total} is the reflection of non-polarized light. Simulation results in Fig.5-5(b) demonstrate that R_p decreases monotonically with increasing d_{TPBi}, while R_s shows a complementary increase. Crucially, the total reflectance R_{total} remains largely invariant across the thickness variation. This theoretical analysis confirms that in principle, replacing TED by spin-coating for TPBi deposition won't limiting the performance of PeLEDs.

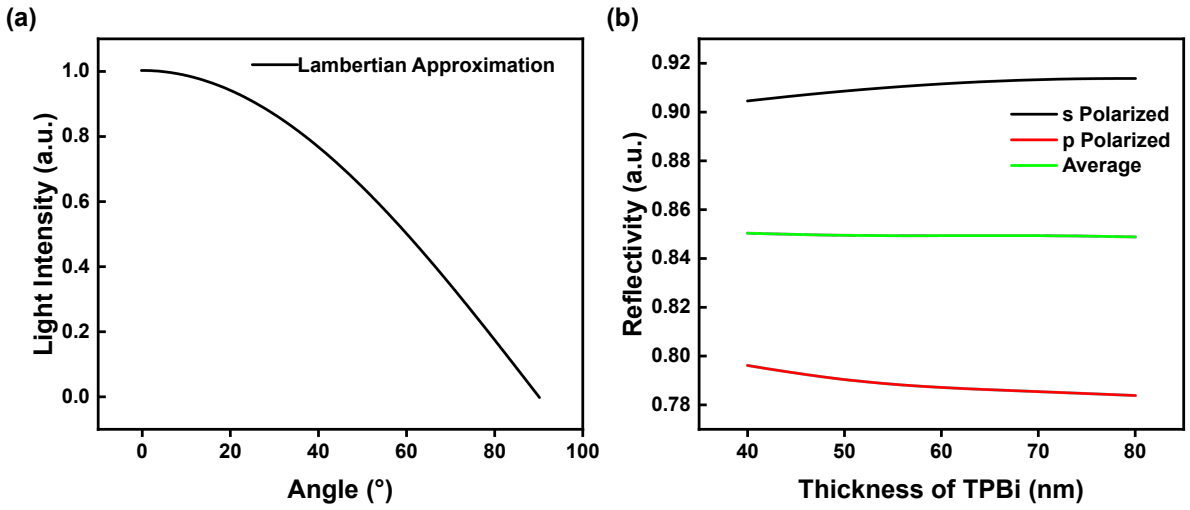

Figure 5-5: Calculation of total reflectivity of the device (a) Assumption that the incident light intensity varies with angle: Lambertian distribution (e) Reflectivity under different d_{TPBi}

5.2 Hole Transport Layer: Self-assembled Monolayer and Electron Tunneling

As detailed in Sec. 1.2.1, there are two predominant HTLs: PEDOT:PSS and NiO_x in PeLEDs fabrication. The former suffers from its intrinsic acidity nature that decomposes ITO electrodes, degrades perovskites, and quenches excitons[38]. The latter exhibits poor interfacial adhesion with perovskites, resulting in substantial defect formation at the heterojunction[52].

The carbazole phosphonic acid (PACz) family molecule is a new class of molecule developed to address these challenges that they became popular in the field of PVK solar cells [105, 72, 106]. Structurally, PACz family organic compounds typically feature a carbazole group as the head group, phosphoric acid as the anchoring group, and a carbon chain linking the two (Fig.5-6(a)). The carbazole group consists of a pyrrole ring that connects two benzene rings, forming a symmetric structure. This highly conjugated structure greatly enhances the stability and electron affinity of PACz. The anchoring group in PACz can covalently bind with TCO substrates in either a monodentate or bidentate fashion. This contributes to the formation of ultrathin and stable SAMs monolayer with excellent robustness

against external environmental factors. Additionally, the anchoring group can effectively passivate defects on the substrate surface through specific binding [105]. Researchers have gradually developed various types of PACz organic compounds to meet different application requirements (Fig.5-6(a)) [107].

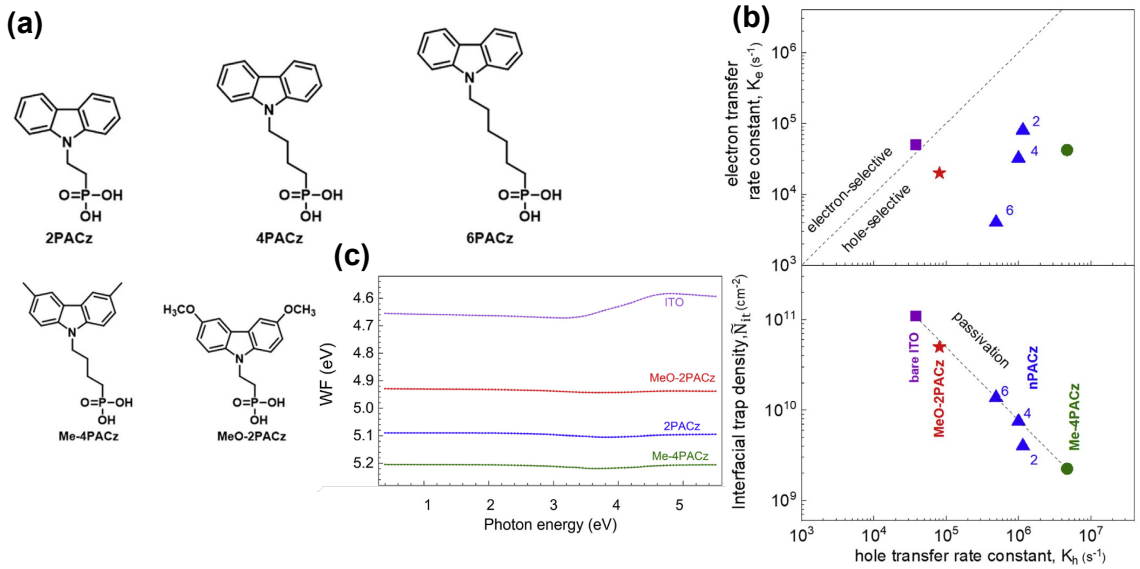

Figure 5-6: (a) Structure of different PACz (b) WF of different PACz [108](c) Hole transfer rate constant and interfacial trap density of different PACz [108]

In 2019, Al-Ashouri et al. [109] first applied two PACz molecules: 2PACz and MeO-PACz into PSCs. Compared to the previously established SAM molecule V1036 ((2-3,6-bis[bis(4-methoxyphenyl)amino]-9H-carbazol-9-ylethyl)phosphonic acid) and common HTL material PTAA (poly[bis(4-phenyl)(2,4,6-trimethylphenyl)amine]), the PACz derivatives achieved superior passivation of defects at the HTL/perovskite interface due to their unique molecular design. Almasabi et al. [110] found that MeO-PACz exhibits excellent wettability and mechanical adhesion to perovskite layers. Their DFT models revealed that the enhanced adhesion arises from the additional functional group (-MeO) in MeO-2PACz, which tends to form hydrogen bonds between the hydrogen atoms of the -MeO group and surface iodine atoms of $FAPbI_3$. This interaction significantly improved the performance of MeO-2PACz. In 2020, Al-Ashouri et al. reported achieving an exceptionally high PCE of 29.15% in monolithic perovskite/silicon tandem solar cells using Me-4PACz as the HTL [111].

Building on this foundation, Levine et al. used transient surface photovoltage (SPV) and TRPL techniques to study the effects of different PACz structures on hole transfer rate constants and interfacial trap densities in ITO/SAM/perovskite architectures [108]. They proposed that the chain length of the linker group affects the barrier thickness of the organic layer. For n-PACz molecules with identical anchoring and head groups, a higher n value leads to a lower hole transfer rate. In contrast, the type of head and anchoring groups significantly influences the dipole moment of SAM molecules, thereby altering their properties. For instance, although MeO-2PACz exhibits excellent wettability, its hole transfer rate is much lower than that of 2PACz. On the other hand, Me-4PACz, while having a slightly lower hole transfer rate than 2PACz, demonstrates superior defect passivation performance, which explains its remarkable success in PSCs (Fig.5-6(b). Moreover, structural differences also impact the work function of SAMs, further influencing their effectiveness in various device applications (Fig.5-6(c)).

Despite the significant success of SAMs in PSCs owing to their exceptional hole-transport and defect-passivation capabilities, their implementation in PeLEDs remains limited. Existing studies primarily utilize SAM molecules as interfacial modifiers to enhance morphological properties between

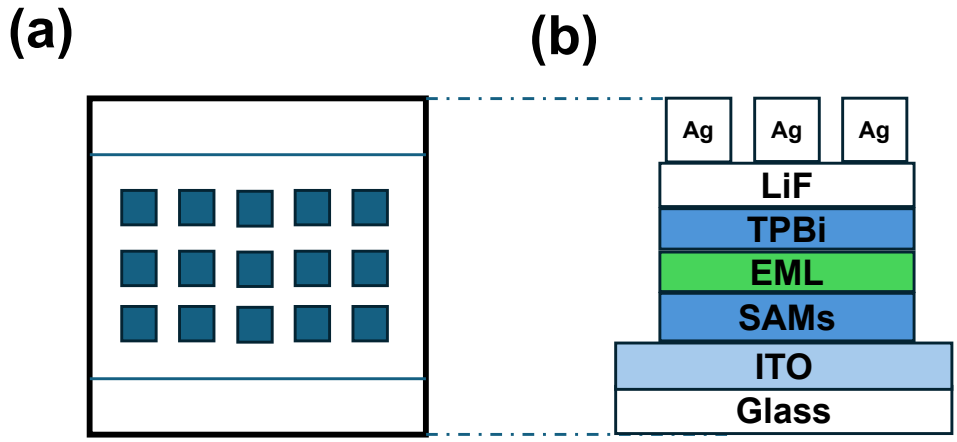

Figure 5-7: Schematic illustration of the device configuration for J-V characterization (not to scale). (a) Top view showing 15 active sub-devices (3×3 mm^2 each) patterned in the central region. Only these Ag-electrode-covered areas are electrically active. The peripheral ITO contacts remain exposed. (b) Cross-sectional view of the layered device architecture.

conventional HTLs and perovskites—particularly between MOs and perovskite layers [112, 113, 114].

Notably, direct application of PACz molecules as the primary HTL in PeLEDs is exceptionally rare. Shin et al. demonstrated one such implementation in a blue-emitting PeLED (473 nm) using (2-(3,6-dichloro-9H-carbazol-9-yl)ethyl)phosphonic acid (36ClCzEPA), a PACz derivative, as the HTL, achieving an EQE of 4.8% [115]. Given that this efficiency falls below values typically achieved by alternative PeLED architectures [116], the full potential of SAMs in light-emitting devices remains largely unexplored.

During optimization of SAM film morphology, researchers have identified two primary challenges: aggregation and hydrophobicity. Aggregation occurs during spin-coating deposition when intermolecular interactions within SAMs exceed those between SAMs and TCOs, leading to island growth. For instance, Cao et al. observed that Me-4PACz SAM layers exhibit aggregation, causing leakage currents and enhancing nonradiative recombination at interfaces [117, 118]. An effective mitigation strategy involves introducing a secondary, smaller-volume SAM that fills voids between primary SAM molecules, resulting in more uniform films [117, 118]. Hydrophobicity poses another challenge, as hydrophobic head groups hinder perovskite growth. Introducing methoxy groups into PACz-family SAMs enhances layer hydrophilicity, thereby improving subsequent perovskite crystallization [119].

5.2.1 Quantum Tunneling in PeLEDs

With the advantages of PACz molecules, this thesis initially fabricates PeLEDs employing MeO-2PACz and MeO-4PACz as the HTL. We anticipates that the proposed SAMs configuration will deliver three key advantages: Firstly, it should retain the intrinsic benefits of SAMs discussed previously, including facilitating high-quality perovskite growth, providing interfacial defect passivation, and maintaining neutral environment. Secondly, the synergistic combination of large volume PACz and small volume PACz derivatives is expected to enhance film quality and improve ITO surface coverage uniformity, thereby reducing defect density. Finally, the ultrathin HTL architecture should significantly boost hole-injection efficiency into the EML, which is anticipated to dramatically improve PeLED luminance at low operating voltages.

Regarding device fabrication, the PeLED structure (Fig.5-7) incorporates 15 discrete sub-devices, each with an active area of 0.09 cm^2 (Fig.5-7(a)). For optoelectronic characterization, this work employed the PVMD group's glovebox-integrated solar simulator due to the absence of dedicated PeLED measurement systems.

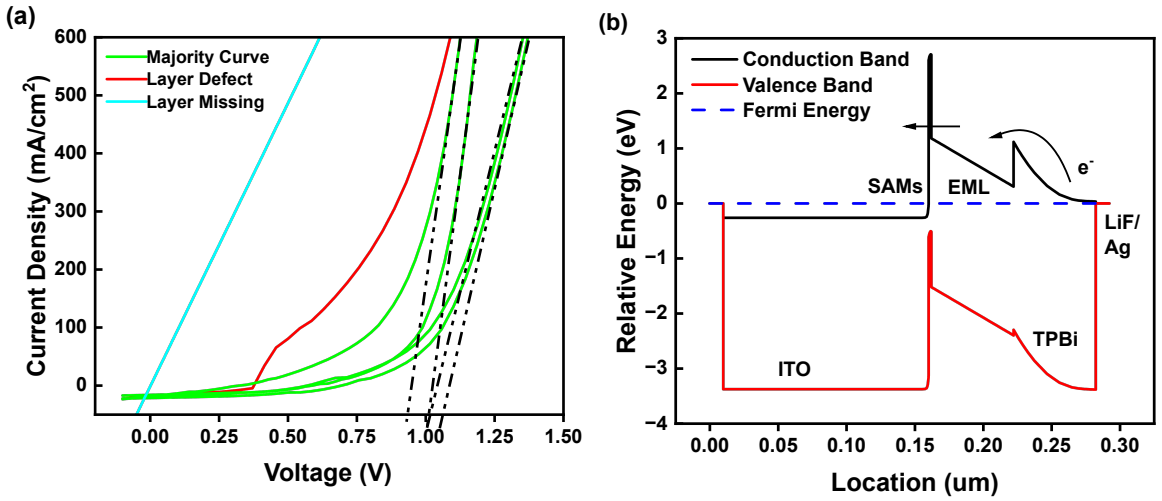

Figure 5-8: (a) Current density-voltage (J-V) characteristics of Glass/ITO/SAMs/EML/TPBi/LiF/Ag devices. The green curve represents typical device behavior, while black and cyan curves indicate defective devices. (b) Energy band diagram of a PeLED architecture without NiO_x interlayer, illustrating direct electron tunneling through the SAMs layer leading to device breakdown.

This setup features a specialized probe charger compatible with the configuration shown in Fig.5-7(b). Measurements were performed by selecting target active areas through the instrument's software interface. However, without integrated photon detection capabilities, characterization was limited to current density-voltage (J-V) profiling via source meter measurements and qualitative assessment of electroluminescence through visual inspection.

The measured current density-voltage (J-V) characteristics are presented in Fig.5-8(a). The green curve represents typical device behavior observed in the majority of sub-devices. These devices exhibit turn-on voltages around 1 V, with their J-V curves transitioning abruptly from exponential to linear behavior beyond this threshold. This characteristic indicates a complete absence of semiconductor properties at operational voltages.

The red curve (Fig.5-8(a)) shows an additional step-like feature at low voltages, suggesting possible pinhole defects in the thin-film structure. Such defects likely enable premature dielectric breakdown at reduced potentials, causing sudden resistance collapse. The cyan curve (Fig.5-8(a)) displays purely ohmic behavior, implying incomplete film coverage where the ITO substrate dominates the electrical characteristics.

Crucially, no electroluminescence was observed in any devices during testing, consistent with the non-diode behavior demonstrated in all J-V profiles.

In this thesis, we attributes the absence of electroluminescence in these PeLEDs to electron tunneling phenomena through the hole transport layer. To enable accurate assessment of carrier behavior in PeLEDs, this thesis employed TCAD Sentaurus simulations [120], conducted by Dr. Procel Moya (PVMD Group), to model the intrinsic band structure of heterostructured PeLED devices under dark conditions at zero bias. The electrical parameters used in the simulation are detailed in Tab.5-2, with the resulting band diagrams presented in Fig.5-8(b) and Fig.5-9(b).

Although the LUMO of SAMs lies above that of the EML (Fig.5-8(b)), theoretically enabling electron blocking, the ultrathin SAMs (about 2 nm) facilitate direct electron tunneling over radiative recombination in the EML. Consequently, injected electrons preferentially tunnel through the SAM, causing electrical shorts. Current density-voltage (J-V) characteristics in Fig.5-8(a) confirm this mechanism. SAM-based PeLEDs exhibit turn-on voltages near 1 V. The energy that this voltage can give to the electrons is lower than both the EML bandgap (2.78 eV) and the energy barrier of electrons

Table 5-2: Materials and their electrical property used in simulation[37, 121, 122, 123]

Materials	**HOMO (Ionization Energy) (eV)**	**LUMO (Electron Affinity) (eV)**	**Thickness (nm)**
ITO	-4.9	/	150
NiO_x	-5.4	-1.8	30
SAMs	-5.3	-2.1	2
Perovskite	-6.39	-3.61	60
TPBi	-6.2	-2.8	60
Ag/LiF	-4.3	/	120

between EML and the SAM layer (2.70 eV). Instead, this voltage aligns with the energy difference between electrodes and the LUMO of TPBi (1.11 eV), indicating that most injected electrons tunnel through the SAM, resulting in device shorting.

To suppress tunneling effects in the device, a sufficiently thick interfacial layer can theoretically be introduced at either the ITO/HTL or HTL/EML junction. Two candidate materials are available in the glove box during the period of my master thesis: PTAA and NiO_x nanoparticles. However, PTAA presents significant limitations. First, its LUMO level (-2.30 eV) is substantially deeper than those of SAMs and NiO_x (Tab.5-2), resulting in inadequate electron blocking capabilities [124]. Second, we observed that PTAA's pronounced hydrophobicity prevents successful perovskite deposition via spin-coating using our standard fabrication protocol (Sec.2.2.3)—UV illumination of spin-coated perovskite on PTAA substrates yielded no detectable photoluminescence, indicating failed film formation.

In contrast, NiO_x films exhibit enhanced wettability following ultraviolet-ozone treatment after spin-coating. Consequently, a NiO_x interlayer was incorporated as a tunneling barrier. This design serves dual purposes. On the one hand, $NiOx$ possesses a high LUMO level (Fig.5-9(b)), effectively blocking electron injection. On the other hand, the SAM bridges NiO_x and the EML, enhancing interfacial adhesion. One of the sub-devices with NiO_x exhibit pronounced semiconductor characteristics in J-V measurements and produce clearly visible EL shown in the green curve of Fig.5-9(a). The turn-on voltage occurs near 3 V, with current density increasing steeply at higher voltages. This growth rate exceeds those reported for high-efficiency PeLEDs, causing device burnout at low voltages due to excessive current [37].

In this thesis, we attributes the current dissipation to two primary pathways: (1) Radiative recombination occurs when the applied voltage exceeds the EML bandgap, converting injected carriers into light. (2) Due to TPBi's higher electron mobility, electron injection outpaces hole injection. When the bias exceeds the energy barrier between the NiO_x LUMO and electrode work function, excess electrons tunnel through the conduction band, causing instantaneous short-circuit failure. Additionally, the contribution of poor film morphology (characterized by thickness inhomogeneity and pinhole defects) to increased leakage current cannot be ruled out.

It should be noted that no established protocol for NiO_x thickness was found in the literature, and time constraints precluded further optimization measurements. However, based on established PeLED operational principles, this interlayer should typically measure tens of nanometers thick [125].

Additionally, device reproducibility proved challenging: only one of fifteen sub-devices exhibited electroluminescence. Most non-emitting devices displayed characteristics similar to the red curve in Fig.5-9(a), featuring inconsistent turn-on voltages (predominantly below 3 V) and complete linearization of J-V curves around 3 V, indicative of dielectric breakdown.

We attribute this performance variability to non-uniform NiO_x distribution. As detailed in Sec.2.2.3, our protocol involved dispersing NiO_x nanoparticles in aqueous solution via ultrasonication prior to spin-coating. However, we observed significant sedimentation during deposition, evidenced by solution darkening at the container bottom. This phenomenon suggests nanoparticle agglomeration and settling, resulting in thickness variations across the deposited film that compromise the tunneling

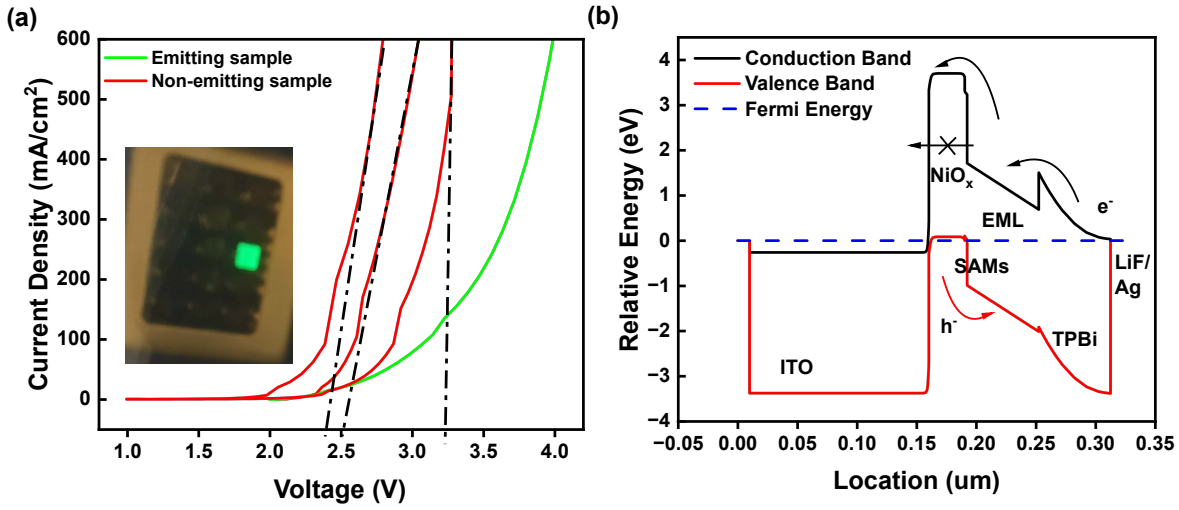

Figure 5-9: (a) J-V characteristics of Glass/ITO/NiO_x/SAMs/EML/TPBi/LiF/Ag devices. The green J-V curve is from luminous sub-device, while red curves are from non-luminous sub-devices. (b) Energy band diagram of a PeLED architecture without NiO_x interlayer, illustrating direct electron tunneling through the SAMs layer leading to device breakdown.

barrier effectiveness. The observed sedimentation during spin-coating (Sec.2.2.3) suggests compromised colloidal stability. To mitigate this, we propose a dual-batch processing strategy: maintaining two identical aqueous NiO_x dispersions subjected to alternating ultrasonication cycles during spin coating. This ensures at least one dispersion remains within its transient stability window (typically <2 min post-sonication) during deposition, minimizing agglomeration-driven thickness variations that compromise tunneling barrier functionality.

5.2.2 Feasibility study of Tunneling Barrier Layer

As discussed in the previous section, optimal device performance requires trade-off of two competing phenomena:

(1): Leakage current suppression needs increased HTL thickness,

(2): Enhanced hole injection for excess electron neutralization requires thinner HTL.

Current strategies predominantly incorporate polymeric insulating interlayers (e.g., polyethylene glycol (PEG), polyethylenimine ethoxylated (PEIE), PMMA, and polyvinylpyrrolidone (PVP)) at HTL/EML or EML/ETL interfaces to block electron overflow [37, 126, 127]. However, these insulating layers intrinsically obstacle hole transport, consequently degrading PeLED performance at low operating voltages.

Compared to alternative HTLs, SAMs enable superior perovskite morphology at minimal thicknesses. This ultrathin configuration inherently enhances hole injection efficiency. Theoretical high-performance PeLEDs could be realized if tunneling currents are suppressed. To achieve this, an ultra-thin MOs interlayer between SAMs and ITO is proposed by me to simultaneously block electron tunneling and optimize carrier injection barriers. This approach would enhance hole injection to balance carrier transport, ultimately boosting luminance and EQE.

For preliminary thickness estimation, this work employs a quantum mechanical model for tunneling through rectangular barriers. Consider a one-dimensional system (Fig.5-10) with a finite energy barrier of width a and height V_0. When a is sufficiently large (tunneling probability $\ll 1$), the amplitude-squared ratio of transmitted to incident electron wavefunctions follows Eq.5-10 [128]. Three critical assumptions apply when adapting this model to PeLED band structures:

1. Electron mass need to be replaced by the effective mass (m_e^*). While the specific m_e^* for quasi-2D

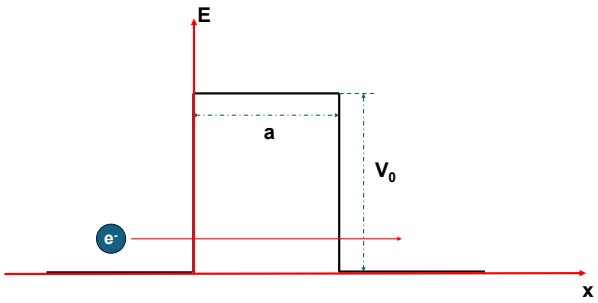

Figure 5-10: Quantum Tunneling Model, a barrier with width a and height V_0. When an electron hits a potential barrier, there is a certain probability that it will pass through the barrier and cause quantum tunneling.

$PEA_2(FAPbBr_3)_2PbBr_4$ ($n = 3$) was unavailable, density functional theory (DFT) calculations for analogous quasi-2D perovskites indicate m_e^* values between 0.1 m_e and 0.3 m_e [129] (where m_e is the free electron mass).

2. In the actual device, the LUMO at the ITO side exhibits lower energy, while the LUMO at the EML side shows higher energy (Fig. 5-10(a)). However, to simplify computation, this thesis neglects the energy offset across the barrier under the high-barrier approximation where tunneling probability dominates.

3. Applied bias did not modifies both barrier height and width during device operation.

Consequently, electron tunneling probabilities were computed across varying barrier widths and effective masses (m_e^*), as shown in Fig.5-11. Notably, at SAM barrier thicknesses of 1-2 nm, significant tunneling probability persists. However, increasing the thickness beyond this range causes exponential reduction—a transition from 2 nm to 5 nm decreases tunneling probability by ten orders of magnitude. This explains the operational devices reported by Shin *et al.* using solely 36ClCzEPA as HTL, where marginal barrier thickening sufficiently suppressed tunneling currents.

It should be emphasized that these calculations assume ideal thin-film conditions. Practical fabrication introduces thickness non-uniformity and defects, necessitating actual barrier thicknesses exceeding theoretical value. Therefore, the optimal thickness range should be empirically explored between 3.5 nm and 10 nm. Based on this analysis, this work proposes that incorporating a tunneling barrier layer of several nanometers—adjacent to the SAM—can effectively block electron tunneling while enabling efficient low-voltage electroluminescence.

$$T = e^{-2\beta a} \tag{5-10}$$

$$\beta = \frac{\sqrt{2m_e V_0}}{\hbar} \tag{5-11}$$

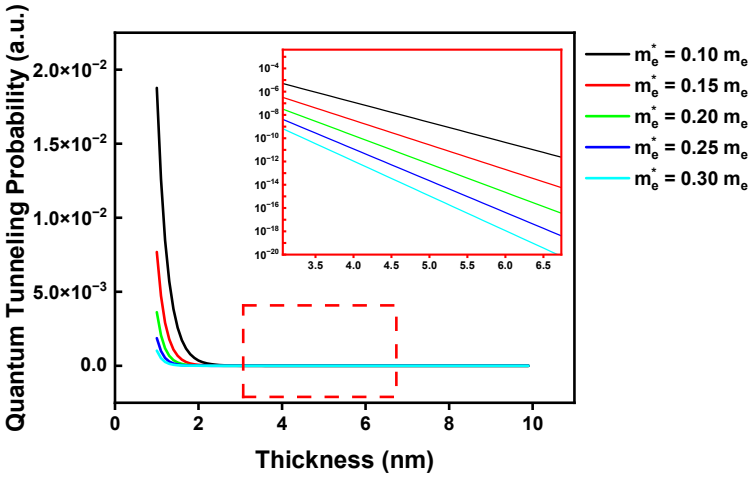

Figure 5-11: Simulated quantum tunneling probability: $T \propto \exp(-2d\sqrt{2m^*\Delta E/\hbar^2}$ where d = barrier width, m^* = effective mass. Exponential decay dominates thickness dependence.

5.3 Summary

This chapter combines theoretical modeling and experimental fabrication to investigate the distinctive properties of both TPBi and SAM layers in perovskite LEDs. For the TPBi layer, thickness-dependent optical simulations were performed, confirming the scientific feasibility of replacing thermal evaporation with solution-processed spin coating. Regarding SAM films, fabricated layers revealed significant electron tunneling during device operation, prompting quantitative analysis of thickness effects on tunneling probability.

Ultimately, operational light-emitting devices were successfully fabricated. The introduction of a thin electron barrier layer is proposed as a critical optimization pathway for future development.

6 Conclusion

This thesis successfully demonstrates the first operational perovskite LEDs fabricated within the PVMD group, establishing foundational device architectures and characterization methodologies. The principal accomplishments include:

1. **Development of a dynamic spin-coating process for uniform PMMA encapsulation layers.** TRPL analysis confirmed these coatings significantly retard ambient perovskite degradation. However, the PMMA layers proved insufficient for maintaining EML stability throughout measurements, indicating the requirement for advanced encapsulation strategies.

2. **Identification and partial correction of alignment issues in the PLQY measurement setup, resulting in reduced experimental uncertainty.** Subsequent analysis revealed residual alignment imperfections requiring further calibration refinement.

3. **Design a home-made EQE test system.** Future work should focus on developing automated measurement protocols to enhance testing efficiency, and reduce the measurement time.

4. **Quantification of TPBi thickness effects on optical performance via COMSOL Multiphysics simulations.** Results confirm that thickness variations independent to spin-coating processes do not significantly impact optical characteristics in the present device architecture.

5. **Synthesis of quasi-2D perovskites with ∼530 nm emission through combined PEA/FA A-site doping.** Optimization using 2PACz additive (0.025 mg/ml) and EA anti-solvent yielded champion devices with 49% PLQY. Theoretical analysis suggests TL anti-solvents may enable superior morphological control.

6. **Successful fabrication of operational PeLEDs using NiO_x/SAMs bilayer hole transport structures.** Quantification of HTL thickness-dependent electron tunneling effects provides clear pathways for future device optimization. We propose that a thin NiO_x interlayer (1-5 nm thickness) integrated within the SAM-based hole transport structure effectively suppresses electron tunneling while simultaneously maximizing hole injection efficiency. This configuration leverages the complementary functions of both materials: the SAM provides template growth for the EML, while the ultrathin NiO_x layer serves as an electron tunneling barrier that impedes electron leakage without significantly decreasing hole transfer efficiency.

7 Outlook

Due to the primary objective of this thesis being the design of all LED layers and fabrication of a working device, we could only simultaneously advance all aspects of device fabrication while avoiding excessive depth in any single aspect. This has left room for optimization in nearly every aspect addressed in this thesis.

1. The most promising development direction is tunneling barrier layer fabrication. Currently, to apply SAMs in PeLEDs while simultaneously suppressing electron tunneling, researchers mainly employ two methods: The first uses Metal Oxides as HTL with SAMs as an interfacial passivation layer between Metal Oxides and Perovskite. The second inserts an insulating layer as an electron Barrier Layer at an interface in PeLEDs. Although both can block electron tunneling, they damage the luminance and EQE of PeLEDs at low voltages. If we can insert a NiO_x layer (estimated 1-5 nm thickness) between ITO and SAMs using atomic layer deposition that precisely blocks electron tunneling, then such PeLEDs are expected to demonstrate state-of-the-art performance in low-voltage operating environments.

2. Second, in this thesis, we consider the main reason for the lower PLQY of TL samples compared to EA samples to be the non-uniformity of TL samples. If the uniformity of TL application during antisolvent dripping can be improved, then it may be possible to further increase the PLQY of perovskite. Near the end of writing this thesis, we noticed a newly published paper (first published 01.08.2025) that uses pressure-driven atomization of CB to uniformly apply CB [130]. Although reference to this work was not incorporated into the main text, we consider that utilizing this work could effectively solve the problems we encountered when preparing samples with TL. Initial attempts could start with purchasing press-type sprayers commonly used in cosmetics. If using sprayers improves sample uniformity, then more expensive professional equipment such as ultrasonic nebulizers can be further introduced.

3. Additionally, in fabrication, the electrode design adopted for time-saving requires further optimization. The currently used electrode is a LiF/Ag structure. The work function of this electrode structure is as deep as -4.3 eV, requiring electrons injected from the electrode into ETL to overcome a high energy barrier. This structure is used solely because the PVMD group has mature recipes for depositing Ag. The currently more common structure in the research of PeLEds is LiF/Al, whose work function is generally -3.0 eV, having better matching with the LUMO of TPBi (-2.8 eV).

4. Regarding characterization issues, both EML measurement and PeLEDs measurement still have problems. TRPL tests show that the current PMMA encapsulation method cannot maintain perovskite stability in air for extended periods (>5 mins). We consider there are two solutions to this problem. The first is to customize transparent containers that can seal individual perovskite samples, and measure the entire container during optical tests such as PL, TRPL, PLQY, and UV-Vis spectroscopy. The second is to cover the perovskite sample (glass/ITO/EML) with another glass layer, filling and bonding the gap between the two glasses with UV-resin. Currently, UV-resin has been purchased and is ready for testing to evaluate the sealing effect of this method. Data analysis also shows there is an optical path misalignment problem when testing with FLS 980. This problem likely causes the main part of the light spot to hit the edge of the sample, resulting in measured values lower than true values, requiring further calibration.

5. PeLEDs testing is more challenging. Although we currently have equipment that can perform voltage scanning and obtain corresponding current and LED brightness, we currently don't know the lifetime of PeLEDs under operation. Considering the testing equipment is directly exposed to air, we may need to consider extreme cases where PeLEDs operational lifetime is less than 1 minute. Voltage scans during PeLEDs measurement typically require acquiring more than 10

spectra. If manual saving is used each time, assuming each operation takes 5 seconds, then just saving 10 spectra would take nearly 1 minute. Therefore, programming the equipment to achieve automated measurement is necessary.

8 Acknowledgements

Time passes swiftly; the two years have elapsed in an instant. I have once again overcome numerous challenges to attain a higher academic degree.

First and foremost, I extend my deepest gratitude to my parents and family. Funding my tuition and living expenses during these two years in the Netherlands represented a substantial financial commitment. Without your emotional and financial support, I could not have completed my studies at TU Delft.

Secondly, I sincerely thank my four supervisors: Dr. L. (Luana) Mazzarella, Dr. M. (Moumita) Rana, Dr. A. (Amarante) J. Böttger, and PhD student Haoxu Wang. Cultivating a researcher requires developing multifaceted capabilities beyond foundational scientific knowledge. This includes the ability to stay abreast of research developments, design and analyze experiments, collaborate across disciplines, and effectively communicate results through publications or presentations. Throughout my Master's thesis project, my supervisors dedicated themselves to helping me understand and develop these essential skills, laying a crucial foundation for my future scientific work.

I also wish to acknowledge the PVMD group and Optoelectronic Materials group for providing the instrumentation, equipment, and materials essential for conducting my Master's thesis research.

Furthermore, I am grateful to all my colleagues within the PVMD group. Our interactions—whether sharing daily experiences, discussing research progress, exchanging cross-disciplinary insights, or learning about each other's cultural backgrounds—served as a constant wellspring of inspiration for my scientific endeavors.

Finally, I express my appreciation to everyone who supported me during my Master's program. Each step forward was aided by your encouragement.

I offer particular thanks to my partner. To ensure my focus remained on academic and professional development, you steadfastly prioritized my growth, forgoing your presence to allow me the space to concentrate fully on advancing my knowledge and skills.

References

[1] Zissis, G., Bertoldi, P., and Serrenho, T. *Update on the Status of LED-Lighting world market since 2018*. EUR 30500 EN. Luxembourg: Publications Office of the European Union, 2021. ISBN: 978-92-76-27244-1. DOI: 10.2760/759859.

[2] International Energy Agency. *SHC Task 50, Advanced Lighting Solutions for Retrofitting Buildings*. Technical Report. IEA Solar Heating and Cooling Programme, 2013.

[3] Skarżyński, K. and Wiśniewski, A. "The reflections on energy costs and efficacy problems of modern LED lamps". *Energy Reports* 122024, pp. 4926–4937. ISSN: 2352-4847. DOI: 10.1016/j.egyr.2024.10.038.

[4] Banerjee, S. et al. "Evolution of Organic Light Emitting Diode (OLED) Materials and their Impact on Display Technology". *Chemistry–An Asian Journal* 20(4), 2025, e202401291. DOI: 10.1002/asia.202401291.

[5] Quan, L. N. et al. "Perovskites for light emission". *Advanced Materials* 30(45), 2018, p. 1801996. DOI: 10.1002/adma.201801996.

[6] Zhang, M. et al. "Towards sustainable perovskite light-emitting diodes". *Nature Sustainability* 8(3), 2025, pp. 1–10. ISSN: 2398-9629. DOI: 10.1038/s41893-024-01503-7.

[7] Zhang, K. et al. "Opportunities and challenges in perovskite LED commercialization". *Journal of Materials Chemistry C* 9(11), 2021, pp. 3795–3799. DOI: 10.1039/D1TC00232E.

[8] Feng, S.-C. et al. "Efficient and Stable Red Perovskite Light-Emitting Diodes via Thermodynamic Crystallization Control". *Advanced Materials* 36(44), 2024, p. 2410255. DOI: 10.1002/adma.202410255.

[9] Yu, R. et al. "Frontiers in Green Perovskite Light-Emitting Diodes". *Laser & Photonics Reviews* 18(4), 2024, p. 2300780. DOI: 10.1002/lpor.202300780.

[10] Orlovskaya, N., Browning, N., et al., eds. *Mixed Ionic Electronic Conducting Perovskites for Advanced Energy Systems*. Vol. 173. NATO Science Series II: Mathematics, Physics and Chemistry. Dordrecht: Springer, 2004. ISBN: 978-1-4020-2344-6. DOI: 10.1007/978-1-4020-2344-6.

[11] Li, C. C. et al. "Lead-free perovskites for flexible optoelectronics". *Materials Today Electronics* 82024, p. 100095. ISSN: 2772-9494. DOI: https://doi.org/10.1016/j.mtelec.2024.100095.

[12] Borriello, I., Cantele, G., and Ninno, D. "Ab initio investigation of hybrid organic-inorganic perovskites based on tin halides". *Physical Review B—Condensed Matter and Materials Physics* 77(23), 2008, p. 235214. DOI: 10.1103/PhysRevB.77.235214.

[13] Filip, M. R. et al. "Steric engineering of metal-halide perovskites with tunable optical band gaps". *Nature communications* 5(1), 2014, p. 5757. DOI: 10.1038/ncomms6757.

[14] Oranskaia, A. et al. "Halogen migration in hybrid perovskites: the organic cation matters". *The Journal of Physical Chemistry Letters* 9(18), 2018, pp. 5474–5480. DOI: 10.1021/acs.jpclett.8b02522.

[15] Zhu, T. and Gong, X. "Low-dimensional perovskite materials and their optoelectronics". *InfoMat* 3(10), 2021, pp. 1039–1069. DOI: 10.1002/inf2.12211.

[16] Wang, H.-C. et al. "Perovskite quantum dots and their application in light-emitting diodes". *Small* 14(1), 2018, p. 1702433. DOI: 10.1039/D1TC00232E.

[17] Dey, A. et al. "State of the art and prospects for halide perovskite nanocrystals". *ACS nano* 15(7), 2021, pp. 10775–10981. DOI: 10.1021/acsnano.0c08903.

[18] Wang, K.-H. et al. "Chemical regulation of metal halide perovskite nanomaterials for efficient light-emitting diodes". *Science China Chemistry* 612018, pp. 1047–1061. DOI: 10.1007/s11426-018-9325-7.

[19] Lai, M. et al. “Intrinsic anion diffusivity in lead halide perovskites is facilitated by a soft lattice”. *Proceedings of the National Academy of Sciences* 115(47), 2018, pp. 11929–11934. DOI: 10.1073/pnas.1812718115.

[20] Wu, Z. et al. “Recent progress in meniscus coating for large-area perovskite solar cells and solar modules”. *Sustainable Energy & Fuels* 5(7), 2021, pp. 1926–1951. DOI: 10.1039/d0se01774d.

[21] Han, B. et al. “Stable, efficient red perovskite light-emitting diodes by (α, δ)-CsPbI3 phase engineering”. *Advanced Functional Materials* 28(47), 2018, p. 1804285. DOI: 10.1002/adfm.201804285.

[22] Bi, L. et al. “Deciphering the roles of MA-based volatile additives for α-FAPbI3 to enable efficient inverted perovskite solar cells”. *Journal of the American Chemical Society* 145(10), 2023, pp. 5920–5929. DOI: 10.1021/jacs.2c13566.

[23] Pellet, N. et al. “Mixed-organic-cation Perovskite photovoltaics for enhanced solar-light harvesting”. *Angewandte Chemie International Edition* 53(12), 2014, pp. 3151–3157. DOI: 10.1002/anie.201309361.

[24] Chu, Z. et al. “Large cation ethylammonium incorporated perovskite for efficient and spectra stable blue light-emitting diodes”. *Nature Communications* 11(1), 2020, p. 4165. DOI: 10.1038/s41467-020-17943-6.

[25] Zhang, L. et al. “Ultra-bright and highly efficient inorganic based perovskite light-emitting diodes”. *Nature communications* 8(1), 2017, p. 15640. DOI: 10.1038/ncomms15640.

[26] Peng, X. et al. “A review of low-dimensional metal halide perovskites for blue light emitting diodes”. *Journal of Alloys and Compounds* 8832021, p. 160727. DOI: 10.1016/j.jallcom.2021.160727.

[27] Lin, Y. et al. “Suppressed ion migration in low-dimensional perovskites”. *ACS Energy Letters* 2(7), 2017, pp. 1571–1572. DOI: 10.1021/acsenergylett.7b00442.

[28] Wu, G. et al. “Surface passivation using 2D perovskites toward efficient and stable perovskite solar cells”. *Advanced Materials* 34(8), 2022, p. 2105635. DOI: 10.1002/adma.202105635.

[29] Zheng, X. et al. “Managing grains and interfaces via ligand anchoring enables 22.3%-efficiency inverted perovskite solar cells”. *Nature Energy* 5(2), 2020, pp. 131–140. DOI: 10.1038/s41560-019-0538-4.

[30] Huang, Z. et al. “Suppressed ion migration in reduced-dimensional perovskites improves operating stability”. *ACS Energy Letters* 4(7), 2019, pp. 1521–1527. DOI: 10.1021/acsenergylett.9b00892.

[31] Zou, Y. et al. “Highly efficient and stable 2D–3D perovskite solar cells fabricated by interfacial modification”. *Nanotechnology* 30(27), 2019, p. 275202. DOI: 10.1088/1361-6528/ab10f3.

[32] Chen, X. et al. “Crystallization control via ligand–perovskite coordination for high-performance flexible perovskite solar cells”. *Energy & Environmental Science* 17(17), 2024, pp. 6256–6267. DOI: 10.1039/d4ee02279c.

[33] Li, C. et al. “Multifunctional ligand-manipulated luminescence and electric transport of CsPbI3 perovskite nanocrystals for red light-emitting diodes”. *Chemical Engineering Journal* 4932024, p. 152483. DOI: 10.1016/j.cej.2024.152483.

[34] Feng, W. et al. “Polymer-assisted crystal growth regulation and defect passivation for efficient perovskite light-emitting diodes”. *Advanced Functional Materials* 32(34), 2022, p. 2203371. DOI: 10.1002/adfm.202203371.

[35] Ma, D. et al. “Distribution control enables efficient reduced-dimensional perovskite LEDs”. *Nature* 599(7886), 2021, pp. 594–598. DOI: 10.1038/s41586-021-03997-z.

[36] Guo, Z. et al. “Promoting energy transfer via manipulation of crystallization kinetics of quasi-2D perovskites for efficient green light-emitting diodes”. *Advanced Materials* 33(40), 2021, p. 2102246. DOI: 10.1002/adma.202102246.

[37] Bai, W. et al. “Perovskite light-emitting diodes with an external quantum efficiency exceeding 30%”. *Advanced Materials* 35(39), 2023, p. 2302283. DOI: 10.1002/adma.202302283.

[38] Lee, J. et al. “Advancements in Interfacial Engineering for Perovskite Light-Emitting Diodes”. *Chemistry–A European Journal* 30(32), 2024, e202400372. DOI: 10.1002/chem.202400372.

[39] Chen, L.-C. et al. “Influence of PMMA on all-inorganic halide perovskite CsPbBr3 quantum dots combined with polymer matrix”. *Materials* 12(6), 2019, p. 985. DOI: 10.3390/ma12060985.

[40] Kim, G.-i. et al. “Optimizing Green Perovskite Light-Emitting Diodes through a Solution-Processed Triple-Layer HTL Strategy”. *IEEE Electron Device Letters* 45(6), 2024, pp. 1028–1031. DOI: 10.1109/LED.2024.3387982.

[41] Gangishetty, M. K. et al. “Reducing architecture limitations for efficient blue perovskite light-emitting diodes”. *Advanced Materials* 30(20), 2018, p. 1706226. DOI: 10.1002/adma.201706226.

[42] Gunnarsson, W. B. et al. “Improved charge balance in green perovskite light-emitting diodes with atomic-layer-deposited Al2O3”. *ACS Applied Materials & Interfaces* 14(30), 2022, pp. 34247–34252. DOI: 10.1021/acsami.2c00860.

[43] Du, P. et al. “Thermal evaporation for halide perovskite optoelectronics: fundamentals, progress, and outlook”. *Advanced Optical Materials* 10(4), 2022, p. 2101770. DOI: 10.1002/adom.202101770.

[44] Ouyang, D., Huang, Z., and Choy, W. C. “Solution-processed metal oxide nanocrystals as carrier transport layers in organic and perovskite solar cells”. *Advanced Functional Materials* 29(1), 2019, p. 1804660. DOI: 10.1002/adfm.201804660.

[45] Li, J. et al. “Hole transport layer modification for highly efficient divalent ion-doped pure blue perovskite light-emitting diodes”. *Advanced Optical Materials* 11(1), 2023, p. 2201883. DOI: 10.1002/adom.202201883.

[46] Kittel, C. and McEuen, P. *Introduction to solid state physics(8th ed.)* American: John Wiley & Sons, 2018, pp. 0 - 704. ISBN: 978-0-471-41526-8. DOI: 10.1107/S0365110X54000448.

[47] Islam, A. et al. “Organic Hole-Transport Layers: An Innovative Approach for Efficient Perovskite Light-Emitting Diodes”. *Advanced Optical Materials* 12(17), 2024, p. 2303304. DOI: 10.1002/adom.202303304.

[48] Fan, X. et al. “PEDOT: PSS materials for optoelectronics, thermoelectrics, and flexible and stretchable electronics”. *Journal of Materials Chemistry A* 11(35), 2023, pp. 18561–18591. DOI: 10.1039/d3ta03213b.

[49] Chen, W.-H. et al. “Simple fabrication of a highly conductive and passivated PEDOT: PSS film via cryo-controlled quasi-congealing spin-coating for flexible perovskite solar cells”. *Journal of Materials Chemistry C* 7(33), 2019, pp. 10247–10256. DOI: 10.1039/c9tc02744k.

[50] Yang, X. et al. “Simultaneously Enhancing the Efficiency and Stability of Perovskite Solar Cells by Using P3HT/PEDOT: PSS as a Double Hole Transport Layer”. *Nanomaterials* 14(18), 2024, p. 1476. DOI: 10.3390/nano14181476.

[51] Peng, J. et al. “Efficient perovskite light-emitting diodes achieved by suppressing the acidic surface of PEDOT: PSS films”. *Chemical Engineering Journal* 4852024, p. 149668. DOI: 10.1016/j.cej.2024.149668.

[52] Patel, V. D. and Gupta, D. “Solution-processed metal-oxide based hole transport layers for organic and perovskite solar cell: A review”. *Materials Today Communications* 312022, p. 103664. ISSN: 2352-4928. DOI: 10.1016/j.mtcomm.2022.103664.

[53] Liu, X.-K. et al. "Metal halide perovskites for light-emitting diodes". *Nature Materials* 20(1), 2021, pp. 10–21. DOI: 10.1038/s41563-020-0784-7.

[54] Chen, S. et al. "Preparation and properties of p-type transparent conductive Cu-doped NiO films". *Thin Solid Films* 519(15), 2011, pp. 4944–4947. DOI: 10.1016/j.tsf.2011.01.058.

[55] Wang, Y. et al. "Study on electron transport characterization in TPBi thin films and OLED application". *The Journal of Physical Chemistry C* 125(30), 2021, pp. 16753–16758. DOI: 10.1021/acs.jpcc.1c04138.

[56] Turak, A. "Interfacial degradation in organic optoelectronics". *RSC advances* 3(18), 2013, pp. 6188–6225. DOI: 10.1039/C2RA22770C.

[57] Liu, B. et al. "Highly Efficient Green Light-Emitting Diodes from All-Inorganic Perovskite Nanocrystals Enabled by a New Electron Transport Layer". *Advanced Optical Materials* 6(11), 2018, p. 1800220. DOI: 10.1002/adom.201800220.

[58] COMSOL AB. *Wave Optics Module User's Guide*. Version 5.4. Accessed: 2025-07-07. COMSOL AB. 2025.

[59] Tyona, M. "A theoritical study on spin coating technique". *Advances in materials Research* 2(4), 2013, p. 195. DOI: 10.12989/amr.2013.2.4.195.

[60] Jeon, N. J. et al. "Solvent engineering for high-performance inorganic–organic hybrid perovskite solar cells". *Nature materials* 13(9), 2014, pp. 897–903. DOI: 10.1038/NMAT4014.

[61] Konstantakou, M. et al. "Anti-solvent crystallization strategies for highly efficient perovskite solar cells". *Crystals* 7(10), 2017, p. 291. DOI: 10.3390/cryst7100291.

[62] Tan, K. W. et al. "Thermally induced structural evolution and performance of mesoporous block copolymer-directed alumina perovskite solar cells". *ACS nano* 8(5), 2014, pp. 4730–4739. DOI: 10.1021/nn500526t.

[63] Qin, M. et al. "Manipulating the mixed-perovskite crystallization pathway unveiled by in situ GIWAXS". *Advanced Materials* 31(25), 2019, p. 1901284. DOI: 10.1002/adma.201901284.

[64] Picollo, M., Aceto, M., and Vitorino, T. "UV-Vis spectroscopy". *Physical sciences reviews* 4(4), 2019, p. 20180008. DOI: 10.1515/psr-2018-0008.

[65] Qin, X. et al. "Compositional optimization of mixed cation Dion–Jacobson perovskites for efficient green light emission". *Journal of Materials Chemistry C* 10(1), 2022, pp. 108–114. DOI: 10.1039/d1tc04743d.

[66] Liu, Y. et al. "Two-inch-sized perovskite CH3NH3PbX3 (X= Cl, Br, I) crystals: growth and characterization". *Adv. Mater* 27(35), 2015, pp. 5176–5183. DOI: 10.1002/adma.201502597.

[67] Kong, L. et al. "A spacer cation assisted nucleation and growth strategy enables efficient and high-luminance quasi-2D perovskite LEDs". *Advanced Functional Materials* 33(2), 2023, p. 2209186. DOI: 10.1002/adfm.202209186.

[68] Epp, J. "X-ray diffraction (XRD) techniques for materials characterization". *Materials characterization using nondestructive evaluation (NDE) methods*. Woodhead Publishing, 2016, pp. 81–124. ISBN: 978-0-08-100040-3. DOI: 10.1016/C2014-0-00661-2.

[69] Aftab, S. et al. "From lab to luminescence: perovskite-based dimensional integrations pushing LED boundaries," *Materials Today Physics* 46,2024, p. 101490. DOI: 10.1016/j.mtphys.2024.101490.

[70] Jena, A. K. et al. "Stabilization of α-CsPbI3 in ambient room temperature conditions by incorporating Eu into CsPbI3". *Chemistry of Materials* 30(19), 2018, pp. 6668–6674. DOI: 10.1021/acs.chemmater.8b01808.

[71] Zhou, W. et al. "Fundamentals of scanning electron microscopy (SEM)". *Scanning microscopy for nanotechnology: techniques and applications*2007, pp. 1–40. DOI: 10.3390/app132312600.

[72] Zhang, S. et al. “Minimizing buried interfacial defects for efficient inverted perovskite solar cells”. *Science* 380(6643), 2023, pp. 404–409. DOI: 10.1126/science.adg3755.

[73] Khanna, V. K. “Physical understanding and technological control of carrier lifetimes in semiconductor materials and devices: A critique of conceptual development, state of the art and applications”. *Progress in quantum electronics* 29(2), 2005, pp. 59–163. DOI: 10.1016/j.pquantelec.2005.01.002.

[74] Wang, J. et al. “Bulk passivation and interfacial passivation for perovskite solar cells: Which one is more effective?” *Advanced Materials Interfaces* 8(9), 2021, p. 2002078. DOI: 10.1002/admi.202002078.

[75] Tesa, M., Gakamsky, A., and Thomson, S. “Measurement of photoluminescence lifetimes in the μs range”. *Tech Note, May*2018, pp. 48–51.

[76] Kirchartz, T. et al. “Photoluminescence-based characterization of halide perovskites for photovoltaics”. *Advanced energy materials* 10(26), 2020, p. 1904134. DOI: 10.1002/aenm.201904134.

[77] Chen, Q. et al. “Enhanced thermal stability of MAPbBr3 nanocrystals by ligand modification”. *Materials Research Bulletin* 1572023, p. 112009. DOI: 10.1016/j.materresbull.2022.112009.

[78] Fries, F. and Reineke, S. “Statistical treatment of photoluminescence quantum yield measurements”. *Scientific reports* 9(1), 2019, p. 15638. DOI: 10.1038/s41598-019-51718-4.

[79] Jin, W. et al. “On the accurate characterization of quantum-dot light-emitting diodes for display applications”. *npj Flexible Electronics* 6(1), 2022, p. 35. DOI: 10.1038/s41528-022-00169-5.

[80] Schneider, T. et al. *CIE 250:2022 Spectroradiometric Measurement of Optical Radiation Sources*. Technical Report 250. Cancels and replaces CIE 063-1984; Covers wavelength range 200–2500 nm. CIE - International Commission on Illumination, 2022, p. 99. DOI: 10.25039/TR.250.2022.

[81] Wilderspin, T. J., De Rossi, F., and Watson, T. M. “A simple method to evaluate the effectiveness of encapsulation materials for perovskite solar cells”. *Solar Energy* 1392016, pp. 426–432. DOI: 10.1016/j.solener.2016.09.038.

[82] Qaid, S. M. et al. “Enhancement of light amplification of CsPbBr3 perovskite quantum dot films via surface encapsulation by PMMA polymer”. *Polymers* 13(15), 2021, p. 2574. DOI: 10.3390/polym13152574.

[83] Yang, F., Kang, D.-W., and Kim, Y.-S. “Improved interface of ZnO/CH3NH3PbI3 by a dynamic spin-coating process for efficient perovskite solar cells”. *RSC Advances* 7(31), 2017, pp. 19030–19038. DOI: 10.1039/C7RA01869J.

[84] Tailor, N. K. et al. “Recent progress in morphology optimization in perovskite solar cell”. en. *Journal of Materials Chemistry A* 8(41), 2020, pp. 21356–21386. ISSN: 2050-7488, 2050-7496. DOI: 10.1039/D0TA00143K.

[85] Abdi-Jalebi, M. et al. “Potassium-and rubidium-passivated alloyed perovskite films: Optoelectronic properties and moisture stability”. *ACS energy letters* 3(11), 2018, pp. 2671–2678. DOI: 10.1021/acsenergylett.8b01504.

[86] Wei, L. et al. “Error analysis for the Fourier domain offset estimation algorithm”. *Optics Communications* 3612016, pp. 110–115. DOI: 10.1016/j.optcom.2015.10.043.

[87] Huang, Y. et al. “High-Efficiency Inverted Perovskite Solar Cells via In Situ Passivation Directed Crystallization”. *Advanced Materials* 36(41), 2024, p. 2408101. DOI: 10.1002/adma.202408101.

[88] Yang, F. et al. “Efficient and spectrally stable blue perovskite light-emitting diodes based on potassium passivated nanocrystals”. *Advanced Functional Materials* 30(10), 2020, p. 1908760. DOI: 10.1002/adfm.201908760.

[89] Kuang, Y. et al. “High-performance pure red quasi-two-dimensional perovskite light-emitting diodes with bifunctional potassium trifluoroacetate additive”. *ACS Materials Letters* 5(11), 2023, pp. 2922–2928. DOI: 10.1021/acsmaterialslett.3c00557.

[90] Shen, Y. et al. "Interfacial potassium-guided grain growth for efficient deep-blue perovskite light-emitting diodes". *Advanced Functional Materials* 31(6), 2021, p. 2006736. DOI: 10.1002/adfm.202006736.

[91] Yang, J.-N. et al. "Potassium bromide surface passivation on CsPbI3-xBr x nanocrystals for efficient and stable pure red perovskite light-emitting diodes". *Journal of the American Chemical Society* 142(6), 2020, pp. 2956–2967. DOI: 10.1021/jacs.9b11719.

[92] Kerkache, L. et al. "Physical properties of RF sputtered ITO thin films and annealing effect". *Journal of Physics D: Applied Physics* 39(1), 2005, p. 184. DOI: 10.1088/0022-3727/39/1/027.

[93] Laxmi, L., Srinivasan, P., and Kabra, D. "Optical and optoelectronic properties of 2D, quasi-2D and 3D metal halide perovskites". *Journal of Materials Chemistry C* 132025. DOI: doi.org/10.1039/D4TC04864D.

[94] Li, H. et al. "Dual ligands synergy enables thermal and moisture stability-enhanced blue quasi-2D perovskite for efficient light-emitting diodes". *Chemical Engineering Journal* 4822024, p. 148659. DOI: 10.1016/j.cej.2024.148659.

[95] Li, H. et al. "Control of n-phase distribution in quasi two-dimensional perovskite for efficient blue light-emitting diodes". *ACS Applied Materials & Interfaces* 15(7), 2023, pp. 9574–9583. DOI: 10.1021/acsami.2c19979.

[96] Dong, F. et al. "Partially Ionized Amino Acid Salt Enabling Spatially Vertical n-Phase Distribution of Quasi-2D Perovskite for Efficient Deep-Blue Light-Emitting Diodes". en. *Advanced Optical Materials* 12(28), $2024_0 7$. DOI: 10.1002/adom.202401247.

[97] Liu, Y. et al. "Emerging thermochromic perovskite materials: insights into fundamentals, recent advances and applications". *Advanced Functional Materials* 34(37), 2024, p. 2402234. DOI: 10.1002/adfm.202402234.

[98] Taylor, A. D. et al. "A general approach to high-efficiency perovskite solar cells by any antisolvent". *Nature communications* 12(1), 2021, p. 1878. DOI: 10.1038/s41467-021-22049-8.

[99] Lukong, V. T., Ukoba, K., and Jen, T.-C. "Review of self-cleaning TiO2 thin films deposited with spin coating". *The International Journal of Advanced Manufacturing Technology* 122(9), 2022, pp. 3525–3546. DOI: 10.1007/s00170-022-10043-3.

[100] Baptista, A. et al. "Sputtering physical vapour deposition (PVD) coatings: A critical review on process improvement and market trend demands". *Coatings* 8(11), 2018, p. 402. DOI: 10.3390/coatings8110402.

[101] Guo, K. et al. "Efficient All-Solution-Processed Perovskite Light-Emitting Diodes via a Room-Temperature Vapor-Treated Interlayer". *ACS Applied Materials & Interfaces* 17(10), 2025, pp. 15688–15697. DOI: 10.1021/acsami.4c19098.

[102] Stenzel, O. *The Physics of Thin Film Optical Spectra: An Introduction*. 1st. Vol. 44. Springer Series in Surface Sciences. Berlin, Heidelberg: Springer, 2005. ISBN: 978-3-540-23683-3. DOI: 10.1007/b138175.

[103] Rakić, A. D. "Algorithm for the determination of intrinsic optical constants of metal films: application to aluminum". *Appl. Opt.* 34(22), 1995, pp. 4755–4767. DOI: 10.1364/AO.34.004755.

[104] Archer, E. et al. "Accurate efficiency measurements of organic light-emitting diodes via angle-resolved spectroscopy". *Advanced Optical Materials* 9(1), 2021, p. 2000838. DOI: 10.1002/adom.202000838.

[105] Guo, R. et al. "Refining the substrate surface morphology for achieving efficient inverted perovskite solar cells". *Advanced energy materials* 13(43), 2023, p. 2302280. DOI: 10.1002/aenm.202302280.

[106] Kim, T. H., Kim, B. W., and Im, S. H. "A Self-Assembling Molecule for Improving the Mobility in PEDOT: PSS Hole Transport Layer for Efficient Perovskite Light-Emitting Diodes". *Advanced Electronic Materials*2024, p. 2400626. DOI: 10.1002/aelm.202400626.

[107] Huang, S., Liang, C., and Lin, Z. "Application of PACz-Based Self-Assembled Monolayer Materials in Efficient Perovskite Solar Cells". *ACS Applied Materials & Interfaces* 16(47), 2024, pp. 64424–64446. DOI: 10.1021/acsami.4c13977.

[108] Levine, I. et al. "Charge transfer rates and electron trapping at buried interfaces of perovskite solar cells". *Joule* 5(11), 2021, pp. 2915–2933. DOI: 10.1016/j.joule.2021.07.016.

[109] Al-Ashouri, A. et al. "Conformal monolayer contacts with lossless interfaces for perovskite single junction and monolithic tandem solar cells". *Energy & Environmental Science* 12(11), 2019, pp. 3356–3369. DOI: 10.1039/c9ee02268f.

[110] Almasabi, K. et al. "Hole-transporting self-assembled monolayer enables efficient single-crystal perovskite solar cells with enhanced stability". *ACS Energy Letters* 8(2), 2023, pp. 950–956. DOI: 10.1021/acsenergylett.2c02333.

[111] Al-Ashouri, A. et al. "Monolithic perovskite/silicon tandem solar cell with> 29% efficiency by enhanced hole extraction". *Science* 370(6522), 2020, pp. 1300–1309. DOI: 10.1126/science.abd4016.

[112] Wang, Y.-K. et al. "Self-assembled monolayer–based blue perovskite LEDs". *Science Advances* 9(36), 2023, eadh2140. DOI: 10.1126/sciadv.adh2140.

[113] Wang, N. et al. "Morphology control of perovskite light-emitting diodes by using amino acid self-assembled monolayers". *Applied Physics Letters* 108(14), 2016. DOI: 10.1063/1.4945330.

[114] Tang, L. et al. "Enhanced performance of perovskite light-emitting diodes via diamine interface modification". *ACS applied materials & interfaces* 11(32), 2019, pp. 29132–29138. DOI: 10.1021/acsami.9b11866.

[115] Shin, Y. S. et al. "A Multifunctional Self-Assembled Monolayer for Highly Luminescent Pure-Blue Quasi-2D Perovskite Light-Emitting Diodes". *Advanced Optical Materials* 10(20), 2022, p. 2201313. DOI: 10.1002/adom.202201313.

[116] Xie, M. et al. "Hard–Soft-Acid–Base Management Enabled Bright and Stable Pure-Blue Perovskite Quantum Dot LEDs". *ACS nano* 19(31), 2025. DOI: 10.1021/acsnano.5c06917.

[117] Cao, S. et al. "Hybrid Self-Assembled Molecular Interlayers for Efficient and Stable Inverted Perovskite Solar Cells". *Advanced Energy Materials* 15(23), 2025, p. 2405367. DOI: 10.1002/aenm.202405367.

[118] Cao, Q. et al. "Co-Self-Assembled monolayers modified NiOx for stable inverted perovskite solar cells". *Advanced Materials* 36(16), 2024, p. 2311970. DOI: 10.1002/adma.202311970.

[119] Song, D. et al. "Interfacial engineering with a hole-selective self-assembled monolayer for tin perovskite solar cells via a two-step fabrication". *ACS Energy Letters* 6(12), 2021, pp. 4179–4186. DOI: 10.1021/acsenergylett.1c02124.

[120] Synopsys. *TCAD Sentaurus: Sentaurus Device User Guide*. 2023.

[121] Islam, M. B. et al. "NiOx hole transport layer for perovskite solar cells with improved stability and reproducibility". *ACS omega* 2(5), 2017, pp. 2291–2299. DOI: 10.1021/acsomega.7b00538.

[122] Aboulsaad, M. et al. "Thermal oxidation of sputtered nickel nano-film as hole transport layer for high performance perovskite solar cells". *Journal of Materials Science: Materials in Electronics* 30(22), 2019, pp. 19792–19803. DOI: 10.1007/s10854-019-02345-2.

[123] Jiang, T. et al. "Self-assembled monolayer hole transport layers for high-performance and stable inverted perovskite solar cells". *Energy & Fuels* 38(21), 2024, pp. 21371–21381. DOI: 10.1021/acs.energyfuels.4c03889.

[124] Intaniwet, A. et al. "Achieving a stable time response in polymeric radiation sensors under charge injection by X-rays". *ACS applied materials & interfaces* 2(6), 2010, pp. 1692–1699. DOI: 10.1021/am100220y.

[125] Wang, S. et al. "Fluorinated isopropanol for improved defect passivation and reproducibility in perovskite solar cells". *Nature Energy*2025, pp. 1–10. DOI: 10.1038/s41560-025-01791-z.

[126] Kim, H. et al. "Polymethyl methacrylate as an interlayer between the halide perovskite and copper phthalocyanine layers for stable and efficient perovskite solar cells". *Advanced Functional Materials* 32(13), 2022, p. 2110473. DOI: 10.1002/adfm.202110473.

[127] Jiang, N. et al. "Insight into perovskite light-emitting diodes based on PVP buffer layer". *Journal of Luminescence* 2412022, p. 118515. DOI: 10.1016/j.jlumin.2021.118515.

[128] Griffiths, D. J. and Schroeter, D. F. *Introduction to quantum mechanics*. 3rd ed. Cambridge university press, 2018. ISBN: 978-1-107-18963-8 (Hardback), 978-1-316-60096-7 (Paperback).

[129] Traoré, B. et al. "Band gap, effective masses, and energy level alignment of 2D and 3D halide perovskites and heterostructures using DFT-1/2". *Physical Review Materials* 6(1), 2022, p. 014604. DOI: 10.1103/PhysRevMaterials.6.014604.

[130] Xia, Y. et al. "Spatial Crystallization Homogenization Boosts Scalable Perovskite Light-Emitting Diodes". *Advanced Materials*2025, e06413. DOI: 10.1002/adma.202506413.